

Study of Turbulent Flow and Heat Transfer Over a Backward-Facing Step Under Impingement Cooling

Khudhey S. Mushatet

College of Engineering, Thiqr University

Nassiriya, Iraq

Salimhamed2000@yahoo.com

Abstract

Computations are presented to study the turbulent flow and heat transfer over a channel backward-facing step under impingement cooling. The problem was simulated for different parameters, such as the number of impinging jets, contraction ratio, size of jets, and jet and channel Reynolds numbers. The contraction ratio had the values 0.25, 0.35 and 0.5. The impinging jets were normal to the cross-channel flow. A control volume approach using staggered grid techniques was considered to integrate the continuity, fully elliptic Navier-Stokes and energy equations. A computer program was developed, and the SIMPLE algorithm was employed to determine the existence of coupling between the continuity and Navier-Stokes equations. The effect of turbulence was modelled using a k- ϵ model while the wall functions laws were used to treat the regions near the solid walls. The presented results show that the strength and size of recirculation regions near the reattachment region just after the backward-facing step increase as the contraction ratio increases. Also, the results show that the size of jets, number of jets, and jet and channel Reynolds numbers have a significant effect on the flow field, turbulent kinetic energy and variation of the Nusselt number.

Keywords: Impingement Cooling, Backward-Facing, Turbulent Flow.

دراسة الجريان الاضطرابي وانتقال الحرارة فوق عتبة داخل مجرى هوائي بوجود تبريد تصادمي

المستخلص

في هذا البحث تم إجراء دراسة حسابية لدراسة خصائص الجريان الاضطرابي وانتقال الحرارة فوق عتبة داخل مجرى هوائي و بوجود التبريد التصادمي. تم نمذجة المسألة المدروسة بتأثير عدة عوامل مثل حجم وعدد المنافذ، نسبة التضخيم وأرقام رينولدز للمجرى الرئيسي والمنافذ. نسب التضخيم المدروسة كان لها قيم 0.25، 0.3، 0.5 على التوالي والمنافذات التصادمية كانت عمودية على المجرى الرئيسي. استخدمت طريقة الحجم المحدد مع تقنية الشبكة الزاحفة لتكامل

معادلات الاستمرارية و ناثير-ستوكس والطاقة بينما طور برنامج حاسوب بلغة فورتران وباعتماد خوارزمية الاجراء المبسط التي تحدد الارتباط بين الاستمرارية ومعادلات ناثير-ستوكس. استخدم نموذج الاضطراب $k-\varepsilon$ لنمذجة تأثير الاضطراب في الجريان. اوضحت النتائج التي تم الحصول عليها ان قوة وحجم مناطق إعادة التدوير وطول إعادة الاتصال خلف العتبة يزداد مع زيادة نسبة التخصر. أيضا بينت النتائج أن حجم وعدد المنافث وأرقام رينولدز للمجرى الرئيسي والمنافث لها تأثير واضح على مجال الجريان والطاقة الحركية للضطراب وعدد نسلت.

1. Introduction

Flow separation and reattachment phenomena occur in many engineering and technological applications, such as cooling of turbine blades, cooling of electronic devices, combustion chambers, and flows around buildings, hills and aircrafts. In some applications, the separated and re-attachment regions must be controlled to optimally enhance the heat transfer rate. In the conventional problem of a backward-facing step, however, the geometry is simple, but the resulting structure of the flow field is complicated, especially after the step where a mixing region is created. The impingement cooling mechanism are considered when fast and effective heat transfer dissipation from the hot surface is needed. This mechanism is enhanced when array of multiple impinging jets are used instead of a single jet where mixing zones between these jets are created. Thus this paper tries to conduct a study emphasis on enhancing the rate of heat transfer via incorporating array of impinging slot jets in to the problem of a backward facing step. A channel with a backward-facing step has been investigated experimentally and numerically. Lio an Hwang [1] performed a numerical study on turbulent flow in a duct with a backward-facing step. The turbulent flow and heat transfer in a channel with rib turbulators was investigated by Lio and chen [2], Rau et al. [3] and Hane and Park [4]. The main objective of these studies was to obtain the heat transfer characteristics and friction factor.

Kasagi and Matsunaga [5] studied the turbulent flow in a channel with a backward facing step. 3-D particle tracking velocimeter was used as a measurement technique. They found that the Reynolds normal and shear stresses had the maximum values upstream of the re-attachment. Their study was compared with numerical simulation. Jovice and Driver [6] presented an experimental study on the turbulent flow over a backward facing step at low Reynolds number. The aim was to validate the numerical simulation which was performed by Stanford/NASA center for turbulence research. They demonstrated that the backward facing step flows were sensitive to step height and Reynolds number. ABE and Kondah[7] presented a new turbulent model for predicting fluid flow and heat transfer in separating and reattaching flows. The presented model was modified from low-Reynolds number $k-\varepsilon$ model. They

demonstrated that the used model was efficient in separating and reattaching flows downstream of backward facing step. Ichimiya and Hosaka [8] presented an experimental study to investigate the characteristics of impingement heat transfer caused by three impinging jets. They conducted that there was two peaks of the local Nusselt number behind the second nozzle. Zhang et al. [9] developed a stochastic separation flow model to simulate the sudden expansion of particle-laden flows. A large eddy method and Lagrangian techniques were used by Wang et al. [10] to simulate the turbulent flow over a backward-facing step. The study verified that the particles follow a path when the vorticity of the gas phase is small. Thangam and Knight [11] and Nie and Armaly [12] studied the effect of step height on the separation flow for convective flow adjacent to a backward-facing step. Rhee and Sung [13] adopted a diffusive tensor heat transfer model instead of the familiar constant Prandtl number model. An experimental study was presented by Feng et al. [14] to visualise the turbulent separated flow and measure the wall pressure over a backward-facing step. The study showed that below the separation bubble and the reattachment zone, the negative peak of the time varying wall pressure was in phase with the passage of the local large scale vertical structure. Several studies have reviewed the subject of impingement cooling. Law and Masliyah [15], Chou and Hung [16] and Lee et al. [17] performed a numerical investigation on low Reynolds number impinging jets, which were used to avoid hydrodynamic pressure caused by impingement on the surface. Benna et al. [18], Park and Sung [19] and Cooper et al. [20] presented numerical studies on high Reynolds number impinging jets with different turbulence models. Beitelmal et al. [21] investigated the heat transfer distribution in the impingement region. The considered impinging jets were inclined at different angles of attack. Yang and Shyu [22] and Gabry et al. [23] used CFD models to predict the heat transfer distribution on a smooth surface under an array of angled impinging jets with cross flow. Different angles of attack and conjugate conduction in the boundary were included. The study verified that the Yang-Shih model performed better than the k- ϵ model. Four turbulence models were used by Craft et al. [24] to simulate the turbulent flow of impinging jets discharging from a circular pipe.

In this work, an attempt is made to incorporate the effect of impinging slot jets to the problem of channel backward-facing step flow. To the knowledge of the author, there is no study documented on this particular flow geometry up to date, Consequently this study will assist to promote the research area and giving new aspects to enhance the rate of heat transfer. Thus, a computational study to simulate the turbulent flow and heat transfer of multiple impinging slot jets over a backward-facing step in cross channel flow was carried out as

shown in Figure (1). The scenario was tested with different parameters, such as the contraction ratio (SR), the size and number of impinging jets, and jet and channel Reynolds numbers. The aim of the present work is to show how array of multiple confined impinging slot jets can be a controlling factor to enhance the rate of heat transfer from the hot surface of the channel backward facing step.

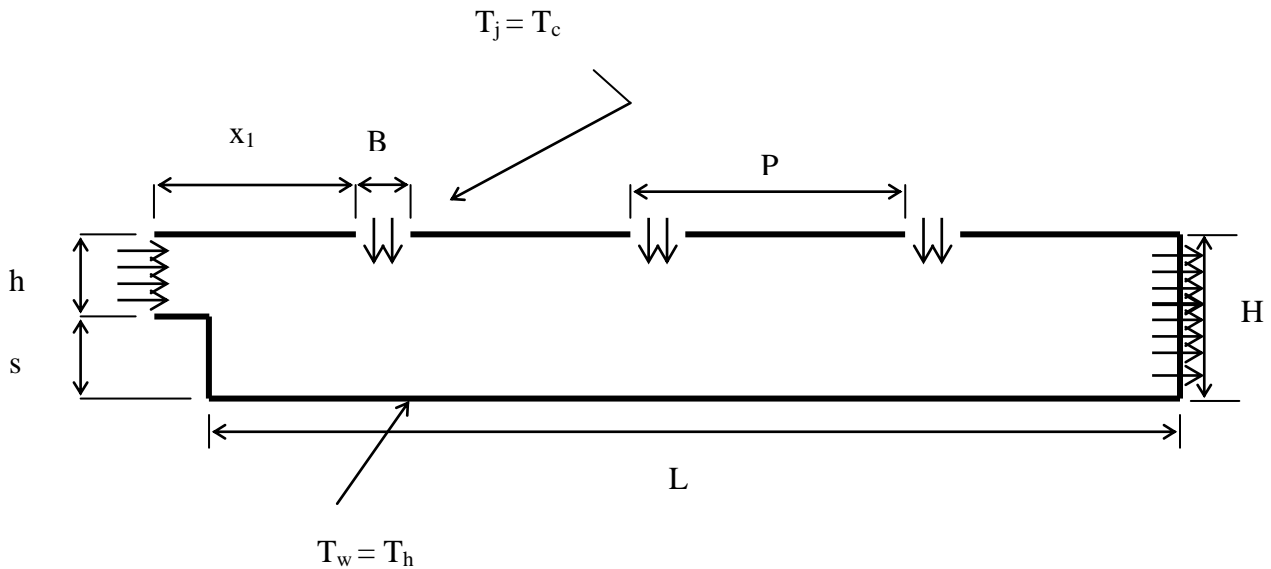


Figure (1). Schematic diagram of the considered problem, $H=0.05\text{m}$, $L=0.4\text{m}$, $x_1=0.0492\text{m}$, $H/B=11$, $P/B=4$.

2. Mathematical model and numerical solution

The following assumptions are used to simplify the solution of mathematical model.

1. Steady state
2. Incompressible flow
3. Constant thermo physical properties.
4. Non slip flow
5. Steady state

The continuity, turbulent fully elliptic Navier-Stokes and energy equations are used to model the considered problem.

$$\frac{\partial}{\partial x_i}(\rho U_i) = 0 \quad (1)$$

$$\frac{\partial U_i U_j}{\partial x_j} = \frac{-\partial P}{\partial x_i} + \frac{\partial}{\partial x_j} \left(\mu \frac{\partial U_i}{\partial x_j} - \overline{\rho u_i u_j} \right) \quad (2)$$

$$\frac{\partial U_i T_j}{\partial x_j} = \frac{\partial}{\partial x_j} \left(\frac{\mu}{Pr} \frac{\partial T_i}{\partial x_j} - \overline{\rho u_i t_j} \right) \quad (3)$$

The turbulent stresses $\overline{\rho u_i u_j}$ and turbulent heat fluxes $\overline{\rho u_i t_j}$ should be modelled in order to close the mentioned governing equations. One of the most widely used turbulence models is the standard k-ε model because it has the ability to handle complex high Reynolds number flows in much less time than other complicated models. However this model gives un prediction of the flow characteristics especially in re-circulating regions as in the region downstream of backward facing, Abet and Kondoh[25]. The next section in the discussion of results will offer the percentage of this un prediction for the flow and thermal field. This model solves two transport equations: one for the turbulent kinetic energy and the other for the dissipation rate of the turbulent kinetic energy, Jones and Lunder [26], as shown below:

$$\frac{\partial \rho k U_i}{\partial x_j} = \frac{\partial}{\partial x_j} \left[\left(\mu + \frac{\mu_t}{\sigma_k} \right) \frac{\partial k}{\partial x_j} \right] + \rho (G_b - \varepsilon) \quad (4)$$

$$\frac{\partial \rho \varepsilon U_j}{\partial x_j} = \frac{\partial}{\partial x_j} \left[\left(\mu + \frac{\mu_t}{\sigma_\varepsilon} \right) \frac{\partial \varepsilon}{\partial x_j} \right] + \rho \frac{\varepsilon}{k} (C_{1\varepsilon} G_b - C_{2\varepsilon} \varepsilon) \quad (5)$$

where the shear production term, (G_b), is defined as:

$$G_b = \mu_t \left(\frac{\partial u_i}{\partial x_j} + \frac{\partial u_j}{\partial x_i} \right) \frac{\partial u_i}{\partial x_j} \quad (6)$$

The turbulent viscosity is given by:

$$\mu_t = \rho c_\mu \frac{k^2}{\varepsilon} \quad (7)$$

The model coefficients are (σ_k ; σ_ε ; $C_{1\varepsilon}$; $C_{2\varepsilon}$; C_μ) = (1.0, 1.3, 1.44, 1.92, 0.09), respectively.

Boundary Conditions

At the walls: $U = V = 0$, $k = 0$, and $\frac{\partial \varepsilon}{\partial y} = 0$

At the lower wall: $\theta = 1$

At the upper wall: $\frac{\partial \theta}{\partial y} = 0$

At inlet:

$$k_{in} = 0.05U_{in}^2, k_j = 0.05U_j^2, T_{in} = T_c, T_j = T_c, T_w = T_h$$

$$\varepsilon_{in} = k_{in}^{1.5} / \lambda H, \varepsilon_j = k_j^{1.5} / \lambda B, \lambda = 0.005$$

$$Re_{in} = \frac{U_{in}h}{\nu}, Re_j = \frac{U_jB}{\nu}$$

where $k_{in}, k_j, U_{in}, U_j, T_{in}, T_j$ are the turbulent kinetic energies, velocities and temperatures at a channel inlet and slot jet inlet, respectively.

The local Nu along the bottom hot wall is expressed as $Nu = \frac{\partial \theta}{\partial Y}$ at $y=0$.

At the channel exit, zero gradients are imposed for the dependent variables. To remedy the large steep gradients near the walls of the channel and the step, wall function laws proposed by Versteeg [27] are incorporated. because they are popular and save computational resources. In this study, the numerical computations are performed on a non-uniform staggered grid system. A finite volume method (FVM) described by Versteeg [27] is adopted to integrate the governing equations from (1) to (5).

$$\int_{cv} (\rho \phi u) dv = \int_{cv} \text{div}(\Gamma \text{grad} \phi) dv + \int_{cv} S_\phi dv \quad (8)$$

Thus, a system of discretisation equations is developed, which means that the system of elliptic partial differential equations is transformed into a system of algebraic equations. Then, the solution of these transformed equations is performed by an implicit line by line Gaussian elimination scheme. An elliptic finite volume computer code was developed to attain the results of the numerical procedure by using pressure-velocity coupling (SIMPLE algorithm), according to Versteeg [27]. This code is based on a hybrid scheme. Because of the strong coupling and non-linearity that are inherent in these equations, relaxation factors are needed to ensure convergence. The relaxation factors used for velocity components and the pressure, temperature and turbulence quantities are 0.45, 1, 0.6, and 0.6, respectively. However these relaxation factors have been adjusted for each case to accelerate the convergence criterion, which is defined as the relative difference of every dependent variable between iteration steps: $\text{Max} |\phi^k(i, j) - \phi^{k-1}(i, j)| \leq 10^{-5}$.

To ensure that the turbulent fluid flow solutions are not significantly affected by the mesh, the numerical simulations are examined under different grid sizes that range from 62×28 to 82×52 . Adding grid points beyond 62×28 did not significantly affect the results.

3. Results and discussion

The computations are presented for two-dimensional turbulent flow through a channel with a backward-facing step and impingement cooling. Different contraction ratios and sizes of impinging jets are investigated for different Reynolds numbers.

The velocity vectors for different numbers of impinging jets are shown in Figures(2-4). As Figure (2) shows, the separation and reattachment, and consequently the recirculation regions, are found directly behind the backward-facing step and the impinging jets. The cross flow begins to separate at the edge of the step and forms a recirculation region. The size and strength of this region depends on the expansion ratio and the existing impinging jets. It is evident that the strength of the recirculation region increase. Also the dimensionless re-attachment length(L_T) after the step increase as the contraction ratio (SR) decrease where $L_T=2, 2.28, 2.3$ as shown in (a), (b) and (c) respectively; this trend is evident in the studied cases. Recirculation between the impinging jets increased as the contraction ratio and number of impinging slot jets increased. It can be seen that the incoming cross flow affects the behaviour of the trajectories of multiple impinging jets because the potential core of each jet is distorted. Part of the flow of impinging jets forms re-circulating regions between the jets, and the other part tries to push the incoming cross flow towards the lower wall of the channel; thus, the combined flow accelerates and becomes narrower. The size of the recirculation region and, consequently, the re-attachment length are affected by the impinging slot jet flow. As the Figure shows, the near upstream impinging jet has a significant effect on this region; it distorts the structure and size of the mentioned recirculation region where the separated flow after the step is pushed towards the bottom wall. As a result, the size and re-attachment length of the recirculation region are minimised. For Figures (3) and (4), the size and strength of the recirculation regions for three and four jets are larger than those with two jets. However, the flow structure is similar for all scenarios. Also, the size and recirculation regions increase as the number of impinging jets increases. The heat transfer is enhanced as the strength of the recirculation regions increases, as shown in Figure (10) where the local Nusselt number increases just after the step between the jets due to the increase in losses.

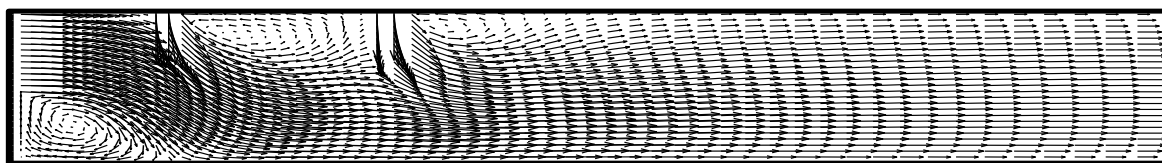
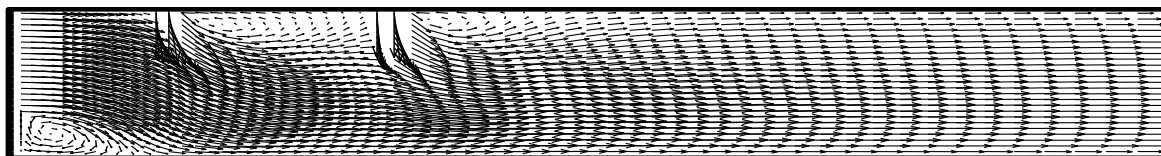
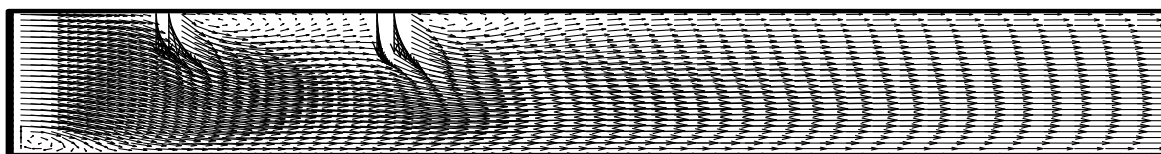
a. $SR = 0.5$ b. $SR = 0.35$ c. $SR = 0.25$

Figure (2). Computed velocity vectors for 2 jets and different values of step height ratios, $Re_j=13517$, $Re_{in}=16896$, $H/B=11$, and $P/B=4$.

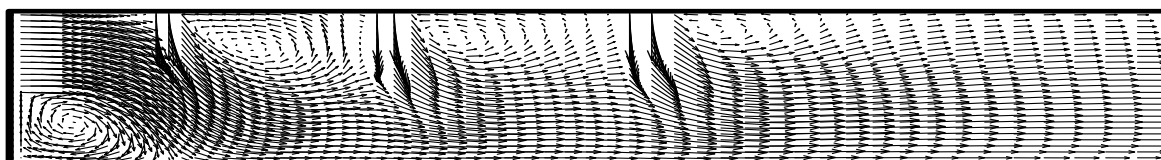
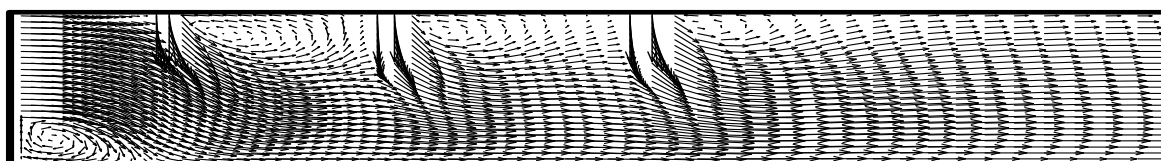
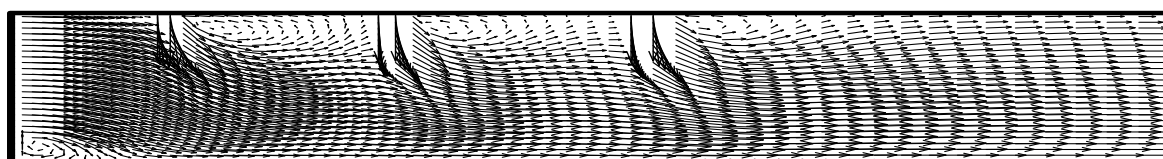
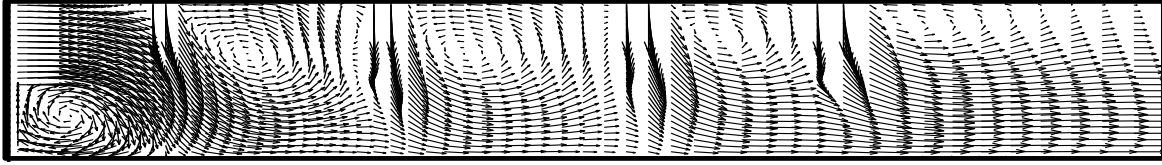
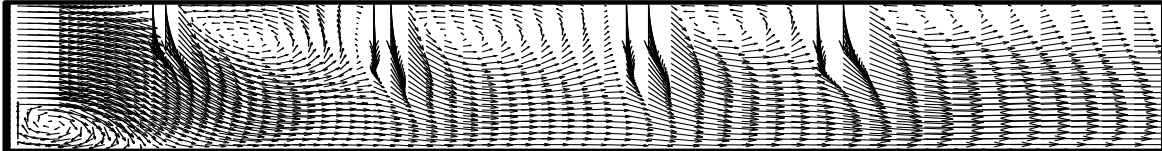
a. $SR = 0.5$ b. $SR = 0.35$ c. $SR = 0.25$

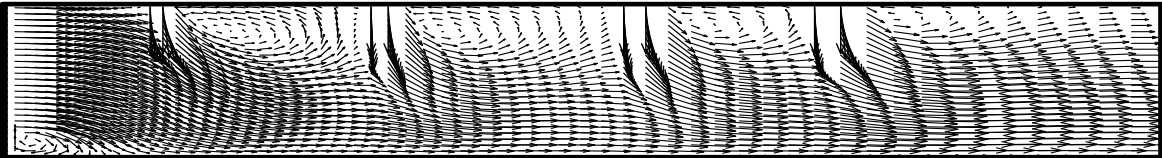
Figure (3). Computed velocity vectors for 3 jets and different values of step height ratios, $Re_j=13517$, $Re_{in}=16896$, $H/B=11$, and $P/B=4$.



a. SR =0.5



b. SR =0.35

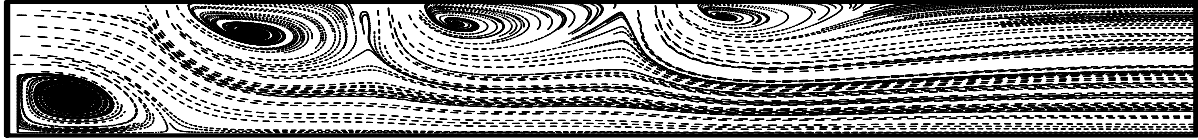


c. SR =0.25

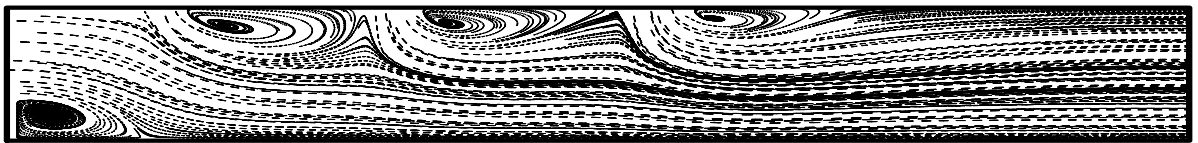
Figure (4). Computed velocity vectors for 4 jets and different values of step height ratios, $Re_j=13517$, $Re_m=16896$, $H/B=11$, and $P/B=4$.

The effect of contraction ratio on the distribution of streamlines for three impinging slot jets and $H/B=11$ is demonstrated in Figure (5). The trajectories of the impinging slot jet forced the cross channel flow towards the bottom wall of the channel and reduced the reattachment length just after the edge of the step. The flow struck the bottom wall in the region between the step and the first impinging jet and enhanced heat transfer, as shown in Figure (9). This phenomenon occurred for all the studied cases and is enhanced as the contraction ratio increased (the strength of recirculation regions increase). Beyond $x=0.1$, the rate of heat transfer decreases as the contraction ratio increases. Also, it is clear that the presence of impinging cooling enhances the heat transfer in the considered physical problem, as shown in Figure(10).

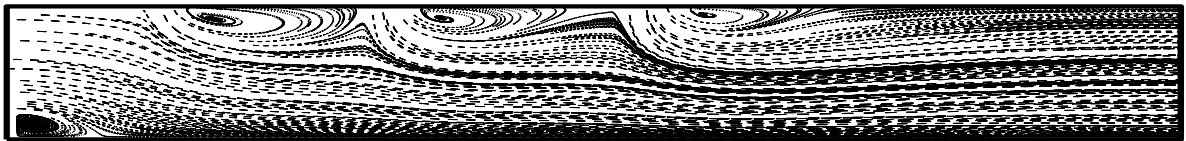
Figure (10) illustrates that three jets achieve the optimum rate of heat transfer. When the number of impinging slot jets exceeds three, the rate of heat transfer is significantly decreased beyond $x=0.1$.



a. $SR = 0.5$



b. $SR = 0.35$

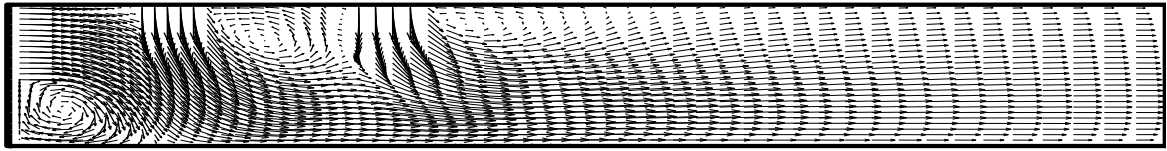


c. $SR = 0.25$

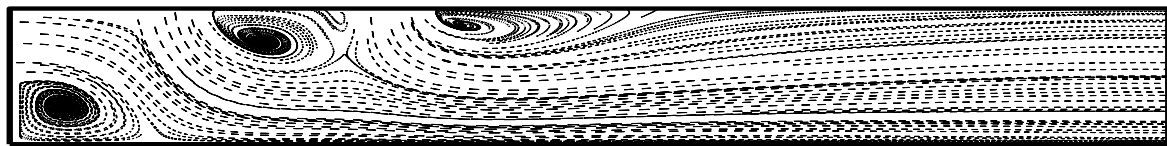
Figure (5). Stream line distribution for 3 jets and different values of step height ratios, $Re_j=13517$, $Re_{in}=16896$, $H/B=11$, and $P/B=4$.

Figures (6) and (7) demonstrate the effect of increasing the size and number of impinging jets on the computed flow field. The results are presented in the form of velocity vectors and stream lines. It is clear that the strength of recirculation regions behind each jet and the step increase as the slot jet width increases (the ratio H/B decreases). This flow structure is dominant for all the studied cases and affects the heat transfer, as shown in Figure (8). In general, the velocity of the main channel flow near the hot wall increases as the ratio H/B decreases (of the size of the slot jets increases) because the flow passage becomes narrower. The effect of increasing the size of the impinging jets on the distribution of the local Nusselt number is found in Figure (8). It is clear that the local Nusselt number increases as the slot jet width increases (the ratio H/B decreases) because the strength of recirculation regions are

larger behind each jet and the step. The strength recirculation regions increase the impinging flow towards the hot wall and consequently increases the rate of heat transfer.

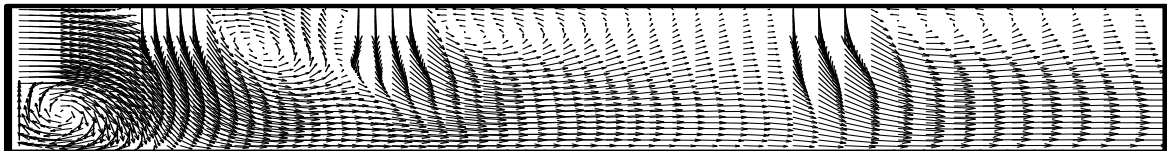


a. velocity vectors

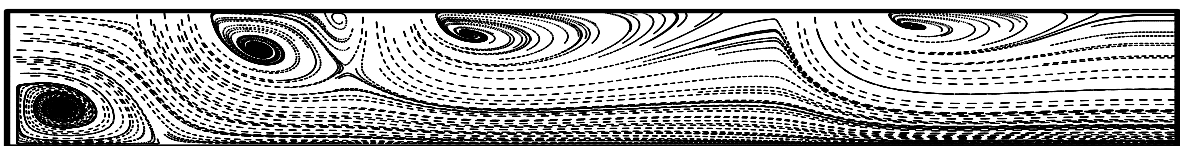


b. stream lines

**Figure (6). Effect of slot jet width on the flow field distribution for 2 jets:
SR=0.5, $Re_j=13517$, $Re_{in}=16896$, $H/B=2.5$, and $P/B=4$.**



a. velocity vectors



b. stream lines

**Figure (7). Effect of a slot jet width on the flow field distribution for 2 jets,
SR=0.5, $Re_{in}=16896$, $H/B=2.5$, $P/B=4$**

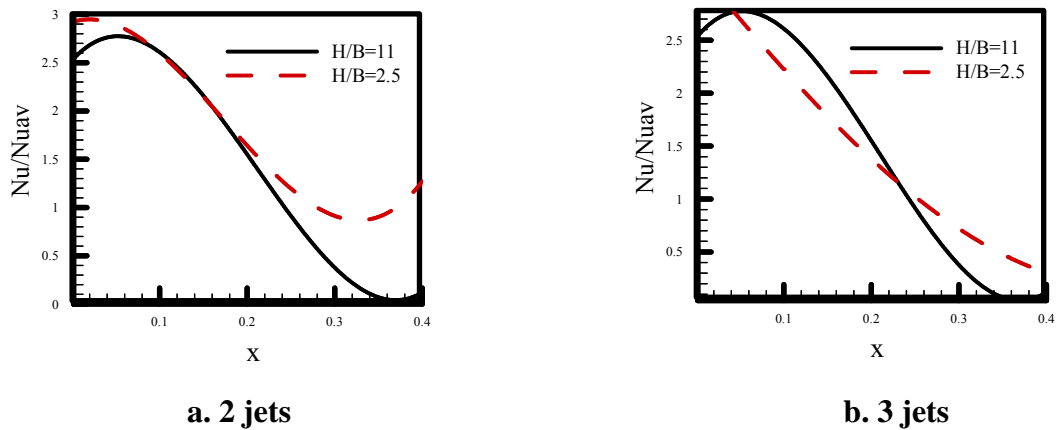


Figure (8). Variation of local Nusselt number for $SR=0.5$, $Re_j=13517$ and $Re_{in}=16896$.

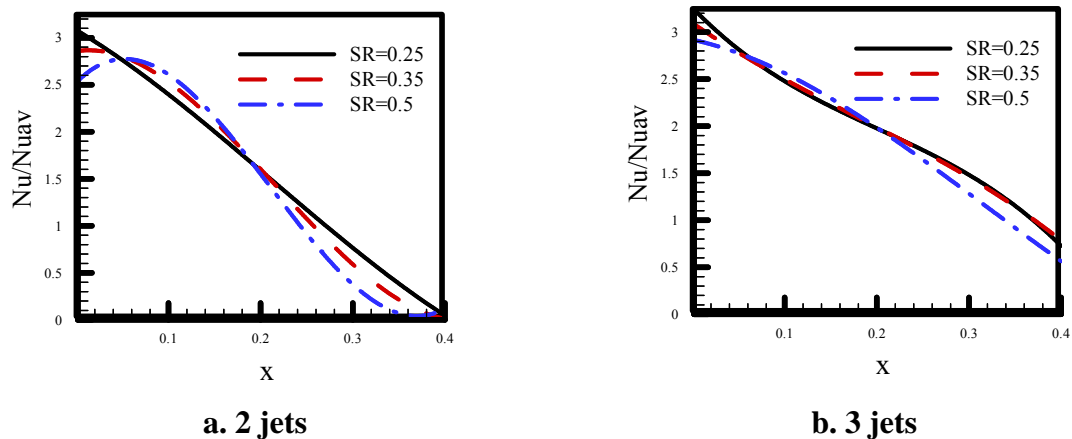


Figure (9). Variation of the local Nusselt number with multiple impingement jets, $Re_j=13517$, $Re_{in}=16896$, $H/B=11$, and $P/B=4$.

Figure (10) represents the variation of local Nusselt number along the hot wall of the backward facing in the presence of impinging jets and without impinging jets. As it is shown, the local Nusselt number is increased significantly in the presence jets compared with that of the case of no jets. Also, it is observed that the three impinging jets indicates the higher rate of heat transfer especially at $x > 0.2$.

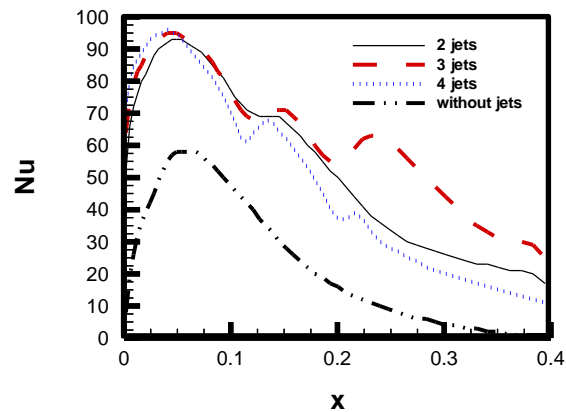
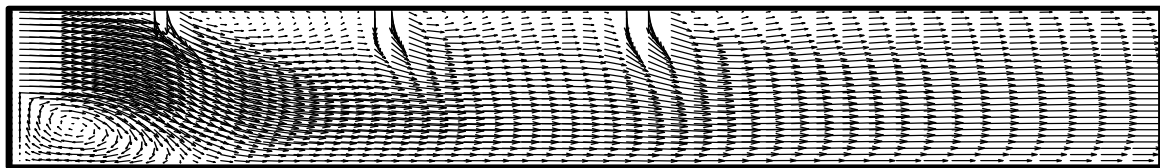
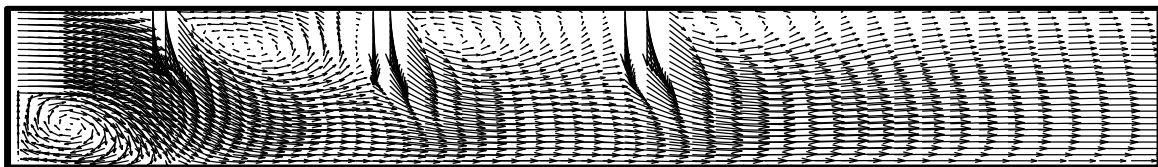


Figure (10). Comparison of variation of local Nusselt number with and without impingement for $SR=0.5$, $Re_j=13517$, $Re_{in}=16896$, $H/B=11$, $P/B=4$.

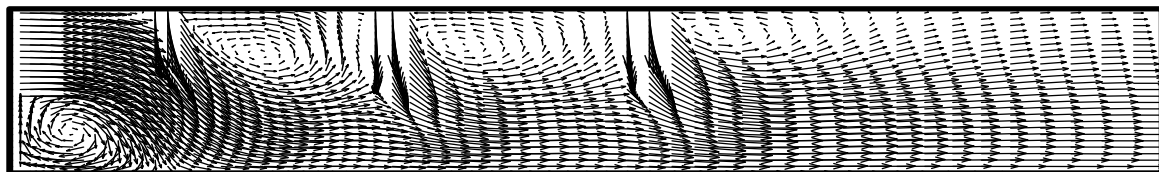
When the impinging jets and inlet channel flow Reynolds numbers increase, the recirculation regions behind each jet increase. However, the recirculation region after the step decreases, as shown in Figure (11). If the Reynolds number increases, the inertia force and penetration of the impinging flow to cross flow increase, which enhances the rate of heat transfer.



a. $Re_j= 6210$



b. $Re_j= 13517$



c. $Re_j= 28127$

Figure (11). Flow field distribution for different jet Reynolds numbers, $SR=0.5$, $H/B=11$, $P/B=4$, $Re_{in}=16896$.

Figure (12) illustrates the non-dimensional axial velocity at different axial positions. For $SR=0.5$, it is evident that the dimensionless axial velocity increases as Re increases for $x/L \leq 0.1$, while the velocity increases and then decreases when $x>0.1$.

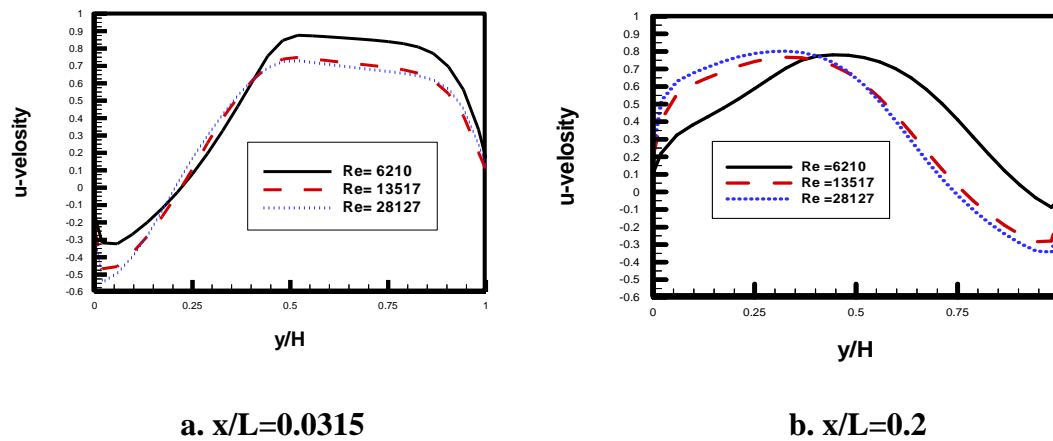


Figure (12). Variation of the dimensionless axial velocity (u/U_{in}) at different jet Reynolds numbers: $H/B=11$, $P/B=4$, $Re_{in}=16896$, and $SR=0.5$.

The distribution of dimensionless axial velocity is depicted at Figure (13) for 3 impinging jet jets and different contraction ratios. Figure (13) shows that the higher values of the velocity occur at $SR=0.25$, which confirms that the recirculation regions increase in size as SR increases, as discussed previously.

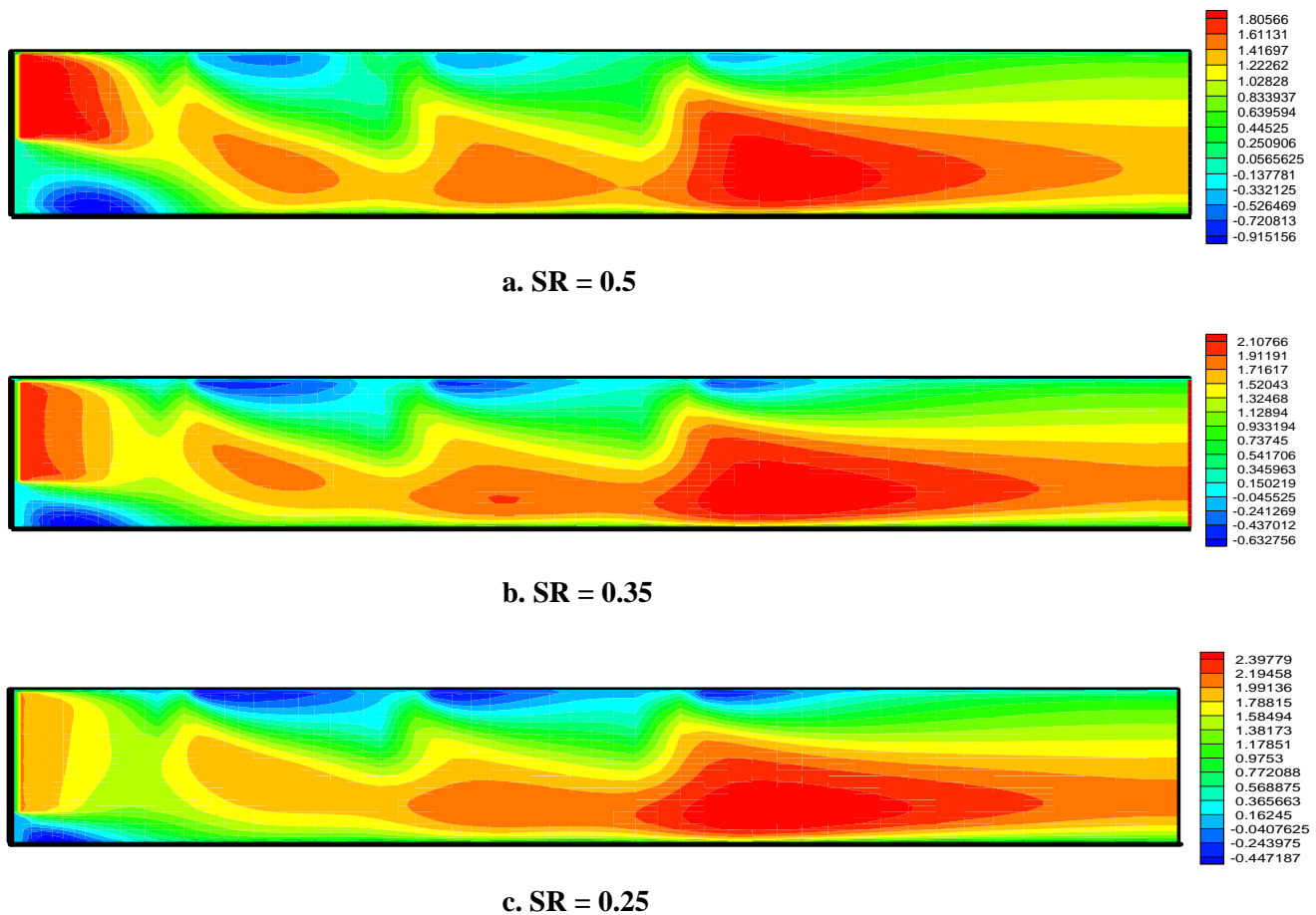


Figure (13). Distribution of dimensionless axial velocity(u/U_{in}) for 3 impingement jets, $H/B=11$, $P/B=4$, $Re_j=13517$, $Re_{in}=16896$.

Figure (14) illustrates the variation of the turbulent kinetic energy with different expansion ratios at the upper and lower walls of the channel. When $SR=0.5$, the turbulent kinetic energy values are higher at the lower wall compared to those at the upper one. This trend extends to the contraction ratio $SR=0.25$. The maximum and minimum values shown in the curves are due to the effect of the impinging jets .

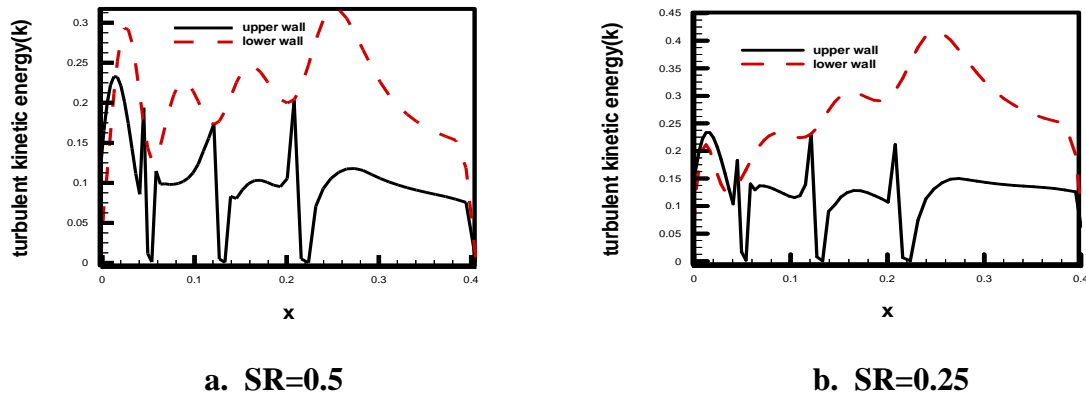


Figure (14). Variation of turbulent kinetic energy (at the walls), $Re_j=13517$, $Re_{in}=16896$, $H/B=11$, and $P/B=4$.

The effect of Re on the variation of turbulent kinetic energy at $y=H/2$ is depicted at Figure (15). It can be noted that the turbulent kinetic energy is increased as Re increases. It is expected that the increase of Re increases the stresses and consequently the turbulent kinetic energy increases.

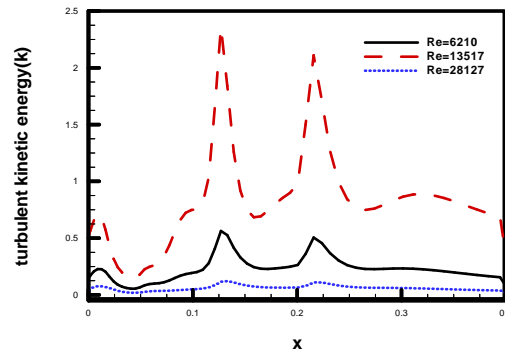


Figure (15). Variation of turbulent kinetic energy for different jet Reynolds numbers (at $y = H/2$): $SR=0.5$, $Re_{in}=16896$, $H/B=11$, and $P/B=4$.

To validate the present numerical code, a test on some of the published studies is performed as shown in Figures (16-18). As the Figures show, acceptable agreement is obtained. However some discrepancy is noticed . This is attributed to use of $k-\epsilon$ model where this model gives un prediction in some of recirculation flows. This un prediction is about 10%.

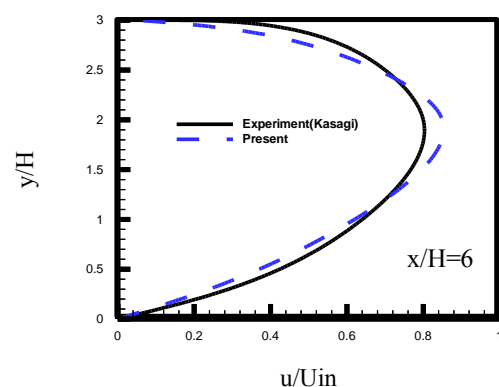


Figure (16). Comparison of the present results with experimental published results of Kasagi(1995), $Re=5540$.

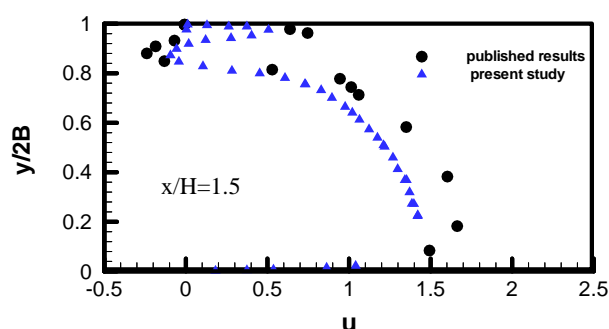


Figure (17) . Comparison between the present results and published experimental data of Lio et al.(1993).

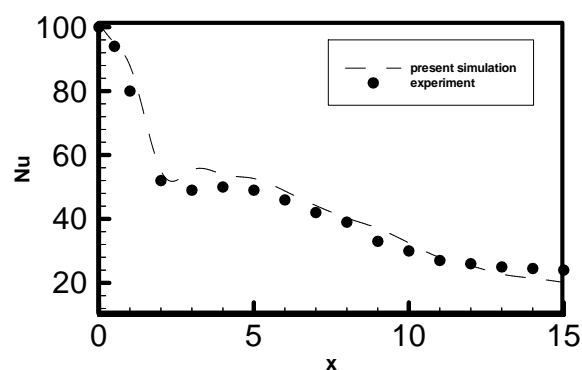


Figure (18). Comparison of the present results with published results of Ichimiya and Hosaka(1992).

4. Conclusions

The following conclusions are obtained from this study.

1. As compared with conventional backward-facing step flow problem, incorporating array of impinging slot jets is significantly enhanced the rate of heat transfer
2. Increasing the number of impinging slot jets enhanced the rate of heat transfer especially near the regions close to the facing step. However this behaviour is converted when number of these jets exceed three.
3. The strength of the recirculation zone behind each slot jet and the step increases as jet width increases.
4. The heat transfer rate increases as the jet size increases.
5. The turbulent kinetic energy is enhanced as the channel and slot jet flow Reynolds numbers increase.

5. References

- [1] Lio, T., Hwang, J., 1992, “ Developing Heat Transfer and Friction in a Ribbed Rectangular Duct with Flow Separation at Inlet”, ASME. J. Heat Transfer, 114, 546-573.
- [2] Lio, T.M., Hwang, G.G. , Chen, S.H., 1993, “Simulation and Measurements of Enhanced Turbulent Heat Transfer in Channels With Periodic Ribs on One Principal Wall” International Journal of Heat Mass Transfer, 36,507-507.
- [3] Rau, G., Cakan, M., Moeller, D., Arts, T., 1988,” The Effect of Periodic Ribs on The Local Aerodynamics and Heat Transfer Performance of A Straight Cooling Channel” ASME Journal of Turbomachinery, 120, 368-375.
- [4] Han, J.C, Heat , 1988, “Transfer and Friction Characteristics in Rectangular Channels With Rib Turbulators” ASME Journal of Heat Transfer, 110, 91-98.
- [5] Nobuhide Kasagi, Akio Matsunaga, 1995,” Three- Dimensional particle-Tracking-Velocimeter velocimetry measurement of Turbulence Statistics and Energy Budget in a backward-Facing Step Flow” Int. J. Heat and Fluid Flow, 16, 477-485.
- [6] Srba Jovice, David M. Driver, 1994 ,“ Backward Facing Step Measurements at Low Reynolds Number, $Re_h=500$ ”, NASA, California 94035-1000.
- [7] Abe, K., Kondoh, T., 1994, “A new Turbulent Model for Predicting Fluid Flow and Heat transfer in Separating and Reattaching flows”, 37,139-151.

- [8] Ichimiya, K., Hosaka, N., 1992 ,“Experimental Study of Heat Transfer Characteristics Due To Confined Impinging Two Dimensional Jet” Exp. Thermal and Fluid Science, 5,803-807.
- [9] Zhang, H.Q., Chan, C. K., Lau, K.S, 2001 ," Numerical Solution of Sudden Expansion Particle-Laden Flows Using an Improved Stochastic Flow Model”, Numerical Heat Transfer, Part A, 4089-102.
- [10] Wang, B., Zhang, H.Q., Wang, X.L., 2006, “ Large Eddy Simulation of Particle Response to Turbulence Along Its Trajectory in a Back Word-Facing Step Turbulent Flow”, Int. J. Heat Mass Transfer, 49, 415-420.
- [11] Thangam, S., Knight, D., 1989, “ Effect of Step Height on The Separated Flow Past a Backward Facing Step”, Phys. Fluids, 3, 604-606.
- [12] Nie, J.H., Armaly, B.F., 2002, “ Three Dimensional Convective Flow Adjacent to a Backward Facing Step-effects of Step Height”, Int. J. Heat Mass Transfer, 45, 2431-2438.
- [13] Rhee, G. H., Sung, H.G., 2000, “ Enhancement of Heat Transfer in Turbulent Separated and Re-Attachment Flow by Local Forcing”, Numerical Heat Transfer, Part A, 137, 733-735.
- [14] KE Feng, Liu Ying-Zheng , Chen Han-Ping, 2007,“ Simultaneous Flow Visualization and Wall Pressure Measurement of the Turbulent Separated and Re-attachment Flow Over a Backward Facing Step”, J. Hydrodynamics, 119, 108-187.
- [15] Law, H.S., Masliyah, J.H., 1984 ,“Mass Transfer Due to Confined Laminar Impinging Two Dimensional Jet”, Int. J. Heat Mass Transfer, 27, 529-539.
- [16] Chou, Y.J., Hung, Y.H., 1994 ,“Impinging Cooling of an Isothermally Heated Surface”, ASME. J. Heat Transfer, 116, 479-482.
- [17] Lee, X.C., Xheng, Q., Zhung, Y., Tia, Y.Q., 1997,” Numerical Study of Recovery Effect and Impingement Heat Transfer with Submerged Circular Jets of Large Prandtl Number Liquid”, Int. J. Heat Mass Transfer, 40, 2647-2653.
- [18] Behnia, M., Parneix, S., Shabany, Y., Durby, P.A., 1999,“Numerical Study of Turbulent Heat Transfer in Confined and Unconfined Impinging Jets”, Int. J. Heat Fluid Flow, 20, 1-9.
- [19] Cooper, D., Jackson, C., Launder, B.E., Liao, G.X., 1993, “Impingement Jet Studies for Turbulence Model Assessment-I Flow Field Experiments”, Int. J. Heat Mass Transfer, 36, 2675-2684.

- [20] Park, T.S., Sung, H.j., 2001,” Development of Near Wall Turbulence Model and Application to Jet Impingement Heat Transfer, *Int J. Heat Fluid Flow*, 22, 10-18.
- [21] Beitmal, A.H., Saad, M.A., Patel, C.D., 2000, “Effects of Surface Roughness on The Average Heat Transfer of An Impinging Air Jet”, *International Communications in Heat and Mass Transfer*, 27, 1-12.
- [22] Yang, Y.T., Shyu, C.H., 1999,” Numerical Study of Multiple Impinging Slot Jets With an Inclined Confinement Surface”, *Numerical Heat Transfer, Part A*, 33, 23-37.
- [23] EL-Gabry, Lamyaa, A., Kamiski, Deborah, A., 2005, “Numerical Investigation of Jet Impingement with Cross Flow-Comparison of Yang-Shih And Standard k- ϵ Turbulence Models”, *Numerical Heat Transfer, Part A*, 47, 441-469.
- [24] Craft, T.G., Graham, L.G.W., Launder, B.E., 1993, “Impinging Jet Studies For Turbulence Model Assessment-II-An Examination of the Performance of Four Turbulence Models”, *Int. J. Heat Mass Transfer*, 36, 2685-2697.
- [25] Shou Shing Hsieh, Jung-Tai Huang, Huang-Hsiu Tsai, 2003, “Impingement Cooling in a Rotating Square Annular Duct with Cross Flow Effect From Rib-Roughened Surface”, *Int. J. Heat Mass Transfer*, 39.
- [26] Jones, W.P., Lunder, B.E., 1972, “The Prediction of Laminarization with a Two Equation Model of Turbulence”, *J. Heat Mass transfer*.
- [27] Versteeg, H.K., Malalasekera, W., 1995, “An Introduction of Computational Fluid Dynamics”, Hemisphere Publishing Corporation, United State of America.

6. Nomenclature

G	generation term, $\text{Kg/m} \cdot \text{sec}^3$
H	height of the channel, m
k	turbulent kinetic energy, m^2/s^2
L	length of the channel, m
L_T	reattachment length behind the facing step(X_{cr}/s)
Nu	local Nusselt number, -
Nuav	average Nusselt number
p	pitch, m
P	pressure, N/m^2
Pr	Prandtl number, -

Re	Reynolds number, -
s	step height, m
SR	contraction ratio (s/H), -
T_C	cold wall temperature, $^{\circ}\text{C}$
T_H	hot wall temperature, $^{\circ}\text{C}$
$\overline{\rho u_i u_j}$	Reynolds stresses
$\overline{\rho u_i t_j}$	turbulent heat fluxes
U_{in}	velocity at a channel inlet
U_j	velocity at a slot jet inlet
X_{cr}	the reattaching distance behind the step

Greek symbols:

ϵ	turbulence dissipation rate, m^2/s^3
μ	dynamic viscosity, $\text{N.s}/\text{m}^2$
μ_t	turbulent viscosity, $\text{N.s}/\text{m}^2$
ρ	air density, Kg/m^3
Γ_{eff}	effective exchange coefficient, $\text{kg}/\text{m.s}$
θ	dimensionless temperature $\left(\frac{T - T_c}{T_h - T_c} \right)$, -
$\sigma_k, \sigma_\epsilon$	turbulent Schmidt numbers, -
α	thermal diffusivity of fluid, m^2/s
S_ϕ	source term, -
ϕ	constant property, -

The Model and the Method of Two-Level Routing in Mpls Network

Alexander V. Lemeshko

Dmytro V. Andrushko

Ahmad M. Hailan

Technical Sciences and The
Scientific Adviser TCS Department
Kharkov national university of radio
Electronics Lenina ave., 14, Kharkov,
61166, UKRAINE,
e-mail: avlem@mail.ru

TCS Department Kharkov National
University of Radio Electronics
Lenina ave, 14, Kharkov, 61166,
UKRAINE
e-mail: da@kture.kharkov.ua

TCS Department Kharkov national
university of radio electronics
Lenina ave, 14, Kharkov, 61166,
UKRAINE
e-mail: onlineahmeds@mail.ru

Abstract

In the article mathematical model for routing in the MPLS network is proposed. Also method of two-level routing on the basis of goal coordination principle in the MPLS network is offered. The method is used to increase the scalability of flow-based routing strategies.

Keywords : MPLS, routing, QoS, NGN .

المستخلص

في البحث اقتراح نموذج رياضي للتوجيه في الشبكة بواسطة التبديل متعدد البروتوكولات باستخدام المؤشرات التعريفية (MPLS). ويعرض أيضاً طريقة توجيه من مستويين بالاعتماد على مبدأ تنسيق الهدف في شبكة التبديل متعدد البروتوكولات باستخدام المؤشرات التعريفية (MPLS). هذه الطريقة استخدمت لتحسين وموازنة أداء إستراتيجية التوجيه.

1. Introduction

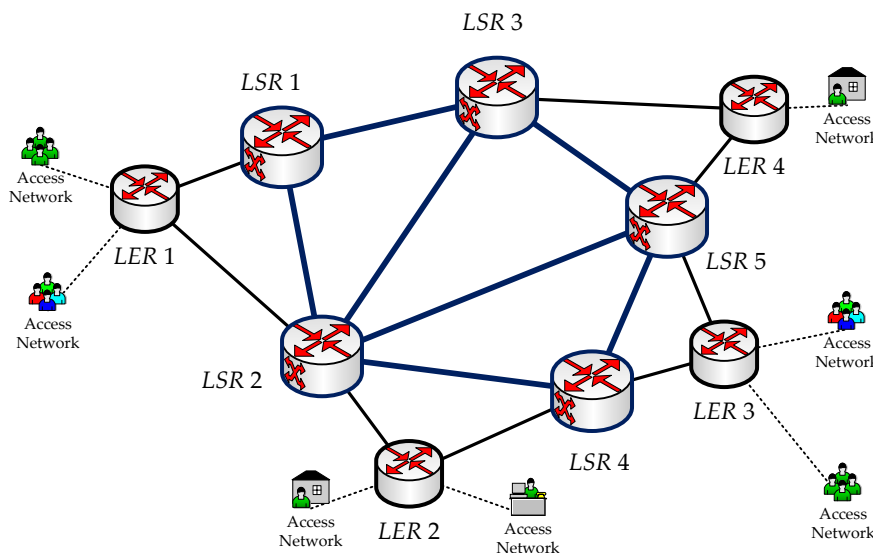
MPLS technology (*Multiprotocol Label Switching*) currently considered as the main transport platform for modern telecommunication systems [1, 2]. During it development previous experience of transport technologies such as IP (*Internet Protocol*) and ATM (*Asynchronous Transfer Mode*) was considered. That's why combination of IP-routing principles and high speed ATM-switching was implemented in MPLS technology. As a result MPLS use virtual connections with source-based routing that significantly expands the capabilities of quality of service (*QoS*) support in this technology. However, along with the advantages, MPLS has number of disadvantages specific to traditional routing

technologies. First of all, these are problems of routing scalability in case of telecommunication system territorial distribution, increase of network nodes number and their coherence, permanent user traffic grows and expansion of *QoS* parameters list.

Analysis has shown [3, 4] that the main way to improve existing and develop new routing protocols is to reevaluate routing mathematical models and methods which is, first of all, associated with the transition to the flow-based models. Such models, comparing to the graph-based take into account structural and functional parameters of telecommunication system and the traffic characteristics. In order to improve scalability of flow-based models, effective solutions are based on the principles of multi-level (hierarchical) routing [5, 6] traditionally used. Due to this, current paper introduces the routing mathematical model that belongs to the multi-level flow-based routing models class and adapted to features of MPLS-networks engineering and functioning.

2. The structural description of MPLS-network

Let's MPLS-network structure Figure (1) is described by graph $G = (M, E)$, where M – is the set of nodes and E – is the set of transmission paths in the network Figure (2) .



Figure(1). Example of MPLS-network structure.

According to MPLS engineering principles the whole set of nodes can be divided into two subsets: $M^+ = \{M_r^+, r = \overline{1, m_{LER}}\}$ – is the label edge routers subset (*LER*) and

$M^- = \{M_j^-, j = \overline{1, m_{LSR}}\}$ – is the label switching routers subset of (LSR) . Each arc $(i, j) \in E$ of the graph presents transmission path in the network and appropriate bandwidth φ_{ij} associated with this path. The set of received user (access networks) traffics K depending on which label edge router received can be decomposed into the subsets $\{K_r, r = \overline{1, m_{LER}}\}$, where K_r – is the set of traffics received by r -th LER . Then each traffic from the K_r -set has series of the following parameters:

M_r^+ – r -th LER which receives k -th traffic (source node);

M_p^+ – p -th LER via which k -th traffic leaves $MPLS$ -network (destination node);

λ^{k_r} – rate (speed) of the k_r -th traffic, i.e. k -th traffic which r -th LER receives.

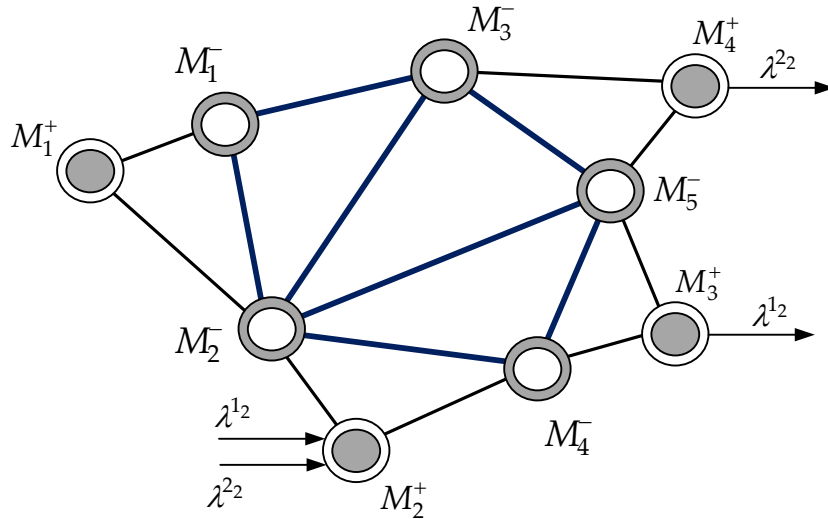


Figure (2). Graph model of MPLS-network.

For example, Figure (2) shows rates of two traffics (λ^{1_2} and λ^{2_2}) entering the second LER and destined for fourth and third LER respectively.

3. Functional description of MPLS-network

During the routing problems solving using flow-based models in $MPLS$ -network, it is required to calculate one or set of paths (*Label Switching Path, LSP*) between a pair of edge sender-receiver nodes and determine the traffic distribution order between them according to

given rate. Let's use two-level scheme of calculation to increase scalability of routing tasks solving:

on the lower layer – desired routes are calculated independently at each LER for the traffics that come to particular LER from subscribers (*network access traffic*);

on the upper layer – solutions obtained on the lower layer are coordinated in order to prevent the probable transmission paths overload in the network due to the routing decisions decentralization.

Then for each r -th LER routing variables $x_{ij}^{k_r}$ characterize traffic rate of the k_r -th traffic in the path $(i, j) \in E$. In order to prevent packet loss at the routers and in the network in general, during the routing variables calculation it is necessary to keep conditions of the flow conservation:

$$\begin{cases} \sum_{j:(i,j) \in E} x_{ij}^{k_r} - \sum_{j:(j,i) \in E} x_{ji}^{k_r} = \lambda^{k_r} & \text{if } k_r \in K_r, i = M_r^+; \\ \sum_{j:(i,j) \in E} x_{ij}^{k_r} - \sum_{j:(j,i) \in E} x_{ji}^{k_r} = 0 & \text{if } k_r \in K_r, i \neq M_r^+, M_p^+; \\ \sum_{j:(i,j) \in E} x_{ij}^{k_r} - \sum_{j:(j,i) \in E} x_{ji}^{k_r} = -\lambda^{k_r} & \text{if } k_r \in K_r, i = M_p^+. \end{cases} \quad (1)$$

The system of equations-conditions (1) should be executed for each traffic which enters any label edge router (LER). Besides, in order to prevent possible transmission path overload in MPLS-network it is important to fulfill following conditions (by number of transmission paths):

$$\sum_{r \in M^+} \sum_{k_r \in K_r} x_{ij}^{k_r} \leq \varphi_{ij}; (i, j) \in E. \quad (2)$$

Please note, that in case of decentralized routing variables calculation it's impossible to take into account condition (2) for each particular LER explicitly, because each edge router determines LSP for user traffic which comes without information about calculation results of the adjacent LER. Due to this let's write conditions (2) in the following form:

$$\sum_{k_r \in K_r} x_{ij}^{k_r} \leq \varphi_{ij} - \sum_{\substack{s \in M^+ \\ s \neq r}} \sum_{k_s \in K_s} x_{ij}^{k_s}; r \in M^+, (i, j) \in E. \quad (3)$$

Expression (3) means that the traffic, routed from r -th LER should not exceed available bandwidth in transmission path, which remained after traffics from other edge routers were served.

According to the physical meaning of the routing variables they should meet these requirements:

$$0 \leq x_{ij}^{k,r} \leq \lambda^{k,r}. \quad (4)$$

In vector-matrix form conditions (3) can be written as:

$$B_r \cdot \vec{x}_r \leq \sum_{\substack{s \in M^+ \\ s \neq r}} B_s \vec{x}_s. \quad (5)$$

During the vector \vec{x}_r variables calculation, a minimum of following goal function should be used as optimality criterion for obtained solutions:

$$\min_x F \quad \text{at} \quad F = \sum_{r \in M^+} \vec{x}_r^t H_r \vec{x}_r, \quad (6)$$

where H_r – diagonal positive matrix of channels metrics; $[]^t$ – vector (matrix) transpose operation.

Then, switching to an unconditional extreme problem it is necessary to maximize a Lagrangian by Lagrange multipliers (ρ and μ):

$$\min_x F = \max_\mu L,$$

Where,

$$L = \sum_{r \in M^+} \vec{x}_r^t H_r \vec{x}_r + \sum_{r \in M^+} \mu_r^t (B_r \cdot \vec{x}_r - \sum_{\substack{s \in M^+ \\ s \neq r}} B_s \vec{x}_s). \quad (7)$$

4. The goal coordination method usage for multilevel routing strategy implementation

To solve the formulated optimization problem let's use the method of the goal coordination [7, 8] for this purpose let's represent Lagrangian (7) in such form:

$$L = \sum_{r \in M^+} \vec{x}_r^t H_r \vec{x}_r + \sum_{r \in M^+} \mu_r^t B_r \vec{x}_r + \sum_{r \in M^+} \mu_r^t \sum_{\substack{s \in M^+ \\ s \neq r}} B_s \vec{x}_s. \quad (8)$$

Assuming that μ_r are constant, last item in expression (8) can be interpreted as:

$$\sum_{r \in M^*} \mu_r^t \sum_{\substack{s \in M^+ \\ s \neq r}} C_{rs} \bar{x}_s = \sum_{r \in M^+} \sum_{\substack{s \in M^+ \\ s \neq r}} \mu_r^t B_s \bar{x}_s ,$$

then expression (8) can be written as:

$$L = \sum_{r \in M^+} L_r ,$$

Where,

$$L_r = \bar{x}_r^t H_r \bar{x}_r + \mu_r^t B_r \bar{x}_r - \sum_{\substack{s \in M^+ \\ s \neq r}} \mu_s^t B_s \bar{x}_r \quad (9)$$

So, function (9) takes a separable form while general *MPLS*-network routing problem is decomposed with the set of routing problems (by the edge routers number) where each r -th *LER*'s routing problem which consists of vector \bar{x}_r calculation reduced to the minimization of the Lagrangian L_r . The expression (9) minimization task determines the lower calculation layer - *LER*-layer. On the upper layer (*LSR*-layer) the main task of which is the coordination of solutions obtained at the lower layer in order to avoid network transmission paths overload (2), modification of the Lagrange multipliers vector implemented during the following gradient procedure execution:

$$\mu_r(\alpha + 1) = \mu_r(\alpha) + \nabla \mu_r , \quad (10)$$

where $\nabla \mu_r$ – gradient of the function calculated using the solutions from the routing problems (\bar{x}_r^*) solving on the upper layer at each particular r -th *LER* ($r \in M^+$), i.e:

$$\nabla \mu_r(x) \Big|_{x=x^*} = B_r \bar{x}_r^* - \sum_{\substack{s \in M^+ \\ s \neq r}} B_s \bar{x}_s^* . \quad (11)$$

The general scheme of a two-level routing in *MPLS*-network is shown in the Figure (3).

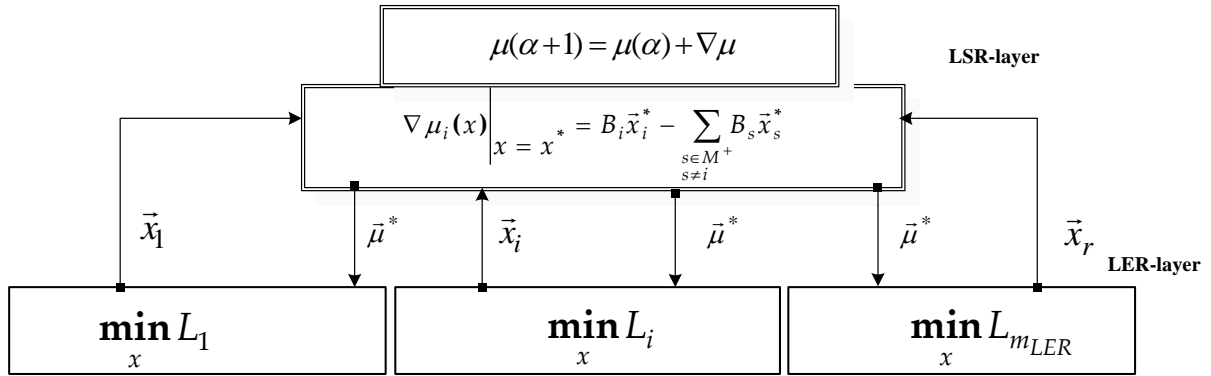


Figure (3). Computing circuit of two-layer routing in MPLS-network supporting traffic engineering technique.

5. Researching method hierarchical-coordination routing in MPLS-network

During the analysis of the hierarchical-coordination routing method structure and its content, it is necessary to notice that its effectiveness mostly determined by the rate of its optimal solution convergence when gradient (11) equals zero. For clarity and ease of calculations, convergence rate was measured by the number of iterative procedures (N_{it}) of Lagrange multipliers calculation on the second level of this method hierarchy. From the point of routing decision scalability the service traffic volume, including data about the network status and control information, was depended proportionally on the number of the coordinating procedure iterations. That is why it is important that the number of such iterations was minimal. The following network characteristics and parameters of the model were varied during the research as follows :

- Number of channels in the network core, i.e. between LSR-routers (N): from $N=3$ to $N=16$;
- Normalized network load (n), which means the ratio of external incoming traffic total rate to the total TCS bandwidth: from 0 to 0.95;
- Type of the objective function (OF), which may be linear [6] or quadratic (6).

According to results analysis, this method converges to the optimal solution at the average of 3-4 iterations as shown in Figure (4).

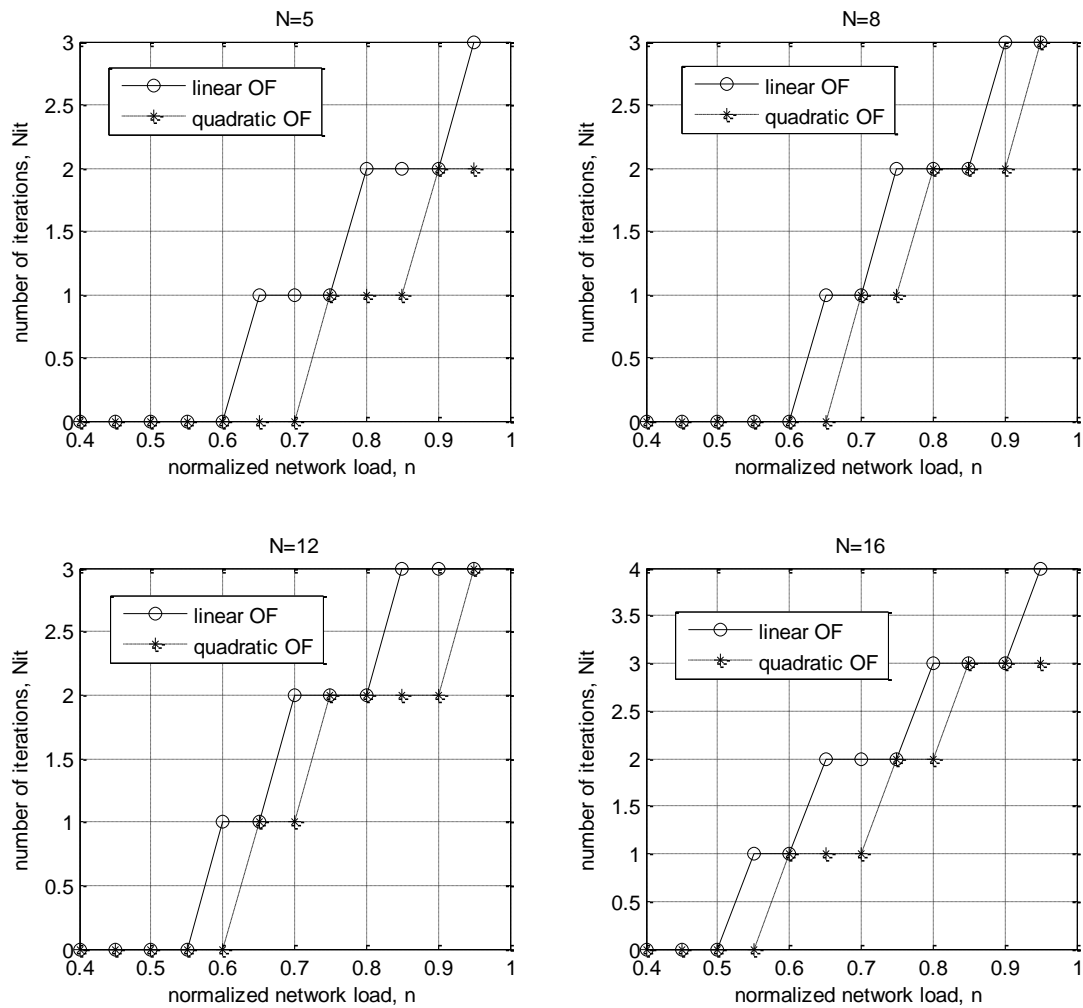


Figure (4). Analysis of the method convergence to the optimal solution for different network structures and network load.

Number of the coordinating procedure iterations (9)-(10) was increasing with the growth of the transmission channels number between the LSR-routers and the incoming traffic rate. Quadratic OF usage provides not such rapid increase of the iterations number as linear OF. Reducing iterations number was reached through more efficient load balancing, since using a quadratic objective function (6) in the routing model provides better load balancing compared to the linear OF optimization [6] at the same external load. It was due to linear OF usage during load increase. In this case the multipath routing strategy implemented with consecutive new path activation in case of currently used routes overloading. Simultaneous load balancing on all possible paths implemented when the quadratic OF used, which provides better utilization of network resources, at the same time the number of iterations (10) - (11) in the method decreased in order to avoid overloading

the TP network. Additionally, when we use the quadratic objective function the coordination process is improving (average at 5-10% more). In the case of the normalized network load $n \leq 0.5 \dots 0.55$ it was not necessary to coordinate solutions by the upper level, because it was enough to provide load balancing on the network paths to prevent TP TCS overloading.

6. Conclusion

Hereby, in this paper the flow-based model of a two-level routing in a MPLS-network proposed, which is represented by the expressions (1)-(6). During the mathematical model of routing optimization problem solving, the principle of goal coordination was used (7)-(11). Due to this, procedure of routing variables calculation acquired two-level character. On the lower layer (*LER*-layer) a set of paths for traffic entering *LER* is calculated and on the upper layer (*LSR*-layer) solutions obtained on the *LER*-layer (routing variables) were coordinated in order to prevent transmission path's overload. The functions of the coordinator in the MPLS-network may be assigned to one of the transit routers.

The main purpose of the proposed two-level solution implementation is to increase the scalability of flow-based routing strategies because usage of the centralized schemes is inertial and resource-consuming while MPLS-network dimension grows. The benefit of goal coordination method usage is simplicity of computational problems (10) - (11) on the *LSR*-layer as in accordance with the paradigm of «stupid network» maintained in MPLS-networks, all «intellectual» functions are concentrated on edge routers (*LER*-layer). In the case of considering MPLS-network as a set of interconnected sub networks the routing process can also be interpreted as a multi-level with additional hierarchical levels allocation.

7. References

- [1] *Olveĭn V.* The structure and implementation of modern technologies MPLS. Publisher: Vilyams, Dialektika, 2004, Serie: Cisco Press. – 480 p.
- [2] *Álvarez S.* QoS for IP/MPLS networks. – Cisco Press, 2006. – 299 p.
- [3] *Simha A., Osborne E.* Traffic Engineering with MPLS. Cisco Press, 2002. – 608 p.
- [4] *Medhi D., Ramasamy K.* Network routing: algorithms, protocols, and architectures. – Morgan Kaufmann Publishers, 2007. – 788 p.

- [5] *Pióro M., Medhi D.* Routing, Flow, and Capacity Design in Communication and Computer Networks. – Morgan Kaufmann, 2004. – 765 p.
- [6] *He T., Wang S., Zhang M.* A Routing Algorithm for Traffic Engineering in MPLS Networks // Journal of Nanjing University of Posts and Telecommunications(Natural Science). – 2010. – P. 381-395.
- [7] *Na Lin, Tao Yang, Li-xue Song.* A New QoS Multicast Routing Algorithm for MPLS-TE // International Conference on Measuring Technology and Mechatronics Automation icmtma – 2010. – Vol. 1. – P.192-195.
- [8] *Oubaha J., Habbani A., Elkoutbi M.* Multi-criteria path optimization in MPLS networks / J. Oubaha, A. Habbani, M. Elkoutbi // Communications and Mobile Network (ISVC) – 2010, 5th International Symposium. – 2010. – P. 1-4
- [9] *Burns J. E., Ott T. J., De Kock J. M., Krzesinski A. E.* Path selection and bandwidth allocation in MPLS networks: a non-linear programming approach // Proc. Internet Performance and Control of Network Systems, 2003. - Vol. 52. - Issues 2-3. – P. 133-152.
- [10] *Cherubini D., Fanni A., Mereu A., Frangioni A., Murgia C., Scutellà M.G., Zuddas P.* Linear programming models for traffic engineering in 100% survivable networks under combined IS-IS/OSPF and MPLS-TE / D. Cherubini, A. Fanni, A. Mereu, A. Frangioni, C. Murgia, M.G. Scutellà, P. Zuddas // Computers & Operations Research. – Vol. 38, issue 12. – 2011. – P. 1805-1815.
- [11] *Lemeshko O.V. Ahmad M. Hailan, Starkova O.V.* Multi-level traffic management in the MPLS-TE DiffServ network // 11-th International Conference «The experience of designing and application of CAD systems in microelectronics» Polyana-Svalyava-(Zakarpattya), UKRAINE 23 - 25 February 2011: Publishing House of Lviv Polytechnic, 2011. – P. 118-120.
- [12] *Lemeshko O., Ahmad M. Hailan, Ali S. Ali.* A flow-based model of two-level routing in multiservice network // Modern Problems of Radio Engineering, Telecommunications and Computer Science. Proceedings of the international Conference TCSET'2010. – Lviv-Slavsko: Publishing House of Lviv Polytechnic, 2010. – P. 225.
- [13] *Mesarovic M.D., Macko D., Takahara, Y.* Theory of hierarchical multilevel systems, Academic Press, New York and London, 1970. – 294 p.
- [14] *Systems: decomposition, optimisation, and control / edited by M. G. Singh, A. Titli,* and Laboratoire d'automatique et d'analyse des systemes du C.N.R.S. Oxford; New York: Pergamon Press, 1978. – 645 p.

Experimental Study of Fluid Flow Through Packed Beds of Glass Sphere Packing

Mohammed N. Latif

Nahrain University
College of Engineering

Head of Medical Engineering Department

Iraq- Baghdad-Jadriya

P.O.Box.64040

Wekar Abd Al-Wahed

Nahrain University
College of Engineering
Chemical Engineering
Department

Iraq- Baghdad-Jadriya

P.O.Box.64040

Zainab Talib Abidzaid

Al-Mustansiryiah University
College of Engineering
Environmental Engineering
Department

Iraq - Baghdad /Bab-AL-

Muthem/P.O. Box 14150

Zainab_talib2009@yahoo.com

Abstract

Fluid flow through packed bed has many important applications in chemical and other process engineering fields such as fixed-catalytic reactor, adsorption of a solute, gas absorption, combustion, drying, filter bed, wastewater treatment and the flow of crude oil in petroleum reservoir.

The present work presents the study of air flow through a packed bed of glass sphere packing with 0.42, 0.50, 0.61, 0.79 and 1.01 cm in diameter, and the packed column was 7.62 cm in diameter and 57 cm long. Different flow rates of fluid were used which expressed by modified Reynolds number. Many variables were studied in this work such as fluid type (air flow), flow rate and the packing porosity, in order to study the effect of these variables on the friction factor.

Anew correlation for friction factor as a function of Reynolds number for air flow through packed of mono size packing has been made.

The results showed that the pressure drop through a packed bed is highly sensitive to the packing porosity which has a significant effect on the friction factor. It was found that as the bed porosity increases the friction factor values as well as the pressure drop values decrease.

Key Words: Friction Factor, Packed Bed, Reynolds Number, Porosity, Air Flow.

الدراسة العملية لجريان الموائع خلال العمود الحشوي المحشو بجسيمات زجاجية كروية الشكل

المستخلص

جريان الموائع خلال الاعمدة المحشوة لها تطبيقات مهمة في الهندسة الكيميائية والفروع الهندسية الاخرى، مثل المفاعلات المحفزة والامتزاز من المذاب، امتصاص الغاز، والاحتراق، والتجفيف، وتصفية السريير، ومعالجة مياه الصرف الصحي وتدفق النفط الخام في المكامن النفطية.

تم في هذا البحث دراسة جريان الهواء خلال عمود حشوي محشو بجسيمات زجاجية كروية الشكل وبأقطار 0.42, 0.5, 0.61, 0.79 و 1.01 سم، وكان قطر العمود المحشو 7.62 سم وطوله 57 سم. كما استخدمت عدة سرع لمعدل الجريان الموائع والممتلئة بعدد رينولدز. لقد تم دراسة عدة عوامل خلال هذا العمل كنوع المائع (جريان الهواء)، سرعة الجريان وتغير مسامية الحشوة لمعرفة تأثير هذه العوامل على معامل الاحتكاك.

تم ايجاد علاقة تجريبية جديدة تربط بين معامل الاحتكاك ورقم رينولدز لجريان الهواء خلال العمود الحشوي استناداً على تجاربنا العملية.

اثبتت نتائج الدراسة ان هبوط الضغط خلال عمود حشوي يتأثر لدرجة كبيرة بمسامية الحشوة والتي لها تأثير ملموس على معامل الاحتكاك. حيث لوحظ انه عندما تزداد مسامية الحشوة تقل قيم معامل الاحتكاك، وبالتالي تقل قيمة هبوط الضغط.

1- Introduction

The study of fluid flow through the packed bed is an important issue. Chemical engineering operations commonly involve the use of packed and fluidized beds. These are devices in which a large surface area for contact between a liquid and gas (absorption, distillation) or a solid and a gas or liquid (adsorption, catalysis) is obtained for achieving rapid [1].

A packed bed is simply a vertical column partially filled with small media varying in shape, size, and density. A fluid (usually air or water) is passed through this column from the bottom and the pressure is measured by two sensors above and below the packed bed [2]. Packed beds are consists of a channel or duct which contains some form of porous material or a collection of randomly packed spheres or other non-spherical particle [3]. The packing material may be glass marbles, ceramics, plastics, pea gravel, or mixtures of materials [4]. It should have a large void volume to allow flow of fluid without excessive pressure drop and it should be chemically inert to fluids being processed [5]. The advantage of using packed column rather than just tank or other reaction vessel is that the packing affords a large contacting surface area for fluids to flow. Usually increased surface area provides a high degree of turbulence in the fluids which are achieved at the expense of increased capital cost

and/or pressure drop, and a balance must be made between these factors when arriving at an economic design [6]. The fluid path is made of many parallel and interconnecting channels. The channels are not of fixed diameter but widen and narrow repeatedly, and even twist and turn in varying directions as the particles obstruct the passageway [7]. Owing to the complicated nature of the flow channels in granular bed, there should not be a sharp transition from laminar to turbulent flow as occurs in pipe flow. Rather there should be a smooth transition from laminar flow throughout - to laminar flow in parts of the granular bed and turbulent flow in other parts - to turbulent flow throughout [8]. The flow rate of fluid is important factor affecting on the pressure drop through packed bed. When there is no flow through the packed bed, the net gravitational force acts downward. When fluid flows upwards, friction forces act upward and counter balance the net gravitational force [9, 10]. From the reading of the manometers, Coulson in 1949 found that the difference in pressure over varying thicknesses of the packing was obtained directly. Some results for bed of spherical particles are shown graphically in Fig 1. The experimental points are seen to lie on straight lines indicating a linear relation between Δp and L . Figure 1 also shows similar results for beds of other material [11].

The fluid flow through packed bed has attracted considerable attention from many investigators; they have shown that the most important issue for mechanical perspective for liquid or gas flow through packed bed depends on the pressure drop and friction [2]. The first carefully documented friction experiments have been carried out by **Hagen** in 1839 for laminar flow [12]. **Schoenborn and Dougherty in 1944** studied the flow of air, water and oil through beds of various commercial ring and saddle packing [13]. **Harkonen in 1987, Lindqvist in 1994, Lammi in 1996, Wang and Gullichsen in 1999 and Lee and Bennington in 2004** measured the average void fraction and flow resistance through packed columns. They found that the pressure drop of liquid through a packed bed depends on many factors, including the particle species and the type and size distribution of the particles. An attempt has been made by **Yu and Standish in 1989** to establish general theory of the random packing of particles. They developed an analytical model based on the experimental results of binary mixtures [14]. **Basu et. al. in 2003** studied the effect of various velocity range on the packed bed column and took their observations of the packing height and pressure drop in the column [15].

The packing of solid particles has been studied more or less continuously for a number of years. The first study of the modes of packing of spheres appears to have been undertaken by **Sticker in 1899** [8]. **Furnas in 1931** [15], **Westman 1930** [17], studied the packing of a bed

of different sizes solid particles [10]. **Graton in 1985** [17] studied the packing of spheres led to the much-quoted limits of porosity for regular packing of single-size spheres.

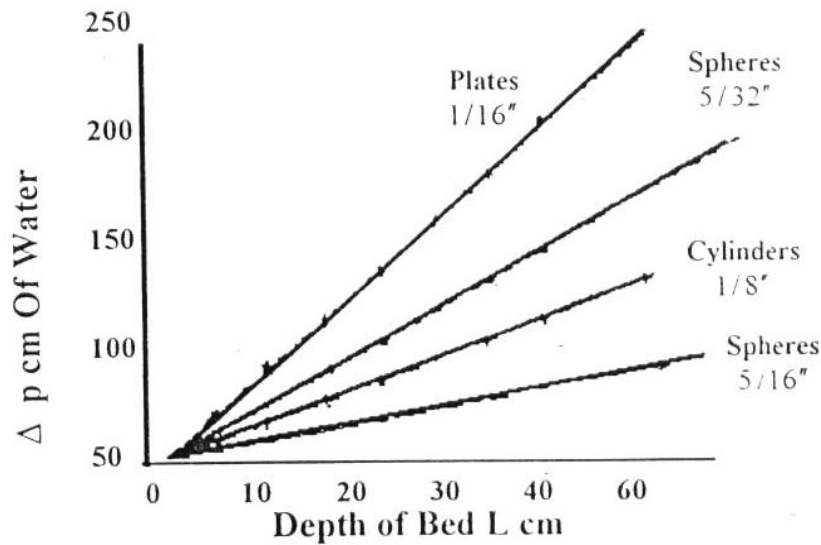


Figure (1). Relation between depth of bed and pressure drop.

Many studies have been done in correlating data for packed columns at higher fluid velocities. **Blanke** in 1926 suggested that this change of relationship between pressure drop and velocity is entirely analogous to that which occurs in ordinary pipes and proposed a friction factor plot similar to that of Stanton [18]. The equation used was that for kinetic effect modified by a friction factor, which is turn, is a function of Reynolds [19].

$$\Delta p = 2f(\rho u^2 / D_p) \quad (1)$$

$$f = \phi(NRe) \quad (2)$$

Some workers have included the effect of void fraction by the addition of another factor in equ. 2. It is usually given in the form $(1-\epsilon)^m/\epsilon^3$ where m is either 1 or 2.

Carman in 1938 and Kozeny in 1927 suggested that the change of relationship between pressure drop, void fraction effect and velocity, and proposed a friction factor for entire Reynolds number by plotting on a logarithmic basis [20]. Carman correlates his data of the friction factor as a function of the Reynolds number for condition of fixed bed operation; the main variables are the velocity, particle diameter, pressure drop per unit length and fraction voids. Carman correlation for fluid flow through randomly packed beds of solid particles by a single curve whose general equation was:

$$f = 5Re_1^{-1} + 0.4Re_1^{-0.1} \quad (3)$$

Where Re_1 is the modified Reynolds number and can be expressed in the following equation:

$$Re_1 = \frac{\rho u}{S(1-e)\mu} \quad (4)$$

And S is the specific surface area of the particles and is the surface area of particle divided by its volume. Its units are $(\text{length})^{-1}$. For sphere:

$$S = \frac{\pi d_p^2}{\pi(d_p^3/6)} = \frac{6}{d_p} \quad (5)$$

The general surface of a bed of particles can often be characterized by the specific area of the bed (S_B) and the fractional voidage of the bed (ϵ). S_B is the surface area presented to the fluid per unit volume of bed when the particles are packed in bed. Its units are $(\text{length})^{-1}$. It can be seen that S and S_B are not equal due to the voidage occurring when the particles are packed in to a bed. If contact points occur between particles so that only a very small fraction of surface area is lost by overlapping, then [8]:

$$S_B = S(1-\epsilon) \quad (6)$$

For a given shape of particle S increases as the particle size is reduced. When mixtures of sizes are studied the value of S for sphere of mixed sizes is given by [21]:

$$S = 6(1-\epsilon) \sum \frac{x_i}{d_{pi}} \quad (7)$$

Where: x_i is the fractional weight of spherical particle; d_p is the diameter of spherical particle.

Sawistowski in 1957 has compared the results obtained for flow of fluids through beds of hollow packing and has noted that equation 3 gives lower values of friction factor for hollow packing [22]. Thus, Sawistowski modified equation 3 as:

$$f = 5Re_1^{-1} + Re_1^{-0.1} \quad (8)$$

Ergun in 1952 studied the pressure drop and friction factor through packed beds composed of uniform spherical particles [9]. His model was also used for non-spherical shape

and/or the particle size distribution was non-uniform [2]. His equation can provide the pressure drop along the length of the packed bed given a fluid velocity:

$$f = 4.17 \text{Re}_1^{-1} + 0.29 \quad (9)$$

Many attempts to study the effect of surface roughness on the friction factor have shown that the variable has a significant effect but no quantitative method of evaluating the effect has been formulated. **Leva in 1949** carried out important experiments using three different groups of materials. He used glass and porcelain as smooth particles, clay and Alundum as rough materials, Aloxite and MgO granules as rougher materials. The degree of the materials roughness was described qualitatively (as a result of his tests). This method of description does not help in the development of a quantitative correlation between the relative roughness (ϵ/d) and the friction factor. Leva expressed equations for the friction factor of these materials as follow. For smooth materials the expression was:

$$f = \frac{1.75}{\text{Re}_1^{0.1}} \quad (10)$$

For rough materials the expression was:

$$f = \frac{2.625}{\text{Re}_1^{0.1}} \quad (11)$$

Whilst for rougher materials the expression was:

$$f = \frac{4.0}{\text{Re}_1^{0.1}} \quad (12)$$

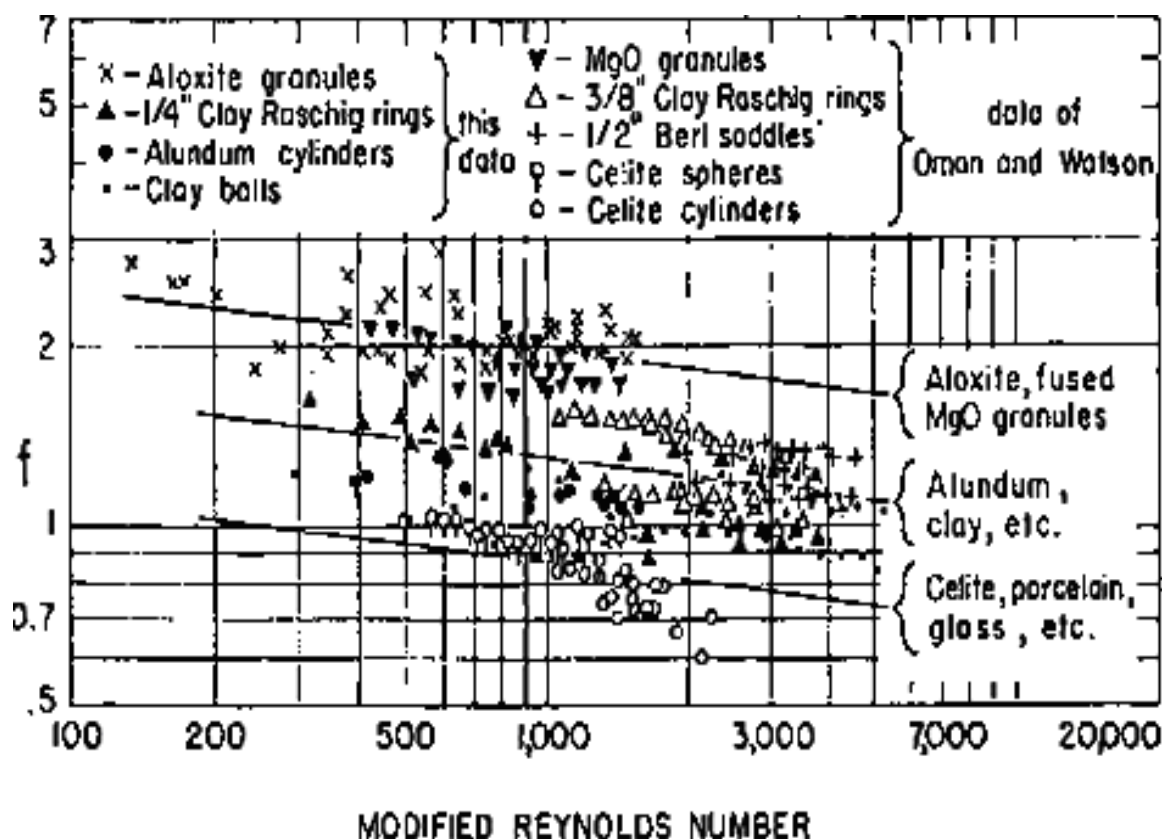


Figure (2). Friction factor for various materials [23].

Figure (2) shows that the friction factor through packed beds is approximately doubled when the degree of surface roughness was increased from that represented by porcelain to the roughness of Aloxite granules [23]. These expressions do not include the relative roughness (ϵ/d) and can only therefore be used for the materials that were used. Leva concluded (from previous expressions) that the degree of surface roughness had no effect on the slope of the $\log f - \log Re$ curve between the limits of Re from 130 to 7000 which covered the range was used [24].

Aim of the work:

The aim of this work is to propose an empirical correlation between friction factor and Reynolds number for air flow through bed of spheres, and study the effect of particle size distribution on the bed porosity. Also studying the effect of bed porosity on the pressure drop and friction factor through the packed bed.

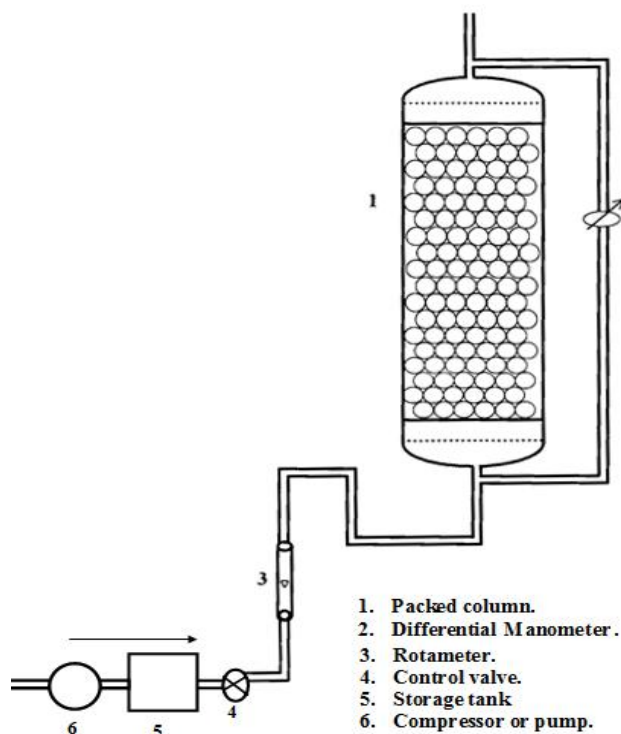
2- Experimental work

In this work five sizes of spherical glass particles were used. The spherical particles diameters were 0.42, 0.51, .61, 0.79 and 1.01cm. The fluid used was air, the properties was

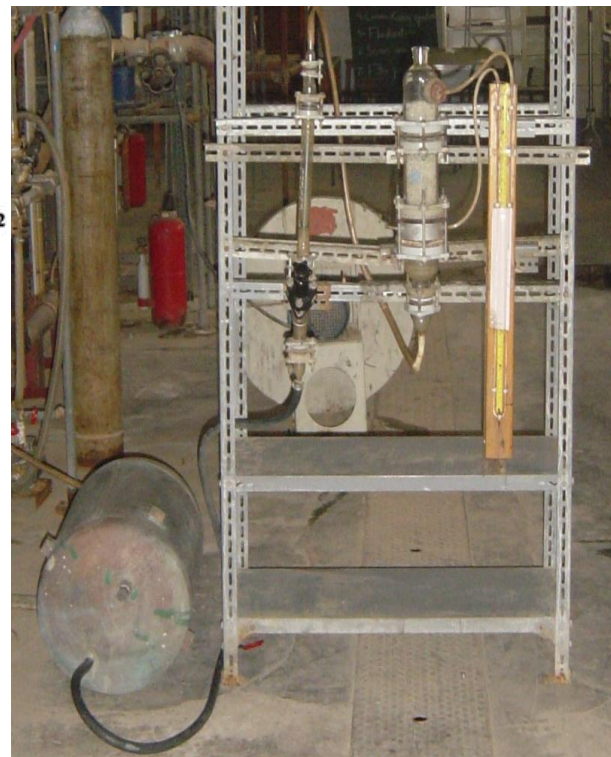
taken at city temperature (31°C). The physical properties of air at this temperature are density 1.1582 kg/m³ and viscosity 1.88×10^{-5} kg/m.s.

A schematic diagram of the apparatus used is shown in Figure 3. The packed bed column was made of Pyrex glass tube (Q.V.F) 7.62 cm inside diameter and 57 cm height. The Q.V.F glass contains two taps at the inlet and outlet of the column. The taps used for measuring the pressure drop are placed flush to the inside surface to determine the static pressure actuarially. The first one was placed downstream at a distance 1 cm from the sieve entrance regional and the second tap was placed at distance 1cm from the top sieve of the column. The distance between the inlet and outlet to the column and the sieve was to avoid the turbulence at the bed. The column was mounted vertically and holds by iron flanges.

Air flow is produced by a compressor to the packed column. The compressor contained a vane rotary type driven by AC motor. The compressor was used to supply the air to packed bed at constant pressure. A storage tank was used to receive air from the compressor and provide it to the rotameter. A rotameter was used for measuring air flow rate, and the flow rate up to 16 cubic meters per hour. The U-tube manometer (with ethanol) was used for measuring the pressure drop through packed column.



A- Apparatus diagram



B- Photographic picture of air flow through packed bed

Figure (3). Air flow through packed bed.

The particles were poured into the column until it was filled and the bed porosity was determined using the following equation:

$$\varepsilon = 1 - \frac{\rho_b}{\rho_t} \quad (13)$$

Where: ρ_b is the bulk density (g/cm^3), ρ_t is the true density of particles (g/cm^3).

The air was provided by the compressor and its flow rates up to 16 cubic meters per hour. It was controlled by means of a control valve at the inlet of the rotameter. The average velocity of the air was obtained from rotameter using equation 14.

$$u = \frac{Q}{A} \quad (14)$$

Where Q is the flow rate of fluid (m^3/hr), A is the bed cross-sectional area (m^2).

The rotameter valve was opened for air flow. The rotameter float was ensured to achieve steady state, and the pressure drop across the bed was measured using u-tube manometer. The friction factor was obtained from pressure drop using the following equation [5]:

$$\frac{R_1}{\rho u_1^2} = \frac{\varepsilon^3 (-\Delta p)}{S(1-\varepsilon)L\rho u^2} \quad (15)$$

Bulk density is defined by the following expression:

$$\text{bulk density}(\rho_b) = \frac{\text{weight of the bed}}{\text{volume of bed}} \quad (16)$$

For a cylindrical bed

$$\text{volume} = \frac{\pi}{4} D^2 L \quad (17)$$

Where: D =inside diameter of the cylinder (cm), L =level of the particles in the bed (cm).

The true densities of particles were determined using shifted water method. To obtain the volume of samples a known weight of particles was immersed in a graduated cylinder (with capacity of 500 ml) filled with water. The weight of container was measured using a sensitive balance first when the container filled with water only and second when it contains the particle besides the water. In both cases, water level inside the container was carefully

maintained at it permissible full mark level. Using the following equation, true density of particles was being determined.

$$\rho_t = \frac{w_1 \times \rho_w}{w_2 - w_3 + w_1} \quad (18)$$

Where: ρ_w = water density at laboratory temperature (g/cm^3), w_1 = solid particles weight (g), w_2 = weight of cylinder filled with water (g), w_3 = weight of cylinder with water and particles (g).

For mixture of particles, the mixture true density (ρ_{tm}) can be determined from the following equation:

$$\rho_m = \frac{1}{\sum_{i=1}^m \frac{x_i}{\rho_{ti}}} \quad (19)$$

Where x_i is the weight percent of component i, ρ_{ti} is the true density of component I (g/cm^3).

3- Result and discussion

The values of friction factors for air flow through beds of mono sizes particles are plotted versus Reynolds numbers as shown in Figures (4-8). These Figures show that the friction factor decreases as Reynolds number increases.

The wall affects the bed porosity and increases its value. This appears in Figure (8) where the bed porosity increases to a value of 0.4359, this wall effect may be due to the ratio of bed diameter (7.62cm) to the particles diameter (1.01 cm) which is less than the supposed ratio (column diameter to the particle diameter should be greater than 10:1).

Figures (4 – 8) show that the values of friction factor of Figure (4) decrease sharply with increasing Reynolds numbers while that of Figure (8) decrease slightly with increasing Reynolds number, because the fluid flow of Figure (4) is at the laminar and transition regions (where the friction factor-Reynolds number curve is of slope of -1) while the fluid flow of Figure (8) is at the transition and turbulent regions (where the friction factor-Reynolds number curve become straighter).

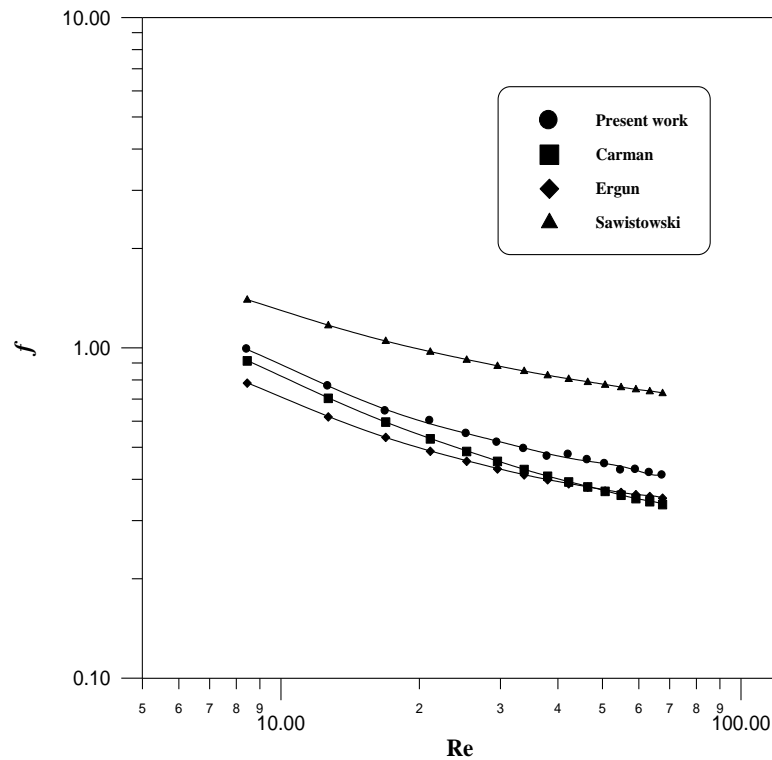


Figure (4). Friction factor versus Reynolds numbers for particles diameter of 0.42 cm and porosity of 0.3746 .

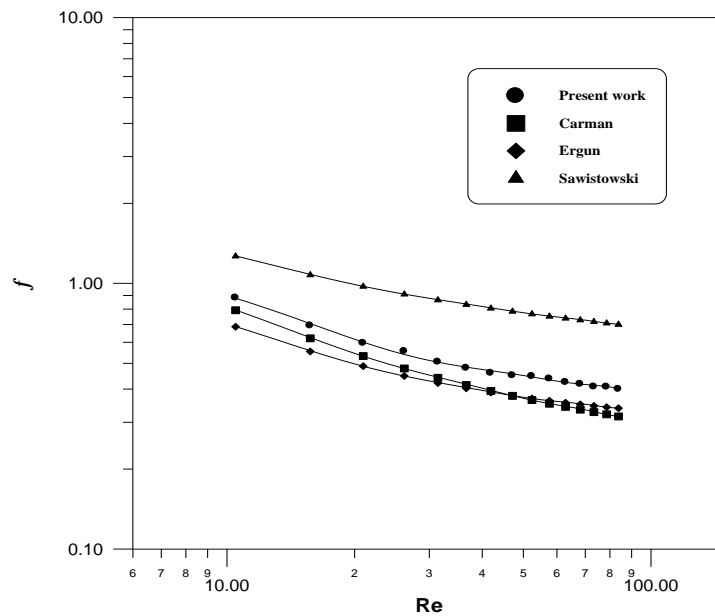


Figure (5). Friction factor versus Reynolds numbers for particles diameter of 0.51 cm and porosity of 0.3999 .

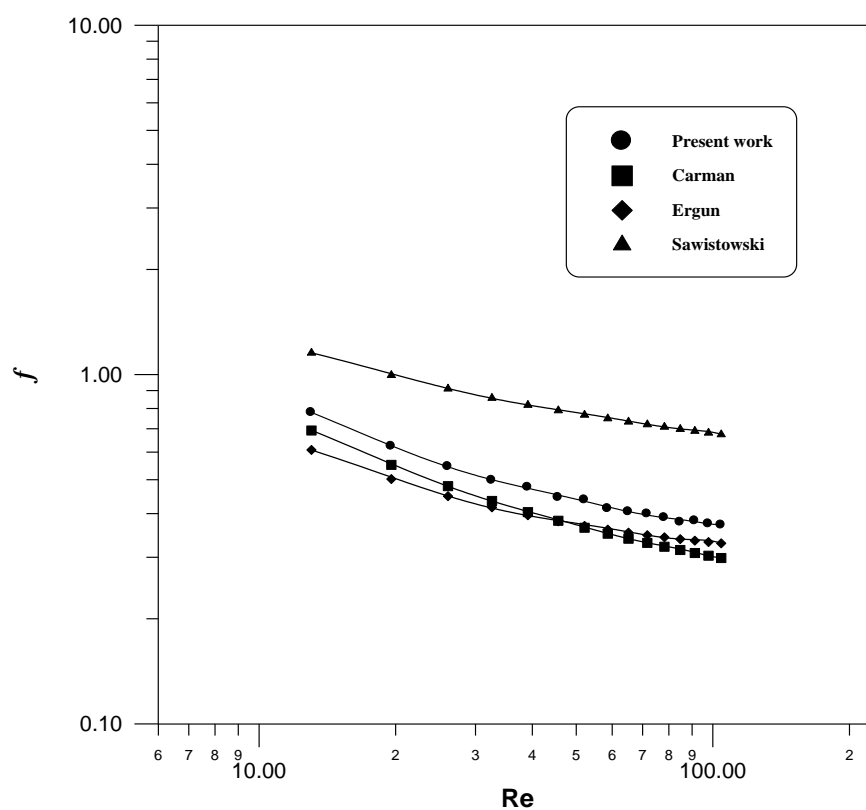


Figure (6). Friction factor versus Reynolds numbers for particles diameter of 0.61 cm and porosity of 0.4112.

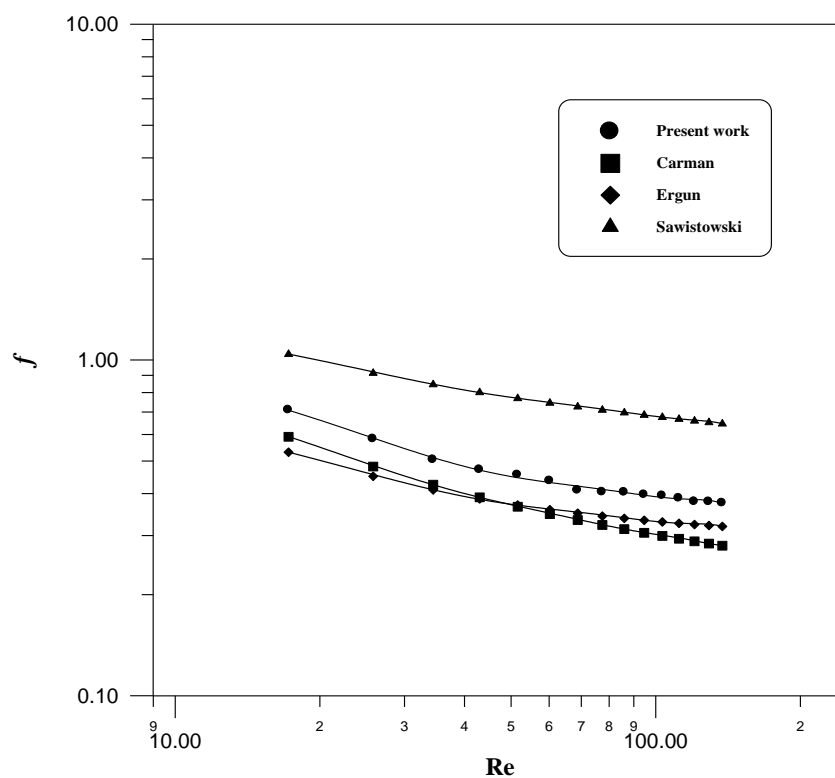


Figure (7). Friction factor versus Reynolds numbers for particles diameter of 0.79 cm and porosity of 0.4225

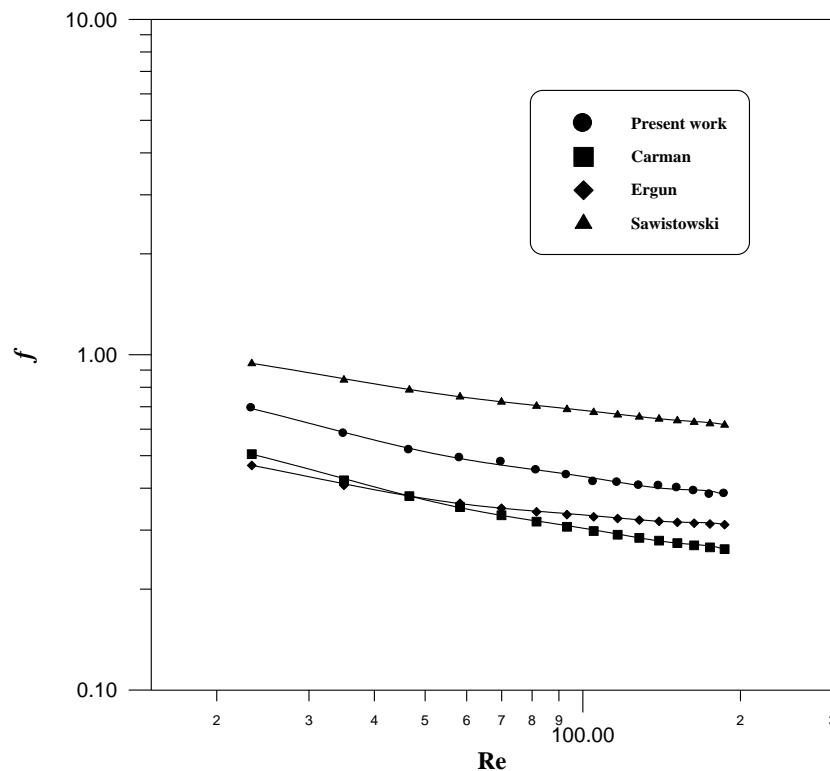


Figure (8). Friction factor versus Reynolds numbers for particles diameter of 1.01 cm and porosity of 0.4359

The difference between the experimental results and the results of Ergun, Carman and Sawistowski, this is may be due to the fact that Ergun and Sawistowski used hollow packings which have certain values of sphericity and porosity (the lower the particle sphericity the more open is the bed) while Carman used sphere packing [9, 20, 22].

It is clear that as the porosity decreases the friction factor decreases [25], in spite of pressure drop increases, and this is because that the friction factor is proportional to power three with porosity, while it is proportional to power one with pressure drop as shown in the equation below:

$$f = \frac{\Delta P}{L} \frac{d_p}{\rho u^2} \left(\frac{\varepsilon^3}{1 - \varepsilon} \right)$$

The best fitting of the experimental results for air flow through beds of mono-sizes particles is represented by the following equation.

$$f = 4.4296 Re^{-1} + 0.5489 Re^{-0.1}$$

With the correlation coefficient is 0.96 and percentage of average errors is 3.446 %.

4- Conclusion

The experimental results show that the friction factor decreases as Reynolds number increases. Examining the experimental results it can be seen that the pressure drop in the bed is inversely proportional to bed porosity for the same velocity of the fluid entering the bed.

The curves representing the experimental results of friction factor for air flow indicate that the air flow was intermediate between the turbulent and laminar regions (at the turbulent region the Reynolds number have insignificant effect on the friction factor values).

The bed porosity highly affects the pressure drop and inversely proportional to it, this is because that when the porosity increases the resistance to fluid flow through the bed decreases.

5- Reference

- [1] Subaramainian R. S., 2007, "Flow through Packed Beds and Fluidized Bed ". Article given on the internet at the web site: www.clarkson.edu/subramanian/ch301/notes/packfluidbed.pdf
- [2] Basu S. , Dixon C., Fereday C., Mueche A., and Perry T., "Comparison of the Ergun equation with experimental values regarding pressure drop and fluid velocity", The Canadian Journal of Chemical Engineering, Vol. 81, No. 2, 2003.
- [3] Pan G. and Yun H., "Flow in Packed Beds". Carnegie Mellon University (2005). Article given on the internet at the web site: http://rothfus.cheme.cmu.edu/tlab/pbeds/projects/t5_s04/t5_s04.pdf
- [4] Chung P., Koontz R., and Newton B., "Packed beds: Pressure drop versus fluid velocity and the Ergun equation" (2002). Article given on the internet at the web site: http://rothfus.cheme.cmu.edu/tlab/pbeds/projects/t10_s02/t10_s02.pdf
- [5] Foust A. S., Wenzel L. A., Clump C. W., Maus L., and Andersen L. B., "Principles of Unit Operations", Second Edition, John Wiley and Sons, New York, 1980.
- [6] Saw E. and Yang A., "Pressure Drop for Flow through Packed Beds", (2004). Article given on the internet at the web site: http://rothfus.cheme.cmu.edu/tlab/pbeds/projects/t4_s04/t4_s04.pdf
- [7] McCabe W. L., Smith J. C. and Peter Harriott, "Unit Operation of Chemical Engineering", Sixth Edition, McGraw-Hill, new York, 2001.
- [8] Gary W. A., "The packing of solid particles", Chapman and Hall, First published, London, 1968.

- [9] Ergun S., chem. Eng.Prog, 48(1952)89.
- [10] Schwartz C. E. and Smith J. M., Ind. Eng. Chem, 45 (1953) 1209.
- [11] Coulson J. M., Inst. Chem. Eng, 13 (1949) 237.
- [12] Suter S. P. and Skalak R., "The history of Poiseuille's law, "Annual Review of Fluid Mechanics, Vol. 25, 1993, pp. 1-19.
- [13] Mursh R. E., "Pressure Drop in Packed Beds of Spheres", (2003).
- [14] Yu A. B. and Standish N., powder technology, 55 (1989) 171.
- [15] Furnas C. C., Ind. Eng. Chem, 23 (1931) 1052.
- [16] Westman A. E. and Hugill M. R., J. Am. Ceram. Soc, 13 (1930) 767.
- [17] Gratton L. C. and Fraser H. J., J. Geol, 43 (1985) 785.
- [18] Blank F. C., Trans. Amer. Inst. Chem, 14 (1926) 415.
- [19] Orning A. A., Ind. Eng. Chem, 41 (1949) 1179.
- [20] Carman P. C., " Fluid flow through a granular bed". Trans. Inst. Chem. Eng, 15 (1938) 153.
- [21] Coulson J.M. and Richardson J.F., " Chemical engineering", volume II Third Edition, Pergama press, Oxford, 1985.
- [22] Sawistowski H., Chem. Eng. Sci, 6 (1957) 138.
- [23] Leva M. X. Max, Chem. Eng, 13 (1949) 115.
- [24] Saied N. Y., M. SC. Thesis, "The effect of particle surface roughness on hydraulic flow through granular media", Bradford University, 1977.
- [25] G. Meyer and Lincolnt, A. I. Ch.E.J, 13 (1936) 11.

6- Notations

Symbols

Notations

K''	=	Kozeny constant
Δp	=	Pressure drop through packed bed (kg/m.s ²)
u	=	Superficial velocity (m/s)
L	=	The height of packing in the bed (m)
Q	=	Flow rate (m ³ /hr)
S	=	Specific surface area of the particles (m ² /m ³)
S_B	=	Specific surface area of the bed (m ² /m ³)
A	=	The bed cross-sectional area (m ²)
d_p	=	Diameter of the particle (m)

d_{pav}	=	Average particles size (m)
d_{pi}	=	Diameter of particle i in mixture (m)
D	=	Diameter of cylinder (m)
Re_l	=	Modified Reynolds number
e	=	Porosity of the bed
$\frac{R_l}{\rho u_1^2}$	=	Modified friction factor
u_1	=	Average velocity through the pore channels (m/s).
L'	=	Length of channel (m)
d_m	=	Equivalent diameter of the pore channels (m)
K'	=	Is a dimensionless constant whose value depends on the structure of the bed
X_i	=	The proportion of the component i in the mixture
x_i	=	The weight fraction of particle i
f_w	=	Correction factor
S_c	=	Surface of the container per unit volume of bed (m^{-1})
d_t	=	Diameter of tube (m)
f	=	Modified friction factor
q	=	Number of components in the mixture
a	=	Representation of packing and fluid characteristics at laminar flow
b	=	Representation of packing and fluid characteristics at turbulent flow

Greek Symbols

ε	=	Porosity of the bed
ρ_b	=	Bulk density (g/cm^3)
ρ_t	=	True density (g/cm^3)
ρ_{tm}	=	True density of mixture (g/cm^3)
ρ_{ti}	=	True density of component i
ρ	=	Density of fluid (kg/m^3)
μ	=	Fluid viscosity ($kg/m.s$)
\emptyset_s	=	Sphericity
δ	=	orientation factor
θ	=	angle of the solid liquid interface with the stream direction

Effect of Bentonite Mudcake on the Interface Between Sandy Clay and Concrete

Ressol R. Shakir

Civil Engineering Department

College of Engineering

Thi-Qar University

Abstract

This paper presents investigation of behavior of bentonite mudcake between soil and concrete. A number of simple shear test have been performed on sandy clay and concrete specimens with and without bentonite mudcake at contact. The constitutive relations such as stress-displacement, dilative and the strength relations have been discussed in details. It was found that thin bentonite mudcake between sandy clay and concrete increases the shear strength, the sliding between soil and concrete in addition to the vertical displacement. The bentonite mudcake has a dual reaction; the upper face interacts with soil and the lower face interacts with concrete, showing different effects.

Keywords: Bored pile ; Bentonite mudcake; constitutive relations; sandy clay; concrete; compressibility; shear strength.

1. Introduction

Large Bored pile foundations are widely used to support heavy buildings around the world. Construction bored piles often needs using bentonite slurry to stabilize the borehole throughout construction. Using bentonite slurry may form weak layer between soil strata and concrete and this may diminish the capacity of the bored piles [1].

Construction period and bentonite slurry properties are main parameters influence the bearing capacity of bored pile. Many researches show that for short time of construction (less than 24 hours), bearing capacity does not decrease [2, 3, 4]. Increasing time of construction causes weak layer of bentonite that could not be removed through concrete pour. Properties of bentonite slurry such as viscosity is an important factor because it determines the degree of replacement of concrete tremie concreting [3, 4, 5, 6].

Maintaining the properties of the slurry within tolerable limits and placing the concrete in the same day of construction may decrease excessive filter cake occurrence and solve the problem of reducing skin friction [3]. However, contribution from recently researches did not

endorse this recommendation. For instance, Brown 2002 [7] showed that reduction in side resistance occurs even if the construction is achieved in short time interval. Zhang et al, 2009 showed that mudcakes have high water content, higher void ratio, high compressibility, low friction and low shear strength compared to in situ soil. Besides, the situation of bored pile construction mostly does not help the engineer to construct in time and within tolerable limits of slurry properties. Effect of bentonite slurry on the bearing capacity is doubt. Accordingly, to that, systematic study about the interaction of bentonite between soil and concrete is involved and constitutive relation of the behavior would be demonstrated.

Direct shear and simple shear test are widely used to study the soil structure interface, however, studying the effect of bentonite on interfacial shear strength using simple shear test are not available. Recently, a direct shear apparatus has been used to study concrete rock interface and sand-steel interface [8, 9]. Shakir and Zhu [10] used a simple shear apparatus to study the interface between compacted clay and concrete, and between compacted soil and different concrete surfaces [11]. The simple shear test is more convenient to investigate the effect of bentonite since it is simple for use and can measure the sliding and deformation in split form.

In this research, there are two questions; how the mudcake can affect the interfacial shear strength when the simple shear test is used; and how to describe the constitutive relation. The objectives of present research were (1) performing many tests on soil concrete interface with and without mudcake at the contact (2) investigating the effect of mudcake with the soil concrete interface (3) describing the constitutive relation such as stress-displacement relationship, shear strength, dilatancy relationship. This research will contribute in inclusive understanding of the constitutive relation of mudcake between concrete and sandy clay and also to show the effect of bentonite on the interfacial shear strength.

2. Experimental tests

2.1 Simple Shear Apparatus

Figure (1) shows an image of interface simple shear apparatus used in this study, which is originally manufactured for Geohohai institute. The simple shear apparatus was adapted and used to test the interface between sandy clay and concrete under constant normal load. Adapting of apparatus implied using GDS “pressure volume controller” to apply controlled shear force. Proving ring based dial gauge was used to measure the applied shear force.

Box containers with inner size 107×107 mm were made from iron and filled by concrete mortar. The contact area between clay and concrete does not change because the concrete area is greater than contact area of the clay sample even when sliding displacement occurs. Stack of rings made from copper with diameter of 60 mm represents the container of sample. Minimizing the friction induced between rings implies lubricating them to make deformation of a clay mass occur freely. The height of sample was 10 mm. Normal displacement is measured by strain gauge with accuracy 0.001 mm/digit, which is the same type used for tangential displacement.

2.2 Computing sliding and deformation displacement

Calculating tangential displacement requires readings of three gauges located at the concrete container, lower and upper ring of container rings (Figure 1). Figure 2 shows schematic diagram for the method of calculation the sliding and deformation displacement after applying the shear force. Sliding displacement equals to subtraction of displacement of bottom ring, which is located in contact with concrete from the displacement of concrete i.e. ($\Delta_s = \Delta_c - \Delta_l$). Subtraction of the sliding displacement from the displacement of the top ring of the sample container equals to the deformation displacement ($\Delta_d = \Delta_l - \Delta_u$). Total displacement is calculated by adding sliding displacement to deformation displacement ($\Delta_t = \Delta_s + \Delta_d$). Thus, in simple shear test, the displacement can be split into two components shear sliding displacement and shear deformation displacement, which increase the ability of understanding the behavior of interface.

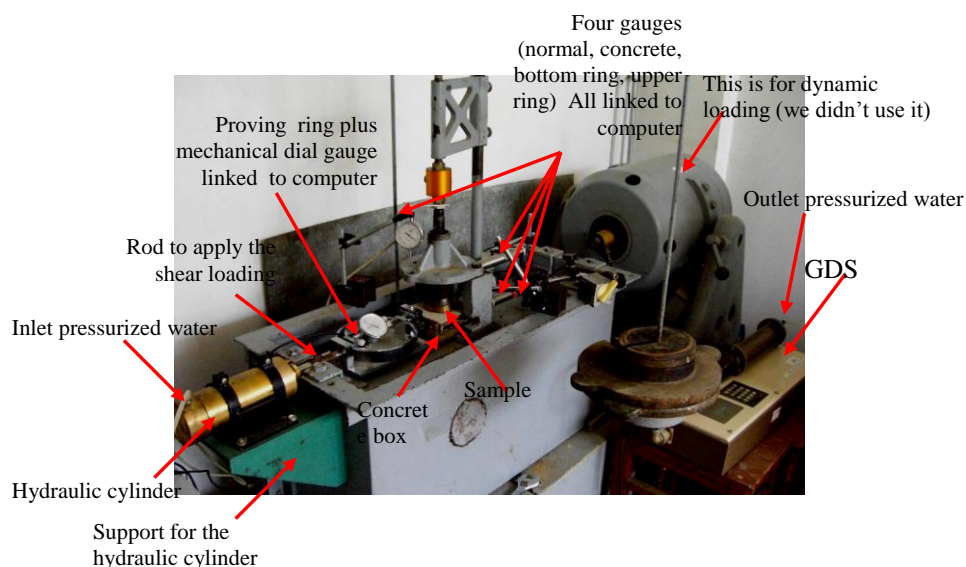


Figure (1). Simple shear apparatus.

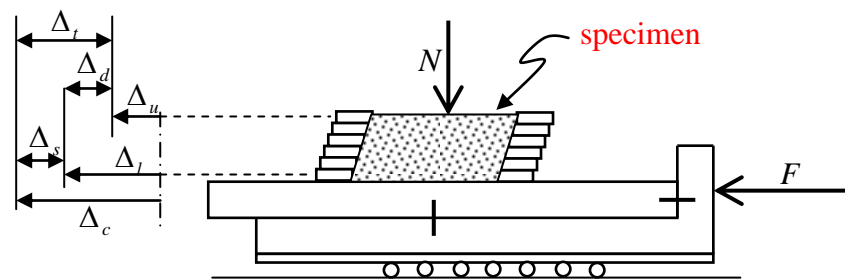


Figure (2). Schematic view shows sliding, deformation, and total shear displacement.

3. Materials and method of test

Preparing of concrete material considered getting practical compression strength and repeatedly testing with minimum wearing in the concrete surface. Five containers were made to pour the concrete mortar. These containers consist of four pieces welded to a plate at the bottom face. The concrete containers minimize the deformation in concrete during performing the test. The concrete was prepared by mixing the sand and cement with 60% water cement ratio, then the five containers were filled by the concrete mortar. The ratio of cement to sand was (1:2.5), and compressive strength is 23 MPa. Scratch was used to fill the concrete mortar into concrete containers and spatula was used to end the surface. Using the five containers of concrete in the interface testing program requires embedding them under wet sand for more than twenty-eight days. Concrete specimens are as follow: the first one is smooth and the other types are rough surface.

The experimental study considered sandy clay soil, which is prepared mixing clay and sand. The dry density of clay is 1.65 g/cm^3 and the optimum water content is about 18%.

For the sand, the dry density is 1.9 g/cm^3 and the optimum water content is about 12%. Table 1 shows the properties of sand such as the diameter opposite to 10%, 30% and 60% finer (D_{10} , D_{30} , D_{60}) as well as the coefficient of uniformity (C_u) and coefficient of curvature (C_c). Sandy clay soil was made by artificially mixing 75% of sand and 25% clay. The sample was prepared by compacting soil inside container of rings with constant dry density.

Preparing of bentonite slurry needs mixing small quantity of bentonite powder with water and waiting for four hours for hydration. The testing needs placing a thin layer of bentonite slurry on the sample by spatula then placing the sample on the concrete for five minutes. Last step is to apply constant normal loading and shear force.

Table (1a). Sand soil properties.

L.L. (%)	P.L. (%)	PL.I. (%)	Gs (%)	Dry Density (g/cm ³)	Wc (%)
35.08	19.98	15.10	2.68	1.65	18

Table (1b). Sand soil properties.

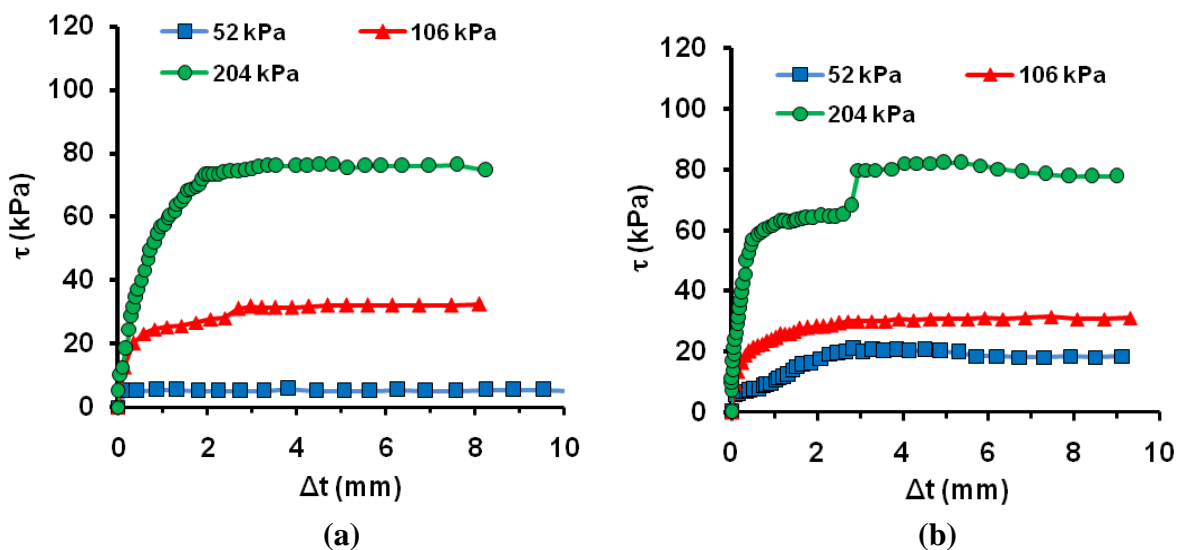
Soil Unified Classification	D_{10}	D_{30}	D_{60}	$C_u = D_{60}/D_{10}$	$C_c = D_{30}^2/(D_{60} \cdot D_{10})$
SP	0.16	0.3	0.45	2.8	1.25

4. Results

4.1 Stress-displacement results

The research considers testing of the interface between sandy clay and concrete with and without bentonite mudcake at contact. One concrete specimen has smooth surface and four concrete specimens have rough surfaces were used in order to take the average. Because of the lake of space, some results are selected. The paper presents the results of interface between sandy clay and two types of concrete; smooth and rough with/without bentonite slurry at the contact.

Figure (3 a,b) shows the result of applied shear stress (τ) versus total displacement (Δt). The test was performed between sandy clay with smooth and rough surface concrete but without bentonite slurry at contact. The shape of curves are hyperpolic and they show the same shape even when the interface tested with smooth and rough-surface concrete. The same comment is recorded for the case when bentonite slurry is used Figure (3c,d). It is also noticed that normal stress has no effect on the shape of curves, however on the size it has. Generally, as the test conducted under high normal stress, shear strength increased noticeably.



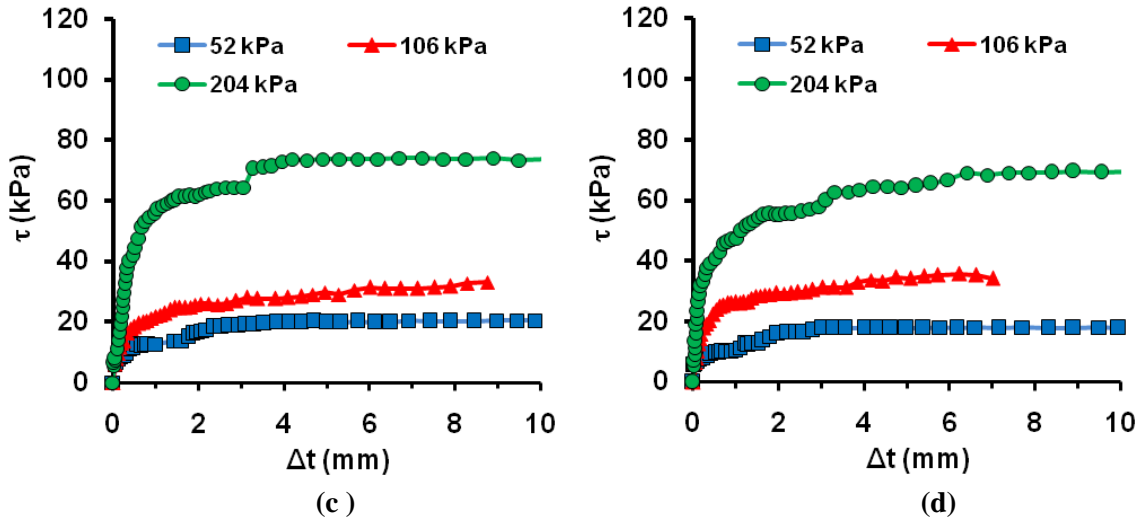
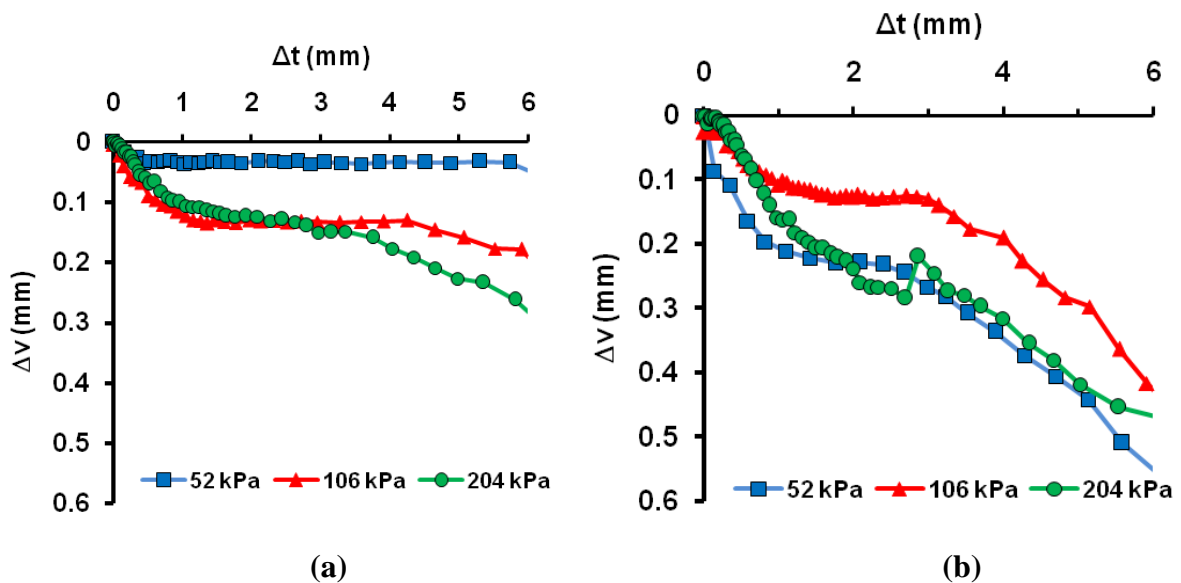


Figure (3). Relation of applied shear stress (τ) versus total displacement (Δt). (a: Sandy clay soil-smooth surface concrete) (b: Sandy clay soil-rough surface concrete; c: Sandy clay soil-smooth surface concrete with bentonite (mudcake) at contact; d: Sandy clay soil-rough surface concrete with bentonite (mudcake) at contact).

4.2 Vertical -shear displacement relations

Figure (4) shows the relation between total shear displacement Δt (mm) versus vertical displacement Δv (mm). Figures (4a) and 4b show the relation for the case of interface between sandy clay soil and smooth concrete and also between sandy clay soil and rough concrete without bentonite mudcake at contact. Figures (4) c and 4d show the same relation but with bentonite at the contact surface. Generally, it can be noticed that as normal stress increases vertical displacement increases Figure (4,a, c and d), however sometimes the results are scattering Figure (4b). Vertical displacement is just compression; there is no transition from compression to tension. Using of bentonite may increase the vertical displacement as will be discussed in sec. 4.2 Figure (4 c, d).



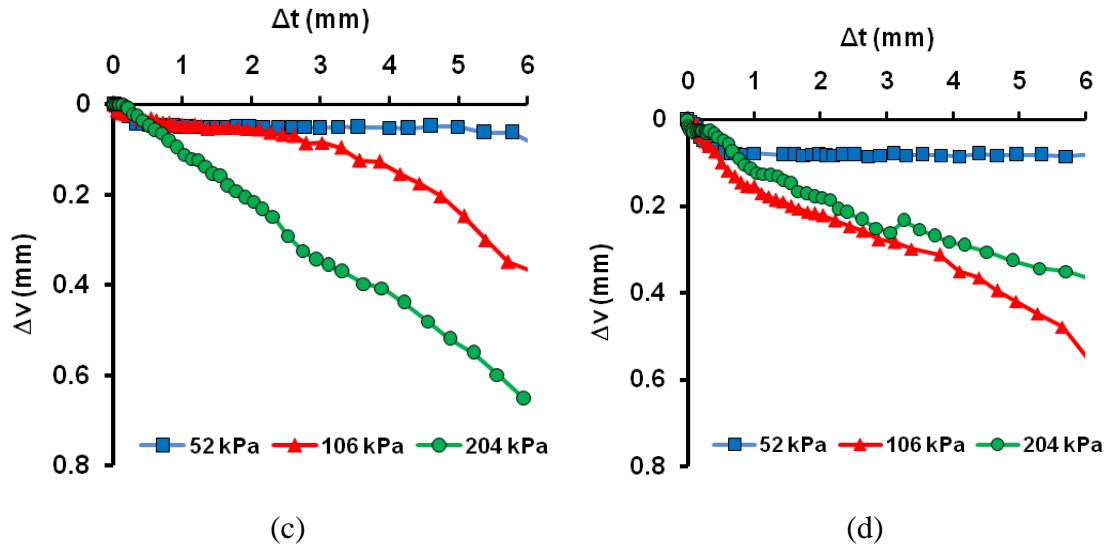
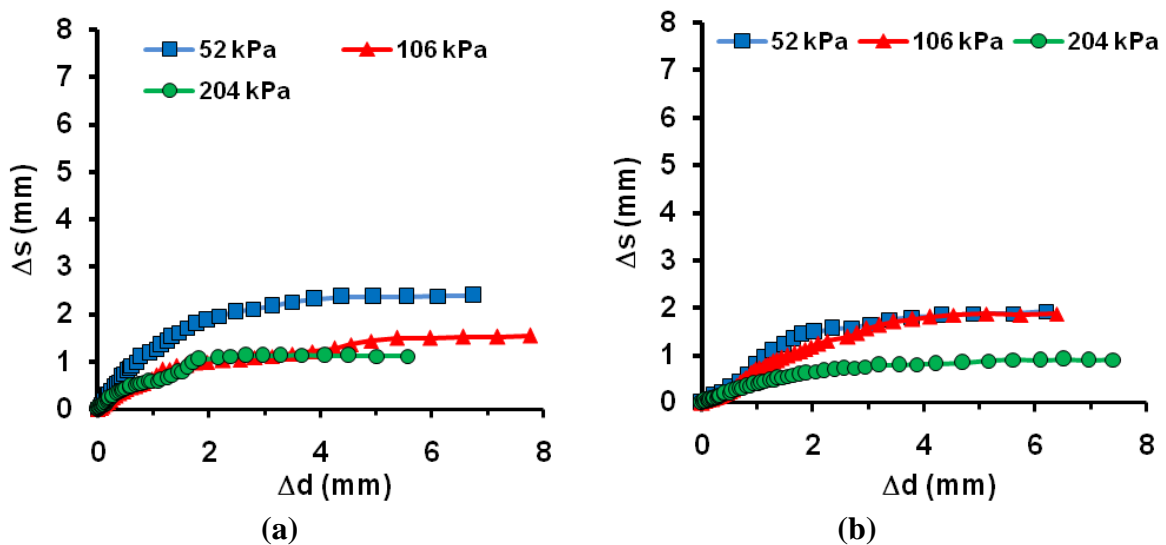


Figure (4). Relation of vertical displacement (Δv) versus total displacement (Δt). (a: Sandy clay soil-smooth surface concrete) (b: Sandy clay soil-rough surface concrete; c: Sandy clay soil-smooth surface concrete with bentonite (mudcake) at contact; d: Sandy clay soil-rough surface concrete with bentonite (mudcake) at contact).

4.3 Sliding-deformation results

Relations between deformation displacement and sliding displacement are shown in Figure (5). Figure (5a) shows the result for the case of sandy clay and smooth concrete. At low normal stress 52 kPa the substantial displacement is the sliding displacement, while for normal stress 106 kPa, 204 kPa the deformation displacement is the substantial. Generally, the deformation displacement is the substantial one Figure (5b, c, d). Effect depicted in figures depends on normal stress intensity.



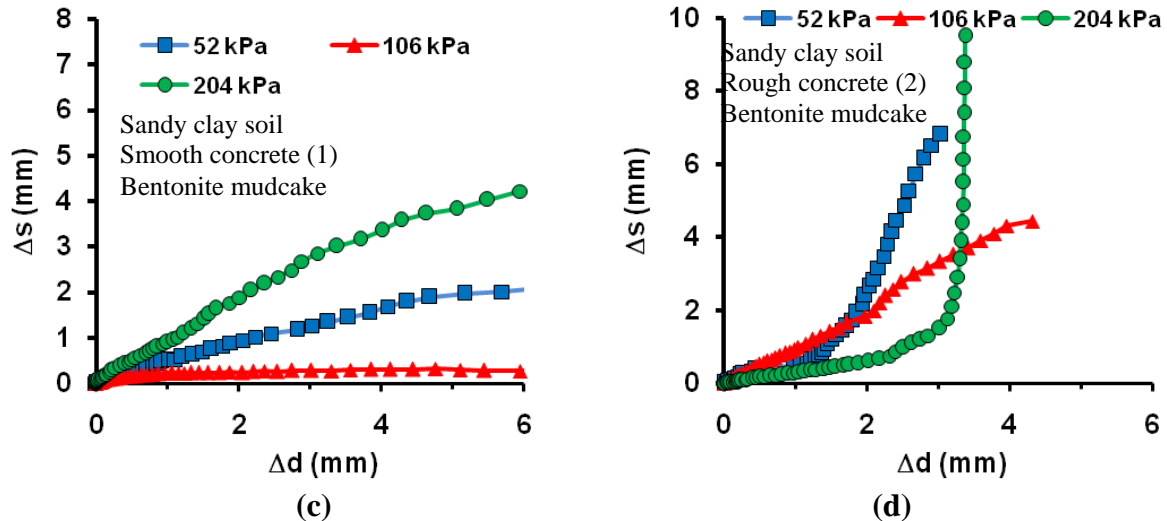


Figure (5). Relation of deformation displacement (Δd) versus sliding displacement (Δs).
 (a: Sandy clay soil-smooth surface concrete) (b: Sandy clay soil-rough surface concrete; c: Sandy clay soil-smooth surface concrete with bentonite (mudcake) at contact; d: Sandy clay soil-rough surface concrete with bentonite (mudcake) at contact).

5- Discussion

The main goal of the present research is to explain the effect of bentonite mudcake on the different relations such as shear stress-shear displacement relations, vertical displacement-shear displacement relations and shear strength relations.

5.1 Shear strength relations

The stress-displacement relations do not show clear peak point Figure (3). Peak point almost appear when the test is carried out on dense sand interfaced with rough surface, see for instance the results of tests conducted between dense sand and steel plate and also between dense sand and concrete [12]. It customarily occurs when applied stresses change sample volume from compression to expansion. Maximum shear stress was mapped against normal stress in order to establish the strength line. Table (2) shows the parameters of adhesion and angle of friction (C , δ) that were obtained from linear curve fitting of the strength line between maximum shear stress and normal stress. The first row in Table (2) represents the parameters for the interface between sandy clay and five types of concrete without bentonite at contact and row two shows the parameters (C , δ) for the case of interface between sandy clay and concrete with bentonite mudcake at contact. The average values for adhesion and angle of friction are shown also in Table (2). Results in Table (2) showed that bentonite decreases the adhesion from 12.9 kPa to 0.4 kPa and in contrast increases angle of friction from 13 to 20.2.

Table (2). Angle of friction and adhesion for sandy clay-concrete interface and Sandy clay-concrete-bentonite-interface.

	Smooth(1)		Rough(2)		Rough(3)		Rough(4)		Rough(5)			
Parameters	C	δ	C	δ	C	δ	C	δ	C	δ	C^{av}	δ^{av}
Sandy clay-concrete-Interface	4.5	14.2°	14.1	13.1°	15.0	13.0°	16.6	13.4°	14.1	11.5°	12.9	13.0°
Sandy clay-bentonite-concrete-Interface	0.0	19.8°	0.0	19.1°	0.0	20.9°	1.8	20.6°	0.0	20.7°	0.4	20.2°

The strength relation is represented by the following equation:

$$\tau = c + \sigma_n \tan \delta \quad (1)$$

τ_{max} symbolizes the equation of ultimate strength, c is the adhesion, δ is the angle of friction.

Average of parameters Table(2) were used in Eq. 1 to calculate the average maximum shear strength for three normal stresses (52, 106, and 204 kPa), The average strength for the case of interface between sandy clay and concrete without bentonite is $\tau^{av}=122$ kPa and for that with bentonite mudcake at contact is $\tau^{av}=134$. The increase in strength is about 10%. At low normal stress the effect of adhesion (c) is sensible, however as normal stress increases the adhesion has an insensible effect compared to the effect of angle of friction. For instance, at normal stress 52 kPa, applying equation 1 on the two average parameters (C^{av} , δ^{av}) Table (2), gives $\tau = 25$ kPa for test without bentonite and $\tau = 20$ kPa for test with bentonite. It can be seen that using bentonite decreases the strength about 20% at normal stress 52 kPa. At normal stress 204 kPa, $\tau = 60$ kPa for test without bentonite and $\tau = 75$ kPa for test with bentonite. Here using bentonite increases the strength about 25% at normal stress 204 kPa. At normal stress 106 kPa the increase is about 5%. Taking the average for the increase and decrease in strength, result of averaging show using bentonite increase the strength by 10%.

5.2 Vertical displacement-shear displacement- relations

Generally, the vertical displacement (Δv) increases as bentonite is used. At smooth surface there is no increase Table (3), Δv equals to 0.6 mm. Average value (Δv^{av})for the test without bentonite was 0.47 mm while it increases to 0.55 mm for the test with bentonite mudcake (Figure 6a,b). Vertical displacement increases by 17%, however the increase in vertical displacement for bentonite layer is not the same and can be determined through this section. Vertical strain equals to vertical displacement divided the original height of the soil sample $\varepsilon_v = \Delta v/h$, which is equal to 0.047. When we use bentonite layer of 1.5 mm, the thickness of soil sample will be 8.5mm (Figure 6 c,d). The vertical displacement in the soil

sample will be $\Delta v_{8.5mm} = 8.5 \times \varepsilon_v$ which is equal to 0.400 mm. Therefore, the vertical displacement in the bentonite layer will be equal to $0.55 - 0.4 = 0.15$ mm where 0.55 mm is the vertical displacement in the soil sample plus bentonite layer. Vertical strain in bentonite is equal to $0.15/1.5$ which is equal to 0.1. Strain in bentonite equal to $0.1/0.045 = 2.2$ times the strain in sandy clay sample. Thus we can conclude that compressibility of bentonite layer is greater two times than the compressibility of sandy clay.

Table (3). Average maximum vertical displacement.

Concrete Shape	Δv (mm), (1)	Δv (mm), (2)	Δv (mm), (3)	Δv (mm), (4)	Δv (mm), (5)	Δv^{av} (mm)
Sandy clay-concrete	0.6	0.49	0.45	0.25	0.58	0.47
Sandy clay-bentonite-concrete	0.6	0.76	0.51	0.24	0.62	0.55

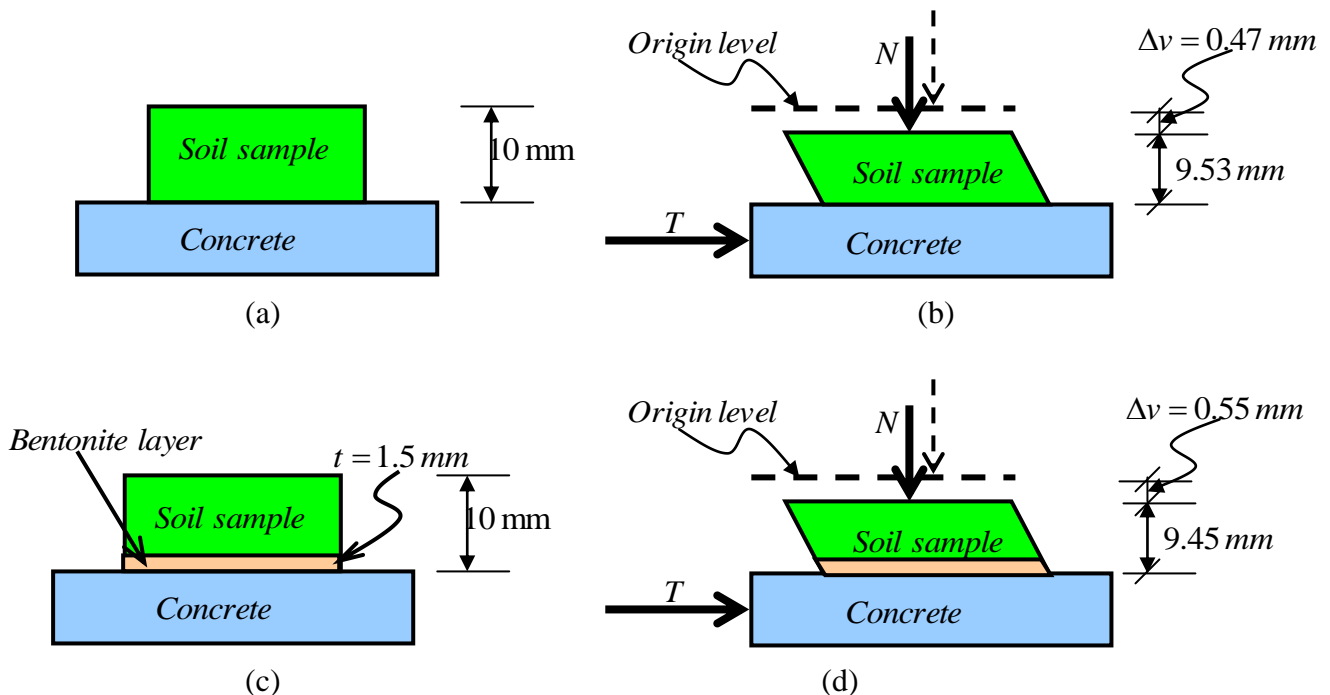


Figure (6). Schematic view show the vertical displacement for test with/without bentonite, before/after the test.

5.3 Sliding –deformation relations

Sliding of the sample depends on two parameters the adhesion and the friction. Using the relations between sliding displacement and deformation displacement (Figure 5) can show that the maximum value of sliding is different as concrete surface and normal stress are changed. We suggested the following equation to calculate sliding ratio $R_s = \Delta_s / \Delta_t$. Table 4 shows the average of sliding ratio. Using of bentonite increases the sliding ratio from 0.25 to 0.36. Figure (7) shows schematic view for the sliding for the test with and without bentonite.

Using of bentonite increases the sliding by percentage of 44%. Increasing of sliding refers to weakness in the contact between soil and concrete, however it is worthless to say that it will reduce the strength. The resistance then will be moved to the body of sample. If the sliding ratio less than 0.5 that means sliding failure was indicated. Most surly the parameters of adhesion and friction are different at each point in the sample body, however it is impossible now to calculate the parameters at each point. With the aid of sliding ratio we can indicate how much shear stresses cause sliding and deformation. We can get the adhesion and angle of friction at sliding by multiplying the total adhesion and angle of friction by the sliding ratio.

Table (4). Sliding ratio for sandy clay-concrete interface and sandy clay-bentonite-concrete-interface.

Concrete Shape	R_s (1)	R_s (2)	R_s (3)	R_s (4)	R_s (5)	R_s
Sandy clay-concrete	0.19	0.38	0.25	0.17	0.27	0.25
Sandy clay-bentonite-concrete	0.24	0.65	0.35	0.17	0.38	0.36

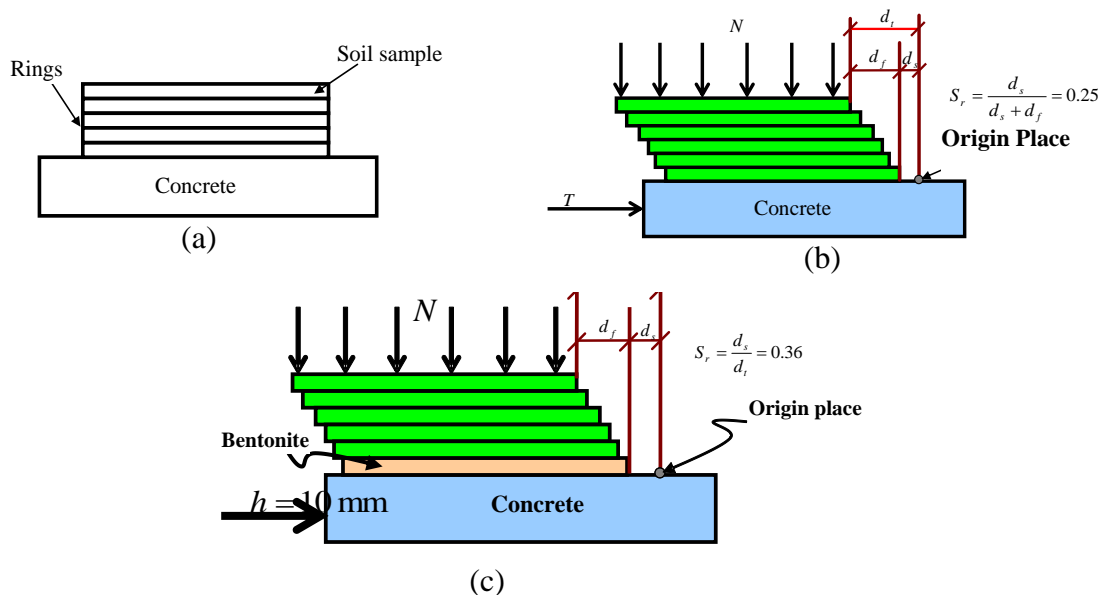


Figure (7). (a) schematic view show the sample rings and concrete before performing the test (b) Average sliding ratio after applying normal and shear force for test between sandy clay and concrete without bentonite (c) Average sliding ratio after applying normal and shear force for test between sandy clay and concrete without bentonite.

Bentonite has dual effect on the interface. It represents the interface layer and the place of stress concentration. The upper face of bentonite contact with sandy clay which may work as an enhancement material. The bentonite fill the voids between particles of sandy clay

sample at contact. The lower face of bentonite contacts with concrete, which may decrease the interlocking between bentonite and concrete. Because the layer of bentonite is weak, it may reduce the strength to sliding. Therefore, we can say that sliding increased from 0.25 for the test without bentonite to 0.36 for the test with bentonite at contact. The increase in sliding is about 44%. Increase in sliding means the body of sample undergo little applied force at first, but after increasing of the applied force, sliding increases, bentonite mudcake fills the voids between asperities of concrete surface making a high resistance against applied shear stress Figure (8), the body of sample begun to undergoes the load and deformation increases until failure. Therefore the shear strength increases as normal stress increase since bentonite will improve the sandy clay soil at the contact between sandy clay and bentonite and also makes the bentonite slurry fill the voids between asperities of concrete.

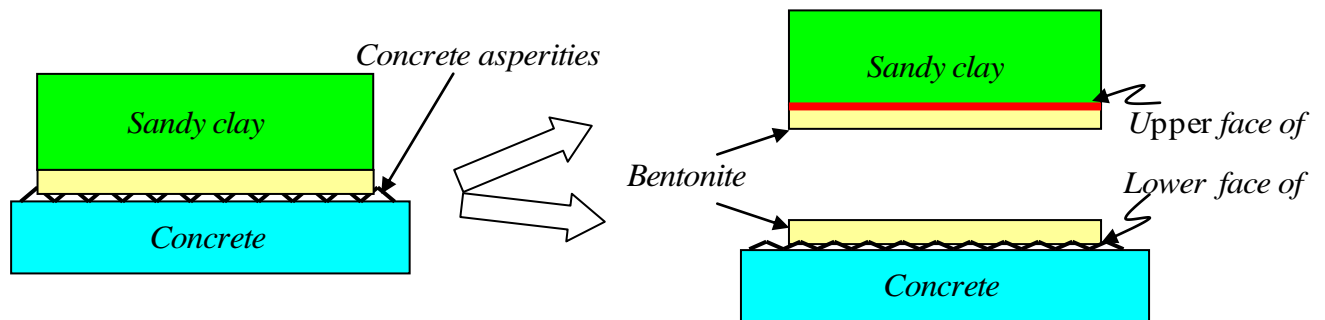


Figure (8). (a) schematic view show the dual effect of bentonite mudcake.

6. Conclusions

In this research simple shear test was used to investigate the effect of bentonite mudcake between sandy clay and concrete and described the relations of shear stress-displacement, vertical displacement-shear displacement relations. Laboratory tests were conducted on interface between sandy clay soil and five specimens of concrete, one has smooth surface and four have different rough surfaces. Tests were conducted with and without bentonite at contact of sandy clay and concrete. The paper presented the following findings. (1) The bentonite mudcake increased the strength by 10% since it fills the voids between soil particles trying to enhance the soil at contact. (2) Using bentonite indicated an increase in vertical displacement by 17% when testing conducted with bentonite at contact more than that without bentonite (3) Using bentonite increased the sliding between sandy clay and concrete by about 44%. (4) bentonite mudcake has dual effect on the interaction between soil and concrete; the upper face of bentonite interacts with sandy clay and the lower face interacts with the

concrete. The contributions increase the understanding of the effect of bentonite mudcake and also describing the constitutive relations of sandy clay-bentonite-concrete-interface .

Acknowledgement

7. References

- [1] O'Neill, M. W. and Reese, L. C. (1999), "Drilled Shafts: Construction Procedures and Design Methods" ADSC: *The International Association of Foundation Drilling*, Publication No. ADSC-TL4, Vol. I.
- [2] Fleming, W.G.K. & Sliwinski, Z.J. (1977), The Use and Influence of Bentonite in Bored Pile Construction, CIRIA REPORT PG3.
- [3] Reese, L.C. & Tucker, K.L. (1985), Bentonite Slurry in Construction Drill Piers. Proc. of a Session sponsored by the Geotechnical Engineering Division of the American Society of Civil Engineers in Conjunction with the ASCE Convention, Denver, Colorado.
- [4] Wardle, I.F., Price, G., & Freeman J., (1992), Effect of Time and Maintained Load on the Ultimate Capacity of Pile in Stiff Clay. Piling European Practice and Worldwide trends. Proc. of the Conf. Organized by the ICE, London.
- [5] Majano E. et al., Effect of Mineral and Polymer Slurries on Perimeter Load Transfer in Drill Shafts, A Report to ADSC, University of Houston, Jan. 1993.
- [6] Thasnanipan, N., Baskaran G. & Anwar, M.A. (1998), Effect of Construction Time and Bentonite Viscosity on Shaft Capacity of Bored Piles, Proc. of the 3rd Int. Geotechnical Seminar on Deep Foundations on Bored and Auger Piles, Ghent, Belgium.
- [7] Brown, D., Muchard, M., and Khouri, B., (2002), "The Effect of Drilling Fluid on Axial Capacity", Cape Fear River, NC, Proceedings of the 27th Annual Conference on Deep Foundations, 2002, San Diego, CA "The Time Factor in Design and Construction of Deep Foundations", (DFI).
- [8] Xue F. Gu, Seidel, J. P., Haberfield, C. M., and Bouazza, A., (2005), "Wear of Sandstone Surfaces During Direct Shear Testing of Sandstone/Concrete Joints" Advances in Deep Foundations (GSP 132) Part of Geo-Frontiers 2005 Proceedings of the Sessions of the Geo-Frontiers 2005 Congress C. Vipulanandan, F. C. Townsend, Editors Austin, Texas, USA, January 24–26, 2005.
- [9] Reddy, E. S., Chapman, D. N. and Sastry, V., (2000), "Direct shear interface test for shaft capacity of piles in sand." *Geotech. Test. J.*, 23(2), 199-205.
- [10] Ressel R. Shakir and Zhu Jungao. (2009) "Behavior of compacted clay concrete interface" *Frontiers of Architecture and Civil Engineering in China* 3(1) 2009.

- [11] Ressel R. Shakir and Zhu Jungao (2009) "Mechanical Behavior of Soil and Concrete Interface" ICEM 2008: International Conference on Experimental Mechanics 2008, edited by Xiaoyuan He, Huimin Xie, Yilan Kang, Proc. of SPIE Vol. 7375, 73756R · © 2009 SPIE.
- [12] Uesugi, M., Kishida, H., and Uchikawa, Y., (1990). "Friction between dry sand and concrete under monotonic and repeated loading," Soils and Foundations, 30(1),115-128.

8. Notations

List of symbols

Δ_s = *sliding displacement*

Δ_c = *concrete displacement*

Δ_l = *lower ring displacement*

Δ_u = *upper ring displacement*

Δ_t = *total displacement*

Δ_d = *deformation displacement*

The Effect of Thermal Residual Stresses Analysis on Tetrahedral Elements Surface Structure

Kadhim Karim Mohsen

Mechanical Engineering Department

College of Engineering

Thi-Qar University

Abstract

This study investigates the effect of thermal residual stress analysis on tetrahedral elements surface structure using finite element technique. An understanding of the effects related to the thermal residual stress is necessary to improve the ability of designers to precisely predict the catastrophic behavior of the apparatuses during overhaul. Tetrahedral elements surface structure production component subjected to applied loads needs to optimize this component that is critical to the tetrahedral elements surface structure efficiency. The applied loads and resulting residual stresses under service conditions is demanded. The finite element modeling was performed. In addition, the fracture life prediction was carried out using finite element based on fatigue analysis. It was observed that the fracture was significantly influenced due to the residual stresses. The obtained result indicates that the existence residual stresses produce the shortest fatigue life for applied loads conditions. The process is one of the promising surface treatments to increase the fracture life for tetrahedral elements surface structure.

Keywords: Tetrahedral elements surface; residual Stresses; fatigue, finite element method, optimization design.

تأثير تحليل الاجهادات المتبقية الحرارية على هيكل رباعي السطوح

المستخلص

تهدف هذه الدراسة الى بحث تأثير الاجهادات المتبقية الحرارية على هيكل رباعي السطوح باستخدام طريقة العناصر المحددة حيث ان من الضروري معرفة التأثيرات الحرارية التي لها علاقة بالاجهادات المتبقية لتحسين قدرة المصممين للتنبأ بدقة سلوك المنتج للفشل اثناء الخدمة . ان الهيكل رباعي السطوح المعرض الى احمال حرارية مسلطة عليه يحتاج الى تصميم امثل لزيادة كفاءة الهيكل حيث تتطلب الاحمال المسلطة والاجهادات المتبقية اثناء ظروف الخدمة اضافة الى انه تم بناء انموذج رياضي للتنبأ بعمر الكسر باستخدام طريقة العناصر المحددة معتمدة على تحليل الكسر وباعتماد على نتائج

طريقة العناصر المحددة تبين ان عمر الكسر يتأثر بصورة كبيرة بالاجهادات المتبقية حيث النتائج اعطت مؤشرا على ان الاجهادات المتبقية تؤدي الى عمر اقصر للهيكل لجميع ظروف العمل وان هذه العملية هي واحدة من المعالجات لعمر الكلال لوصلات هيكل رباعي السطوح.

كلمات مرشدة: رباعي السطوح، الاجهادات المتبقية، الكلال، طريقة العناصر المحددة، التصميم الامثل.

1. Introduction

The use of linear tetrahedral elements facilitates the exact analytical integration of the finite element arrays, and therefore the exact evaluation of the discrete balance equation. Further, the discontinuous integration procedure let us evaluate correctly the discontinuous nature of phase-change phenomena.

The highly non-linear equation governing the problem is solved using the Newton-Raphson method, with an exact, analytically computed tangent matrix. Such an iterative method provides probably the fastest way to solve this equation. Convergence starting from initial solutions lying out of the "attraction" zone was enforced using a line-search procedure. Therefore, it yields an improvement of the robustness of Newton-Raphson method. Thermal results were correctly validated against an analytical solution for a non-is other malphase change problem [1].

The interaction between electricity and elasticity were analyzed using tetrahedral elements. However, these elements were too thick for thin shell or plate applications. To overcome this drawback, Tzou and Tseng (1990) proposed a "thin" piezoelectric solid element by adding three internal degrees of freedom for the vibration control of structures with piezoelectric materials. Hwang et al. (1993) employed classical laminated plate theory (CLPT) to analyze the vibration control of a laminated plate with piezoelectric sensors and actuators. Their study explored the optimal design of the piezoelectric sensors and actuators. Based on the first-order shear deformation theory, Chandrashekhare and Tenneti (1995) developed a finite element model for the vibration control of laminated plates with piezoelectric sensors and actuators and analyzed the thermally induced vibration suppression of laminated plates. Robbins and Reddy (1991) presented the finite element model of a piezoelectrically actuated beam by using four deferent displacement-based one-dimensional beam theories all of which can be reduced from the generalized laminated plate theory of Reddy (1987) [2].

Previous tetrahedral schemes based on generalizations of box splines have encoded arbitrary directional preferences in their associated subdivision rules that were not reflected in

tetrahedral base mesh. Our method avoids this choice of preferred directions resulting a scheme that is simple to implement via repeated smoothing. In an extended appendix, we analyze this tetrahedral scheme and prove that the scheme generates C2 deformations everywhere except along edges of the tetrahedral base mesh. Along edges shared by four or more tetrahedra in the base mesh, we present strong evidence that the scheme generates C1 deformations [3].

The high residual compressive stress of tetrahedral amorphous carbon film deposited by the filtered vacuum arc process causes instability of the coating and substantially limits its applications. The high residual stress is a matter of particular concern for its application to micro electromechanical systems MEMS because the MEMS structure can be severely deformed even when very thin ta-C film is deposited. Systematic control of the residual stress has thus been one of the most important issues in ta-C coating technology. However, a decrease in the residual compressive stress is usually accompanied by the deterioration of the advantageous properties such as high hardness, optical transparency, or surface smoothness [4].

Residual stresses are known to influence a material's mechanical properties such as creep or fatigue life. Sometimes, the effect on properties is beneficial; other times, the effect is very deleterious. Therefore, it is important to be able to monitor and control the residual stresses.

Residual stresses are stresses that remain after the original cause of the stresses (external forces, heat gradient) has been removed. They remain along a cross section of the component, even without the external cause. Residual stresses occur for a variety of reasons, including inelastic deformations and heat treatment. Heat from welding may cause localized expansion, which is taken up during welding by either the molten metal or the placement of parts being welded. When the finished weldment cools, some areas cool and contract more than others, leaving residual stresses. Another example occurs during semiconductor fabrication and micro system fabrication when thin film materials with different thermal and crystalline properties are deposited sequentially under different process conditions. The stress variation through a stack of thin film materials can be very complex and can vary between compressive and tensile stresses from layer to layer.

Induction surface hardening creates a very desirable thermal residual stress state at the surface and thermal residual stress distribution below the surface. Residual stresses are always of a compressive nature and are usually present to the depth of the induction surface hardened layer. A major difficulty in induction surface hardening is, however, to ensure a very slight

variation in hardness and the existence of compressive residual stresses in transition areas to the hardness of the base material. By gently varying the hardness and through compressive residual stresses in the transition area, it is possible to diminish the notch effect induced by stress concentration in parts loaded by cyclic tensile stresses. Additional grinding of the induction surface hardened surface has an adverse effect on the stress state in the surface layer, since grinding always induces tensile residual stresses. By correct selection of the machining conditions and the grinding wheel, taking into account its properties, the engineer will contribute to lessening the relative grinding tensile thermal residual stress distributions which will help keep the favourable thermal residual stress state after induction surface hardening [2].

The residual stresses near the weld root and the weld toe for multi-pass welded tube-to-plates. Two different tubular joint configurations were studied; a three-pass single-U weld groove for maximum weld penetration and a two-pass fillet (no groove) welded tube-to-plates for minimum weld penetration. A 2D axi-symmetric finite element model was developed to calculate the distribution, HAZ, penetration depth and the thermal residual stress distribution for the sequentially coupled thermo-mechanical analysis. The calculated residual stresses was compared with experimental results and showed qualitatively good agreement. Torsion fatigue tests were performed in order to study crack propagation from the weld root, lower and upper weld toe in mode III. Some of the tube structures were loaded with a static internal pressure in order to separate the root crack and initiate the crack growth in mode III. Another batch was PWHT and fatigue tested, in order to study the influence of residual stresses [3].

Established methods for calculating residual stresses from the strains measured when using the slitting method give results for the stresses that exist within the depth range of the slit. Practical considerations typically limit this range to about 90-95% of the specimen thickness. Force and moment equilibrium can provide additional information that may be used to estimate the residual stresses in the “no-data” region within the remaining ligament beyond the maximum slit depth. Three different numerical methods to calculate the thermal residual stress profile over the entire specimen thickness are investigated. They are: truncated Legendre series, regularized Legendre series, and regularized unit pulses. In tests with simulated strain data and with strain data measured on a cold compressed 7050-T7452 Aluminum hand forging, the three methods gave generally similar stress results in the central region of the specimen. At small depths, where the strain sensitivity to the residual stresses is low, the two regularized calculation methods tended to give more stable results. In the area of

very large depth beyond the maximum depth of the slit, the regularized Legendre series solution generally gave the most realistic stress results [4].

Finite Element Analysis (FEA) has been carried out on a single pass butt welding model to illustrate the distortion and thermal residual stress field developed in the weldment. Thermo-elastic-plastic analysis has been used to find the residual stresses and distortion. It was found that the residual stresses and distortion values increase with of laser beam power. On the other hand, the distortion and residual stresses decrease as the speed increases. There is a reduction of thermal residual stress and distortion values as the spot diameter increases [5].

This study presents a direct analysis ,discrete and composite modeling of tetrahedral elements surface structure in three dimension detail interaction of the long-term behavior differential settlement estimation. The crack initiation and propagation result in tetrahedral elements surface structure and life-cycle prediction High-end detail analysis (crash, fatigue, fracture mechanism) caused by shear in wall.

2. Types of loads

Loads cause stresses, deformations, and displacements in structures. Assessment of their effects is carried out by the methods of structural analysis. Excess load or overloading may cause structural, and hence such possibility should be either considered in the design or strictly controlled.

Mechanical structures, such as aerospace vehicles (e.g. aircraft, satellites, rockets, space stations, etc...), marine craft (e.g. boats, submarines, etc.), and material handling machinery have their own particular structural loads and actions.

Loads can be classified as dead loads, live loads ,environmental loads, and other loads .The dead loads are static forces that are relatively constant for an extended time. They can be in tension or compression. The term can refer to a laboratory test method or to the normal usage of a material or structure.

Live loads are usually unstable or moving loads. These dynamic loads may involve considerations such as impact, momentum, vibration, slosh dynamics of fluids, etc. An impact load is one whose time of application on a material is less than one-third of the natural frequency of vibration of that material.

Cyclic loads on a structure can lead to fatigue damage, cumulative damage, or failure. These loads can be repeated loadings on a structure or can be due to vibration. The Environmental loads are act as a result of weather, topography and other natural phenomena [6].

Equation of equilibrium is given by:

$$\Delta\sigma + F = 0$$

where, $\Delta\sigma$ is the stress variation and F is the body force. Residual stresses are calculated by using the principle of virtual work. In this method, one considers infinitesimal nodes displacements $\{\delta\}$ imposed onto the body. This causes external total virtual work (equal to the total internal virtual work which is defined by stresses $\{\sigma\}$ and strains $\{\varepsilon\}$). By using FEM (finite element model), strain–displacement can be expressed briefly as follows:

$$\{\varepsilon\} = [B]\{\delta\}e$$

where, $\{\varepsilon\}$ is the strain vector, $[B]$ is the strain–displacement interpolation matrix and $\{\delta\}e$ is the displacement vector for an element. The nodal displacement is obtained from

$$\{\delta\} [K]^{-1} (\{R\}_T \{R\}_P)$$

where, $[K]$ is the conductivity matrix, $\{R\}_T, \{R\}_P$ is the resultant nodal displacements vector with respect to nodal temperature and laser beam power.

The stress-strain relationship is defined as follows:

$$\{\sigma\} = [D](\{\varepsilon_e\})$$

where, $[D]$ is the Stiffness matrix and $\{\varepsilon_e\}$ is the elastic strain vector. For the deformation of metals, the Von Mises yield criterion is employed and the elastic strain is given by

$$\varepsilon_e = \varepsilon - \varepsilon_{pl} - \varepsilon_{th}$$

where, ε_e is the elastic strain, ε is the total strain, ε_{pl} is plastic strain and ε_{th} is the thermal strain.

3. Parameters effect on the values of the residual stresses

Influence of some parameters on the residual stresses from quenching concentrates some important effects on the development of residual stresses from quenching: the influence of the martensitic temperature interval and the influence of the shift of the martensite start

temperature caused by thermal stresses. The influence of the location of the maximum quenching rate on the thermal residual stress pattern is also discussed.

A numerical model of the coupled elasto-plastic problem has been developed, which incorporates the influence of the thermal stresses on the martensite start temperature. It is demonstrated that the length of the martensitic temperature interval may have a significant effect on the thermal residual stress pattern. While large martensitic intervals promote compressive residual stresses at the surface, small martensitic intervals give rise to tensile residual stresses even for small thermal gradients at martensitic temperatures.

The shift of the martensite start temperature due to thermal stresses should always be incorporated in calculations because of significant effects on the thermal residual stress pattern. It is also established that during quenching, the thermal stresses always raise the martensite start temperature at the specimen surface, thus promoting non-uniform phase transformation over the cross section of the specimens

Due to the non-uniform temperature distribution during the thermal cycle, incompatible strains lead to thermal stresses. These incompatible strains due to dimensional changes associated with solidification of the weld metal, metallurgical transformations and plastic deformation, are the main sources of residual stresses and distortion [7].

4. Controlled residual stress

Avoid unknown or random thermal residual stress by forbidding quenching of low ductility, light alloy castings into water following high temperature solution treatment. Boiling water is also not permitted since it represents a negligible improvement over cold water. However, polymer quenchant or forced air-quench may be acceptable if casting stress is shown to be negligible. Planned thermal residual stress may be beneficial if designed correctly into the quenching process.

Uncontrolled residual stresses are undesirable, some designs rely on them. For example, toughened glass and pre-stressed concrete depend on thermal residual stress to prevent brittle failure. A demonstration of the effect is shown by Prince Rupert's Drop, where a molten glass globule is quenched to produce a toughened outer layer [8].

Allthermo-mechanical manufacturing processes—such as forging, extrusion, casting, heat treatment, welding, coating, and machining—create residual stresses in industrial products. There are situations when such stresses can be beneficial and are intentionally created, for example, compressive stresses on the outer surface of a component subjected to fatigue loads, autofrettage in gun barrels, and prestressed pressure vessels; even bolted connections and prestressed concrete can be included in this category. In many other situations, however, the presence of thermal residual stress is detrimental to the integrity of the product under service conditions. Examples in this category include: tensile stresses on the outer surface of a component subjected to fatigue loads, tensile stresses on the inner surface of an austenitic stainless steel pipe caused by welding leading to intergranular stress-corrosion cracking in boiling water reactors, interlaminar stresses in coatings leading to their spallation, premature yielding or fracture (especially in brittle materials), and part distortion or dimensional instability. The presence of residual stresses in a part is also known to affect its machinability. For these reasons, mechanical and manufacturing engineers have long been interested in understanding the source of such stresses, their control, and relief. In the case of metallic products, the selection of material is generally dictated by functional requirements such as the ability of the product to withstand service loads, resistance to wear or corrosion, and so forth. It is rare that the magnitude and distribution of residual stresses is a matter of primary consideration while selecting the material to manufacture a metallic part. The issue facing the manufacturing engineer is to control the residual stresses in the product once the material (and often the manufacturing process) has already been selected. In the case of a composite or coated product, however, minimization of residual stresses is a prime consideration while selecting the constituent materials. This article primarily deals with metallic products. A logical way to control residual stresses in a product should consist of the following steps: Understanding the fundamental sources of stress generation Identifying the parameters that can cause residual stresses in a particular manufacturing process Understanding the relative significance of each one of these parameters Experimenting with the most significant process parameters until a suitable combination is obtained that results in the desired magnitude and distribution of residual stresses If the residual stresses in the product are still higher than acceptable, the only recourse left is the use of one of the various techniques of stress relief or the inducement of a stress pattern more favorable than the original [9].

There are several techniques that are used to measure the residual stress. They can be classified as destructive and non-destructive methods. Mechanical methods or dissection uses

the release of stress and its associated strain after doing a cut, hole or crack. Nonlinear elastic methods as ultrasonic or magnetic techniques require a reference sample. X-ray diffraction is a non-destructive method which allows the measurement of thermal residual stress in isolated spots spaced distances as small as 100 micrometers. Residual stresses can be sufficient to cause a metal part to suddenly split into two or more pieces after it has been resting on a table or floor without external load being applied. While this is not a common occurrence, experienced people in the metal working industry have witnessed this phenomenon. While there may be additional factors causing this to occur residual stresses explain these occurrences[10].

5. Residual stresses measurement methods

The stress is an extrinsic property, which cannot be directly measured. All the methods adopted to measure the residual stresses need the measurement of some intrinsic property, such as the strain, the load and area, and after the stress can be calculated.

Possible methods of calculation

- Mechanical methods (controlled hole drilling)
- nonlinear methods (ultrasonic and magnetic techniques)
- diffract to metric methods

Thermal residual stresses are primarily due to differential expansion when a metal is heated or cooled. The two factors that control this are thermal treatment (heating or cooling) and restraint. Both the thermal treatment and restraint of the component must be present to generate residual stresses [11].

6. Analysis of residual stresses

Residual stresses are known to influence materials mechanical properties such as creep or fatigue life. Sometimes, the effect on properties is beneficial; other times, the effect is very deleterious. Therefore, it is important to be able to monitor and control the residual stresses.

Two different techniques are commonly used for measuring the residual stresses. The most popular technique is a special type of X-ray diffraction (known as the $\sin^2\psi$ method), which is used to measure the stresses in fine grained crystalline materials. An alternate method, the

hole drilling method, is most often used when the X-ray technique is not appropriate. Each method, along with its advantages and disadvantages, is described in this note.

7. The X-ray diffraction method

The $\sin^2\psi$ method is a sensitive and accurate technique to measure residual stresses in a fine grained, polycrystalline material. As shown in Figure(1), the position of a diffraction peak will shift as the sample is rotated by an angle ψ .

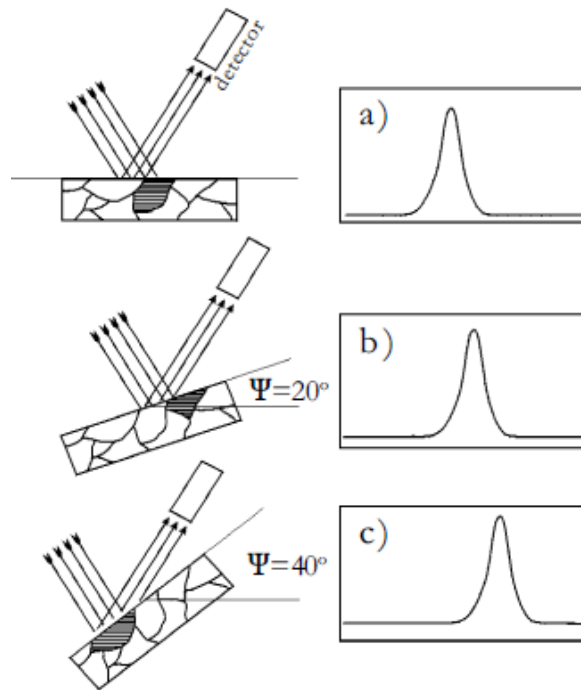


Figure (1). Shift of diffraction peak with change in Q value. Note that as Q increases in b) and c) above, the position of the diffraction peak shifts further and further away from its usual position in a).

The magnitude of the shift will be related to the magnitude of the residual stress. Thus, if there is no residual stress, the shift will be zero. The relationship between the peak shift and the residual stress σ is given by

$$\sigma = \frac{E}{(1 + \nu)\sin^2\psi} \frac{d_n - d_o}{d_o} \quad (13)$$

where E is Young's modulus, ν is Poisson's ratio, ψ is the tilt angle, and d_i are the "d" spacings measured at each tilt angle. If there are no shear strains present in the sample, the "d" spacings would change linearly with $\sin^2\psi$ and a least squares fit to the curve (for multiple values of ψ) would give σ . However, if shear strains are present, a splitting of the plot will occur and the

analysis is more complicated. Finally, if the sample is rotated in-plane, it is possible to determine the principal stresses and their directions.

8. The hole drilling method

There are many situations where X-ray diffraction is not useful for measuring residual stresses. These include non-crystalline materials, large grained materials, nanomaterials, textured, or heavily deformed metals. In these cases, other mechanical methods such as the hole-drilling method are used. The hole-drilling method (ASTM Standard E837) relies on stress relaxation when a hole is drilled into the center of a rosette strain gage such as that shown below. When the material is removed by drilling, the extent of the strain relief is monitored by the gages and the direction and magnitude of the principal stresses can be calculated.



Figure(2). Rosette gage (Magnification: 4x)

A special high speed air turbine drill (shown above) is used to first locate the drill to within 0.001. of the rosette center and then to remove material to a controlled depth. At each depth increment, the strain relief on each of the gages is measured and converted into stress. As subsequent material removals occur, the stress distribution as a function of depth can be estimated. The hole drilling method is used in those situations where the residual stress is relatively uniform over the drilling depth. Thus, it is not intended for situations where the residual stress is superficial.

The accuracy of the hole drilling method is directly related to the ability of locating the hole accurately in the center of the rosette. As an example, if the hole is no more than 0.001. off center, the residual strain error is less than 3%. In practice, the location accuracy is better than this, so the overall accuracy in residual stress measurements is quite good. Another important consideration in this method is the ability to drill the relief hole so as not to

introduce new stresses. This is best achieved in hard materials by use of a high-speed turbine drill which avoids excessive rubbing of the cutting surface against the hole wall. As a result of careful design of the tool, the holes have flat bottoms and straight walls as required by ASTM E837. The hole drilling method has many advantages, but it also has many disadvantages. Of particular concern is that the method is valid only up to about 50% of the yield strength of the test material. Thus, great care has to be exercised when selecting testing methods [12].

The aim of the present study is therefore to propose a further development to facilitate and accelerate geometry acquisition modification during the fabrication of FE models of restorations.

9. Finite element method analysis

Finite element method analysis is a simulation technique which evaluates the behavior of components, equipment and structures for various loading conditions including applied forces, pressures and temperatures. Thus, a complex engineering problem with non-standard shape and geometry can be solved using finite element analysis where a closed form solution is not available. The finite element analysis methods result in the stress distribution, displacements and reaction loads at supports etc. for the model. Finite element analysis techniques can be used for a number of scenarios e.g. Design optimization, material weight minimization, shape optimization, code compliance etc

Most engineering materials have linear stress-strain relationships [12]. These relationships can be expressed for of homogenous material as

$$\sigma = E\epsilon \quad (1)$$

$$\tau = G\gamma \quad (2)$$

These relationships are known as Hooke's Law, where E is the modulus of elasticity, the ϵ are the normal strains, the σ are the normal stresses, G is the modulus of rigidity, the σ_{ij} are the shearing stresses, and the γ are the shearing strains. In order to express the strain components ϵ in terms of the stress components, we use the principle of superposition, which states that the effect of a given combined loading on a structure can be obtained by determining separately.

For general complex isotropic tetrahedral elements surface structure with mass matrix $[m_i]$, stiffness matrix $[k_{ij}]$, damping matrix $[c_i]$, and column matrix of external forces $[p_j]$

Displacement function

$$u_{ij}(x) = c_{ij}\phi_{ij}(x) \quad (3)$$

$$\varepsilon = \frac{\partial u_{ij}(x)}{\partial x} \quad (4)$$

The residual stresses;

$$\tau = \frac{k_{ij}}{A_{ij}}\gamma + \delta_{ij}\varepsilon'_{ij} \quad (5)$$

The Generalized stiffness coefficient is

$$k_{ij} = \int_0^l E_i I_i \phi_{ij}''^2 dx + k_i \phi_i^2 \quad (6)$$

The proportional generalized damping coefficients, damping ratios, damped natural frequencies and damped period the in the i th mode can be obtained from the relation:

$$C_i = \int_0^l C_i \phi_{ij}^2 dx \quad (7)$$

$$C_i = 2\zeta_i m_{ij} \omega_i$$

$$C_{C_{ri}} = 2m_{ij} \omega_i$$

$$\omega_{di} = \sqrt{1 - \zeta_i^2} \quad (8)$$

$$\tau_d = \frac{2\pi}{\omega_{di}}$$

where A_{ij} = cross-sectional area of tetrahedral elements surface structure

$$A_{ij} = b_{ij} t_i$$

b_{ij} = Width of tetrahedral structure elements

t_i = Thickness of tetrahedral structure elements

To find the tetrahedral elements stiffness matrices k_{ij}

$$[K]^{x=1,2,3,\dots} = \begin{bmatrix} k_{11}^x & k_{12}^x & k_{13}^x & k_{14}^x & k_{15}^x & k_{16}^x \\ k_{21}^x & k_{22}^x & k_{23}^x & k_{24}^x & k_{25}^x & k_{26}^x \\ k_{31}^x & k_{32}^x & k_{33}^x & k_{34}^x & k_{35}^x & k_{36}^x \\ k_{41}^x & k_{42}^x & k_{43}^x & k_{44}^x & k_{45}^x & k_{46}^x \\ k_{51}^x & k_{52}^x & k_{53}^x & k_{54}^x & k_{55}^x & k_{56}^x \\ k_{61}^x & k_{62}^x & k_{63}^x & k_{64}^x & k_{65}^x & k_{66}^x \end{bmatrix} \quad (9)$$

For the first 4 trusses tetrahedral elements surface structure stiffeners

$$[K] = \begin{bmatrix} k_{11}^1 & k_{12}^1 & k_{13}^1 & k_{14}^1 & 0 & 0 & 0 & 0 & 0 & 0 & 0 & 0 & 0 & 0 & 0 & 0 \\ k_{21}^1 & k_{22}^1 & k_{23}^1 & k_{24}^1 & & & & & & & & & & & & 0 \\ k_{31}^1 & k_{32}^1 & k_{33}^1 & k_{34}^1 & & & & & & & & & & & & 0 \\ k_{41}^1 & k_{42}^1 & k_{43}^1 & k_{44}^1 & & & & & & & & & & & & \\ & & & & k_{11}^2 & k_{12}^2 & k_{13}^2 & k_{14}^2 & & & & & & & & \\ & & & & k_{21}^2 & k_{22}^2 & k_{23}^2 & k_{24}^2 & & & & & & & & \\ & & & & k_{31}^2 & k_{32}^2 & k_{33}^2 & k_{34}^2 & & & & & & & & \\ & & & & k_{41}^2 & k_{42}^2 & k_{43}^2 & k_{44}^2 & & & & & & & & \\ & & & & & & & & k_{11}^3 & k_{12}^3 & k_{13}^3 & k_{14}^3 & & & & \\ & & & & & & & & k_{21}^3 & k_{22}^3 & k_{23}^3 & k_{24}^3 & & & & \\ & & & & & & & & k_{31}^3 & k_{32}^3 & k_{33}^3 & k_{34}^3 & & & & \\ & & & & & & & & k_{41}^3 & k_{42}^3 & k_{43}^3 & k_{44}^3 & & & & \\ & & & & & & & & & & & & k_{11}^4 & k_{12}^4 & k_{13}^4 & k_{14}^4 \\ & & & & & & & & & & & & k_{21}^4 & k_{22}^4 & k_{23}^4 & k_{24}^4 \\ & & & & & & & & & & & & k_{31}^4 & k_{32}^4 & k_{33}^4 & k_{34}^4 \\ & & & & & & & & & & & & k_{41}^4 & k_{42}^4 & k_{43}^4 & k_{44}^4 \end{bmatrix} \quad \dots \quad (10)$$

using over labia method

$$[K] = K_1 + K_2 + K_3 + K_4 \quad (11)$$

$$C_p \frac{\partial T}{\partial t} = \frac{\partial}{\partial x} \left(\lambda \frac{\partial T}{\partial x} \right) + \frac{\partial}{\partial y} \left(\lambda \frac{\partial T}{\partial y} \right) + Q \quad (13)$$

where C_p is the specific heat of the work, t the element thickness, λ the heat conductivity, the temperature T and Q the generated heat. It is assumed as well that the heat comes only from the boundary and that no heat source exists inside the material.

11. Modeling of problem

The shape function for tetrahedral elements surface structure is assumed to be linear in the finite element in the following form:

$$\phi = c_1 + c_2 x + c_3 x^2 + c_4 x^3 \quad (14)$$

as for the tetrahedral element taken in continuum as shown in Fig. (3), C_1, C_2, C_3 and C_4 are determined by substituting $x_1, x_2, x_3, x_4, y_1, y_2, y_3$, and y_4

Equation (14) can be written as

$$\begin{aligned} \phi = \frac{1}{2S} \{ & \langle y_{43}(x - x_3) - x_{43}(y - y_3) \rangle T_1 + \langle -y_{42}(x - x_4) - x_{42}(y - y_4) \rangle T_2 \\ & + \langle y_{31}(x - x_3) - x_{31}(y - y_3) \rangle T_3 \\ & + \langle y_{21}(x - x_1) - x_{21}(y - y_{12}) \rangle T_4 \} \end{aligned} \quad (15)$$

where T_1, T_2, T_3 and T_4 are the temperature at the nodes and S is the boundary surface of the tetrahedral structure

$$x_{ij} = x_i - x_j \quad \text{and} \quad y_{ij} = y_i - y_j$$

The tetrahedral structure surface region is divided into finite number of element rectangular in shape as shown in Figure(4) connected at their four nodes for plane stress and along inters elements boundaries, equilibrium and compatibility must be satisfied at each node and along the boundaries between the elements.

The general form for the thermal residual stress [14]

$$\sigma_{ij} = - \frac{E \propto \Delta T}{(1 - \nu)} \quad (16)$$

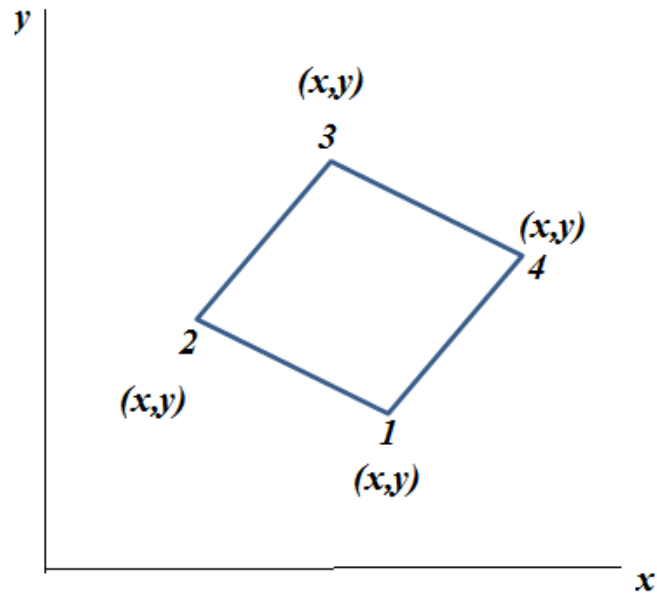
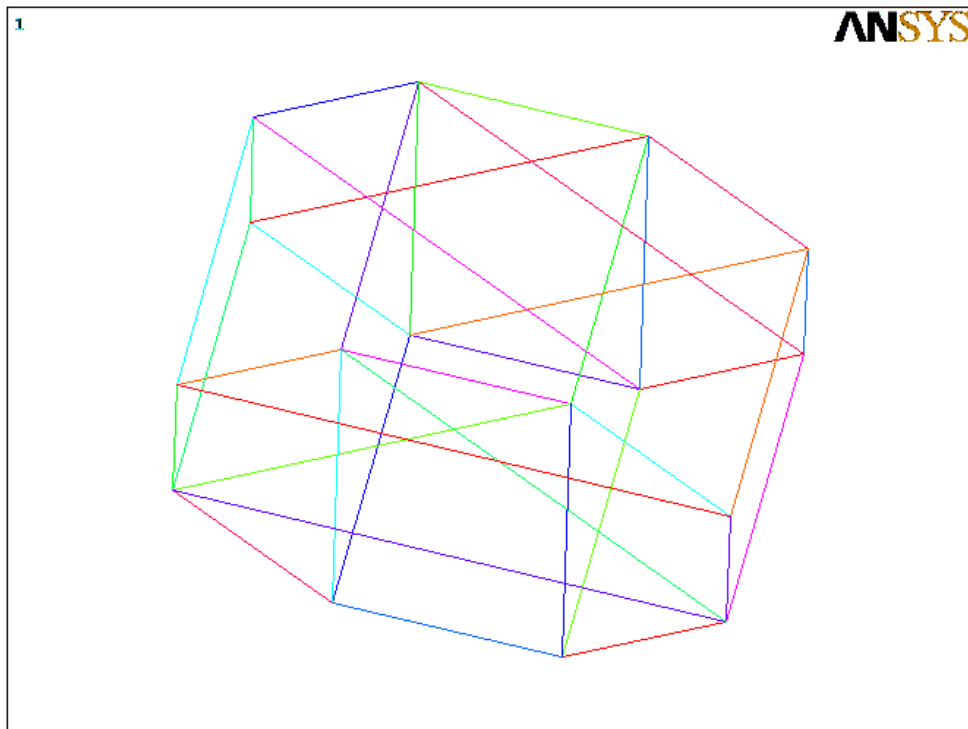


Figure (4).A plane stress of tetrahedral structure surface region divided into finite elements.

Therefore the division of a three-dimensional region into tetrahedral elements of the continuous structure can be shown in Figure(5)



Figure(5). Division of a three-dimensional region into tetrahedral elements .

Fracture life prediction can be obtained from the previous equations as follows:

$$N_f = c/\mu A_{ij} D \sum_{i=1}^n \sum_{j=1}^n k_{ij} F_i \phi \quad (15)$$

12.Results and discussion

For various loading conditions investigated, the thermal residual stress analysis results for the tetrahedral elements surface structure were checked against the allowable stresses. The stress and displacement results were found to be suitable per structural engineering practices.

Thermal residual stress can be determined from the tetrahedral geometry of the structure and the distribution of strains and stresses combination set up during the operating conditions. For temperature changes leading to thermal expansion cause thermal loads then residual stresses are caused by the thermal loading that occurs when hot tetrahedral elements surface structure metal is cooled metal. Successive cooling causes thermal, plastic, and transformation of stresses strains to format the material, and these strains give rise to residual stress.

By using the Ansys program to study the output graphs for present work as follows:

Figure(6) and (7) show the application of equation (16) which explain the relationship between the residual stresses after temperature change where the residual stresses of the heated element is higher than the lower one.

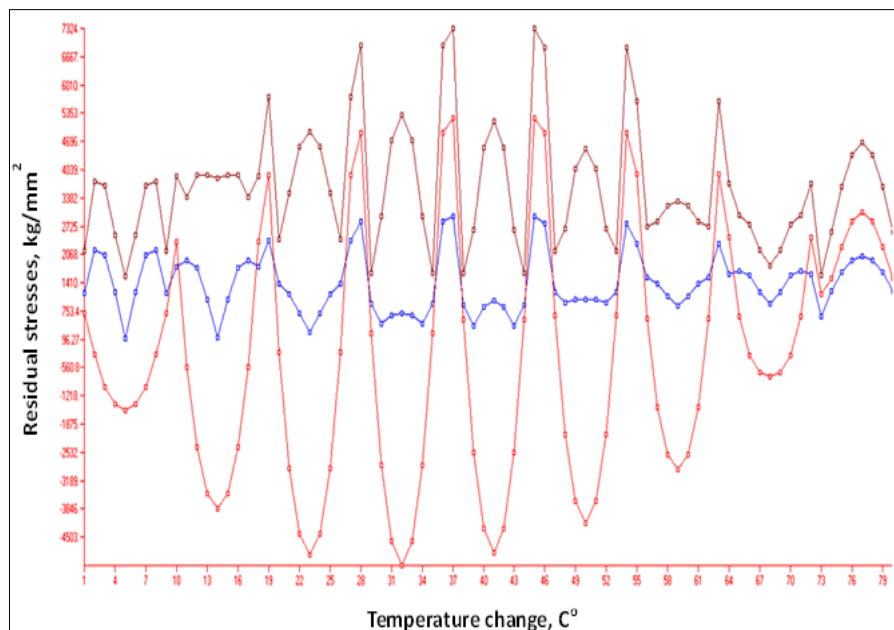
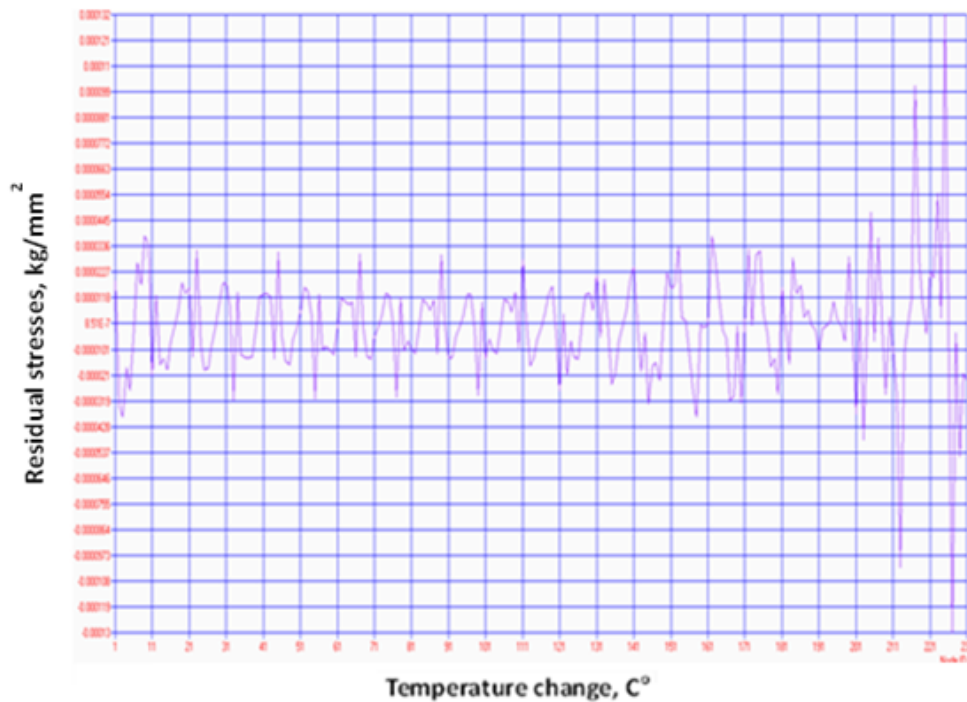
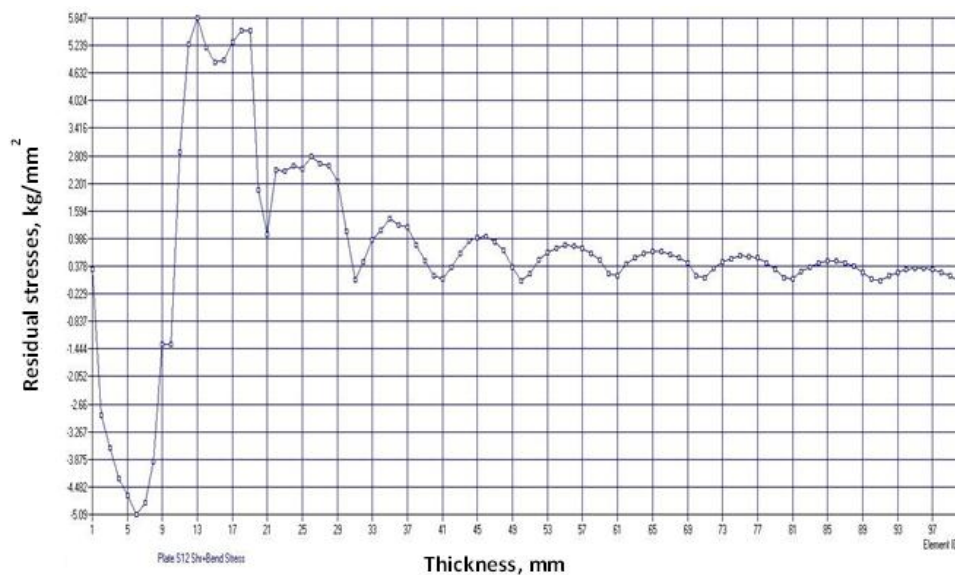


Figure (6). Residual stresses of the tetrahedral structure.



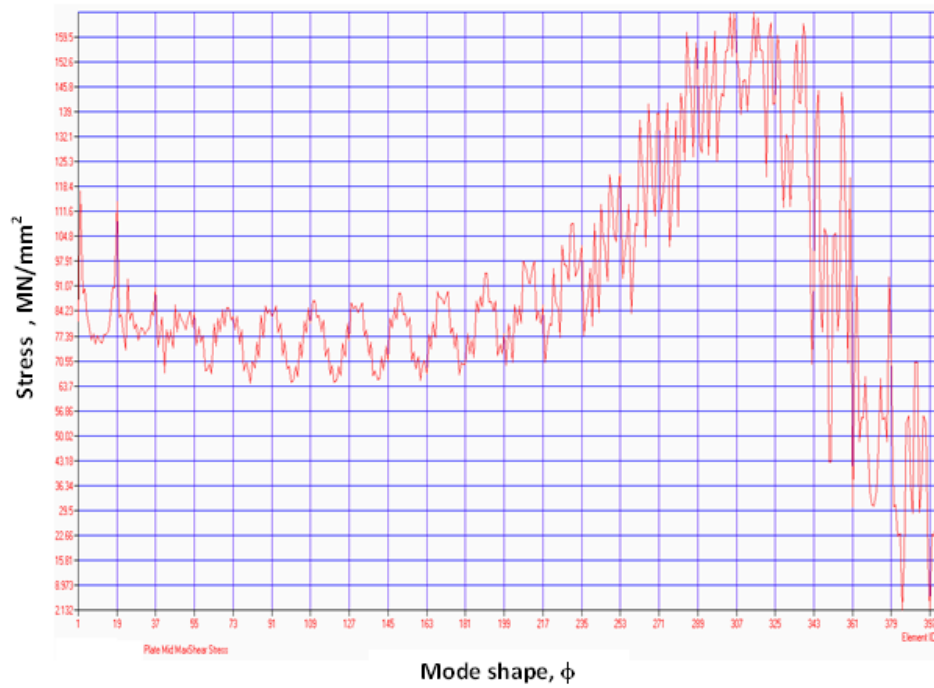
Figure(7). Residual stresses for one element.

Figure (8) show the Variation of Residual stresses of the tetrahedral structure with thickness, The strengths of the truss prevent the residual stresses to penetrable into the truss grains, and decelerates away from the boundary.



Figure(7). Variation of Residual stresses of the tetrahedral structure with thickness.

Figure(9) shows the stress distribution along the tetrahedral elements surface with mode shape, it can be seen that the higher modes show the largest stressed of the surface,



Figure(9). Stress distribution for different mode shapes.

The weakness of the truss allows the residual stresses to into the truss grains, but accelerates the residual stresses away from the boundary. Figure(10) indicate that the longer fracture life is in the higher stiffness grain boundaries , lighter damping.

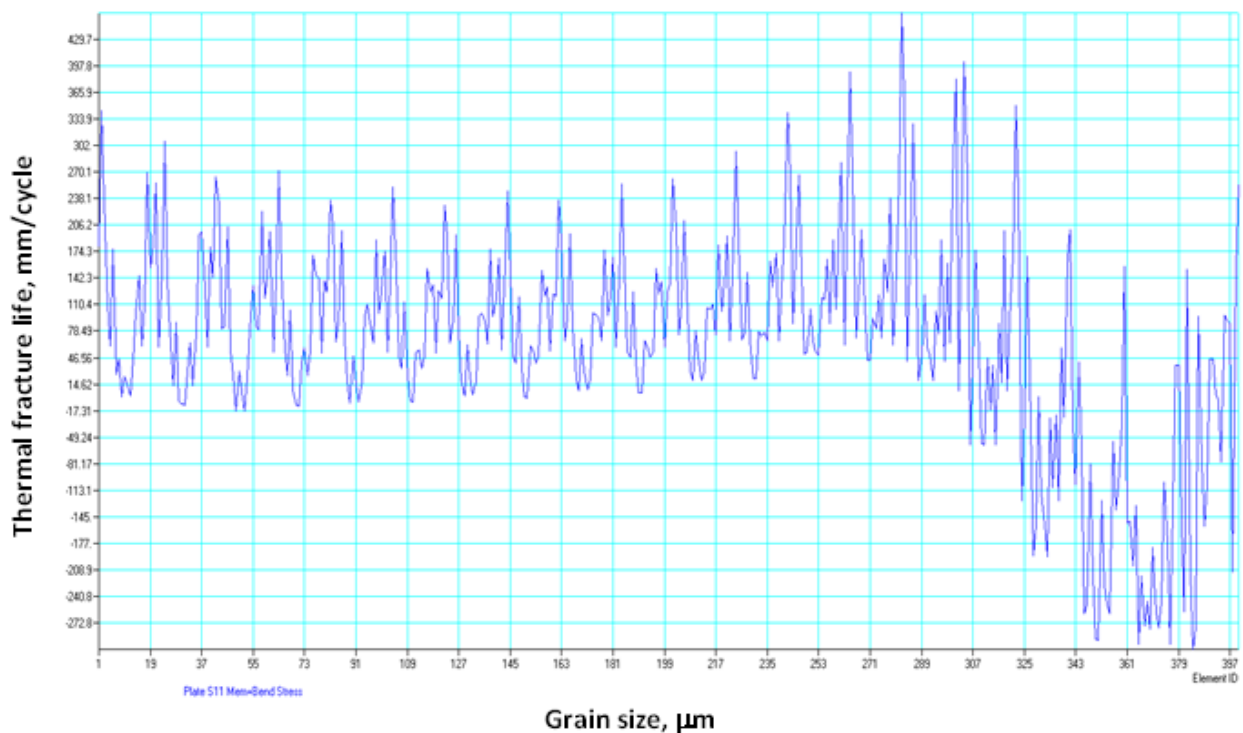


Figure (10). Thermal fracture life.

13. Conclusions

The investigation of tetrahedral elements surface structure change and the residual stress with respect to thermal deformation are studied which can be summarized as follow:

1. The thermal residual stress in the tetrahedral elements surface structure is investigated using finite element method
2. Residual stress distribution shows that tetrahedral elements surface structure is tension outward the surface and in compression inward
3. The thermal residual stress inversely increased from the elastic to plastic transition element
4. Cracks is most effective in the plastic deformation were the stress concentration is higher
5. The longer fracture life is in the higher stiffness grain boundaries, lighter damping.
6. The strengths of the truss prevent the residual stresses to penetrable into the truss grains, and decelerate away from the boundary.
7. The residual stress of the heated element is higher than the lower one.

14. References

- [1] A. Anca, A. Cardona, and J.M. Risso, 3D-THERMO-MECHANICAL SIMULATION OF WELDING PROCESSES, Universidad Nacional del Litoral–CONICET Guemes 3450, 3000, Santa Fe, Argentine .
- [2] X.Q. He, T.Y. Ng, S. Sivashanker, K.M. Liew , Active control of FGM plates with integrated piezoelectric sensors and actuators, Centre for Advanced Numerical Engineering Simulations, School of Mechanical and Production Engineering, Nanyang Technological University, Nanyang Avenue, Singapore 639798, Singapore .
- [3] S. Schaefer J. Hakenberg J. Warren, Smooth Subdivision of Tetrahedral Meshes, Eurographics Symposium on Geometry Processing (2004) R. Scopigno, D. Zorin, (Editors), Rice University .
- [4] Tae-Young Kim, Churl Seung Lee, Young Jin Lee, and Kwang-Ryeol Lee, Reduction of the residual compressive stress of tetrahedral amorphous carbon film by Ar background gas during the filtered vacuum arc process, Future Technology Research Division, Korea Institute of Science and Technology, P.O. Box 131, Cheongryang, Seoul 136-791, Korea, 2007 .
- [5] J. Grum (2002), Analysis of residual stresses in main crankshaft bearings after induction surface hardening and finish grinding, Faculty of Mechanical Engineering, University of Ljubljana, Asfkerceva 6, 1000 Ljubljana, Slovenia .

- [6]Avallone, E.A., and Baumeister, T., ed. Mark's Standard Handbook for Mechanical Engineers (10th ed.). McGraw-Hill. pp. 11–42. ISBN 0-07-004997-1.2002 .
- [7] Z. Barsoum (2007),Residual stress analysis and fatigue of multi-pass welded tubular structures, Royal Institute of Technology, Department of Aeronautical and Vehicle Engineering, Teknikringen 8, 100 44 Stockholm, Sweden .
- [8] Gary S. Schajer(2006), Residual Stress Solution Extrapolation for the Slitting Method using Equilibrium Constraints, Department of Mechanical Engineering, University of British Columbia, Vancouver, Canada.
- [9] M T Todinov (1999), Influence of some parameters on the residual stresses from quenching, School of Metallurgy and Materials, The University of Birmingham, Birmingham, UK .
- [10]Georgeta Apostol and Gheorghe Solomon (2012), parameters influence on the residual stress and distorsionat laser weld using finite element analysis, U.P.B. Sci. Bull., Series D, and Vol.74.
- [11] Chandra, U.(1993), Control of Residual Stresses, ASM handbook, Vol. 20 (Materials Selection and. Design). ASM International, New Jersey.
- [12] Khaled A. Alhazza (2002), Nonlinear Vibrations of Doubly Curved Cross-Ply Shallow Shells, Dissertation submitted to the Faculty of the Virginia Polytechnic Institute and State University .
- [13] Chaudhury, G.K. and W.D. Dover (1985), Fatigue analysis of offshore platforms subjected to seawave loading. International Journal of Fatigue .
- [14] ã H & M Analytical Services, 2002, Analysis of Residual Stresses Inc.
- [15] Van Hulle, F.J. (1991), Wind energy: Technology and implementation. Proceeding of the European Conference, Amsterdam, Netherlands.
- [16] Kozo Kishi and Hiroshi Eda,(1971), Analysis of the Structure and Thermal Residual Stress In the Machined Surface Layer by Grinding, University, Utsunomiya, Japan.
- [17] T.L. Becker Jr. b, R.M. Cannon a, R.O. Ritchie, (1999) , An approximate method for residual stress calculation in functionally graded materials, University of California, Berkeley, USA .

15. Notations

List of Symbols

A	cross-sectional area	(mm ²)
c	crack size	(μm)
D	grain diameter	(mm)
E	Modulus of elasticity	(N/m ²)
G	Modulus of rigidity	(N/m ²)
N_f	Fracture life	(mm/cycle)
σ	Normal stresses	(N/m ²)
τ	Shearing stresses	(N/m ²)
ε	Normal strains	(dimensionless)
γ	Shearing strains	(dimensionless)
μ	Coefficient of friction	(dimensionless)
δ_{ij}	Kroneker delta	(dimensionless)
C_p	Specific heat of the work	(cal/g.C ^o)
t	Element thickness	(mm)
λ	Heat conductivity	(cal/cm.sec.C ^o)
T	Temperature	(C ^o)
Q	Generated heat.	(C ^o)
α	Thermal expansion coefficient	(1/C ^o)
ν	Poisson's ratio	(dimensionless)

Predicting Punching Shear Strength of Ferrocement Slabs Using Back-Propagation Neural Network

Mohammed A. Mashrei

Civil Engineering Department

College of Engineering

Thi_Qar University

moha74ed@yahoo.com

Abstract

A back-propagation neural network (BPNN) model is developed to predict the punching shear strength of square ferrocement slabs. The experimental data used for training and testing the neural network model, are collected from several sources. They are arranged in a format of seven input parameters (the effective span, slab thickness, yield tensile strength of wire mesh, volume fraction of wire mesh, mortar compressive strength, width of square loaded area, boundary condition of the supported slabs) and one output parameter (punching shear strength). A parametric study is carried out using BPNN to study the influence of each parameter affecting the punching shear strength of ferrocement slabs. A comparison with the experimental results and those from other existing empirical equations demonstrates that the predictions from BPNN are indeed better. We conclude that the BPNN model may serve as a good tool for predicting the punching shear strength.

Keywords: Ferrocement; Punching shear; Slabs; Strength; BPNN.

التنبؤ بمقاومة القص للسقوف الفيروسمنتية باستخدام تقنيات الشبكات العصبية

المستخلص

استخدمت خوارزمية التعقب الخلفي للشبكات العصبية للتنبؤ بمقاومة القص للسقوف الفيروسمنتية ذات الاشكال المربعة. تم تدريب وفحص الشبكة العصبية بالاعتماد على معلومات عملية أخذت من تجارب سابقة ومن مصادر مختلفة. تم الأخذ بنظر الاعتبار العوامل المؤثرة هندسيا على تصرف السقوف بشكل عام لبناء الشبكة العصبية. مدخلات الشبكة هي: الفضاء الفعال، سمك السقف، مقاومة الخرسانة، نسبة الحديد، مقدار الخضوع للحديد، ابعاد مساحة التحميل بالإضافة إلى طريقة الإسناد المستخدمة أما المخرجات فكانت مقاومة القص للسقوف. كذلك تم في هذا البحث دراسة تأثير كل عنصر من العناصر المدخلة على مقاومة القص للسقوف الفيروسمنتية. تم مقارنة النتائج التي تم الحصول عليها في بحثنا هذا مع بعض النتائج العملية و مع النتائج التي تم الحصول عليها من طرق مقترحة اخرى لحساب مقاومة القص للسقوف. اثبت النتائج بان تقنية الشبكات العصبية وباستخدام خوارزمية التعقب الخلفي هي طريقة جيدة لحساب مقاومة القص ويمكن اعتمادها للتنبؤ بأي نموذج آخرى ضمن حدود البيانات المستخدمة في بحثنا هذا.

1. Introduction

With the rapid progress in innovative construction techniques, application of ferrocement is becoming increasingly common for use in various structural engineering applications. This has led significant research activities for this material resulting in considerable volume of technical information on design, construction, maintenance and rehabilitation techniques using ferrocement.

Ferrocement is a composite material constructed by cement mortar reinforced with closely spaced layers of wire mesh [1-5]. The ultimate tensile resistance of ferrocement is provided solely by the reinforcement in the direction of loading. The compressive strength is equal to that of the unreinforced mortar. However, the analysis and design of ferrocement elements is complex and is based primarily on the reinforced concrete analysis using the principles of equilibrium and compatibility [6]. Most of the applications of ferrocement is in civil engineering structures are for the situations where high tensile strength or small crack width is the governing criteria. Also the use of ferrocement is not limited to stressed skin elements alone. In applications with ferrocement as plate structural elements, it becomes necessary to understand the punching shear behavior of ferrocement. There are few papers available in the literature on the behavior of ferrocement slabs under punching shear. Paramasivam and Tan [7] presented an experimental study to evaluate the punching shear strength of ferrocement slabs. They considered the effect of the effective span to depth ratio, thickness of the slab, volume fraction of reinforcement, mortar strength, size of the load bearing plate and the spacing of the skeletal steel. Mansur et al. [8] considered a tests on 31 simply supported square ferrocement slabs under a central concentrated load to estimate the punching shear. All slabs failed in punching shear. Authors found that the punching shear increased with an increase in the thickness of the slab, volume fraction of reinforcement, mortar strength, size of the load bearing plate and decrease as the effective span is increased. Based on the experimental results, they developed an empirical formula to estimate the punching shear strength. Al-Kubaisy and Jumaat [9] presented a study on the behavior of simply supported ferrocement slabs under punching shear. The effects of the parameters as presented in [7] and shape of the loading area on the punching shear strength are examined. Mansur et al. [10] carried out an experimental study on a 14 restrained ferrocement slabs under a central load. The slab are supported and restrained on all four sides by edge ribs. They investigated the punching shear strength of slab and effect of the degree of the end restrained in adding to the effect of thickness of slab, mortar strength, size of loaded area and volume fraction of reinforcement.

The relationships used to estimate the punching shear strength are empirical formula and their predictive abilities are limited by the corresponding data sets from which they are derived. In some cases, these methods do not provide reliable predictions for use in practice. Over the last few years or so, the use of an alternative approach to modeling based on artificial neural networks (ANNs) has increased in many areas of engineering. In particular, ANNs have been applied to many structural and geotechnical engineering problems. Neural networks are an observational model developed on the basis of available data representing a mapping between input and output variables. The main advantage of ANNs is that one does not require an explicit model or equation, which is a prerequisite in the conventional approach [11]. In other words, when the information available for constructing the model is only available in the form of data derived from observations or measurements, neural network models, based on the input/output variables systems, have been successfully used to generate the relationships between these variables. The typical ANN model consists of a number of artificial neurons variously known as processing elements or nodes that are usually arranged in layers, more information on the use of ANN models in engineering applications may be found in ([12,13]. Back-propagation neural network are the most commonly used type of networks in structural engineering applications where a set of input parameters are mapped through single or several hidden layers, using weights, into output parameters.

The purpose of this study is to develop a BPNN based model to evaluate the punching shear strength of ferrocement slabs. The performance of the BPNN model is compared with experimental data and other empirical models. The developed BPNN model is also utilized to evaluate the effect of various variables which govern the behavior of such structure. The study is based on an available database resulting from tests on 68 specimens.

2. Existing models to estimate punching shear strength

Several models have been proposed to theoretically predict the punching shear strength of ferrocement slab. A brief summary of select models only are given in the following:

2.1- ACI building code equations[14]

The punching shear strength of ferrocement slabs was estimated using the equation proposed for reinforced concrete by ACI 318 code. The punching shear strength (V_u) is taken as the smallest of the following

$$a) \quad V_u = \left(2 + \frac{4}{\beta}\right) \sqrt{f'_c} u_o d \quad (1)$$

$$b) \quad V_u = \left(\frac{\alpha_s d}{u_o} + 2 \right) \sqrt{f'_c} u_o d \quad (2)$$

$$c) \quad V_u = 4 \sqrt{f'_c} u_o d \quad (3)$$

2.2-Al-Kubaisy and Jumaat equation[9]

An empirical equation is proposed by Al-Kubaisy and Jumaat to predict the punching shear strength based on tested ferrocement slabs. The proposed equation can be written as

$$V_u = u_{cr} \cdot d \cdot [0.07(f_{cu})^{0.5} + 0.35(\rho)^{1.1}] \left(\frac{h}{30} + 0.2 \right)^{1.25} \left(\frac{100}{a} \right)^{0.5} \quad (4)$$

where:

$$u_{cr} = 4 \left[0.75a + \frac{5.32 \cdot h + 0.25a}{\sqrt{2}} \right]$$

f_{cu} : cube compressive strength ≤ 60 N/mm²

ρ : $100 A_s / b \cdot d \leq 3$

h : total thickness ≤ 30 mm

a : side dimension of a square loaded area or equivalent square for rectangular or circular loaded area

2.3-Mansur et al. equation [8]

Mansur et al. presented an empirical equation to predict the punching shear strength of ferrocement. The final expression of proposed equation is given in the following

$$V_u = 0.45 (f'_c)^{1/3} (v_f)^{0.5} \left(\frac{h}{l} \right)^{1/3} \cdot u_o \cdot h \quad (5)$$

where

$$u_o = 4(w + 2 \cdot k \cdot h)$$

$$k = 1.5$$

3. Neural network

3.1 Neural network architecture

A Neural network model may be thought of as black box device that accepts inputs and produces outputs [15]. The commonest type of artificial neural network consists of three groups or layers of units: input layer units connected to one or two layers of hidden units which is/are connected to a layer of output units. The function of input layer is to receive input or information from the outside world, and to pass this information to the network for processing. These may be either sensory input or signals from other systems outside the one being modeled.

The number of input neurons corresponds to the number of input variables into the neural network, and the number of output neurons is the same as the number of desired output variables. The number of neurons in the hidden layer(s) depends on the application of the network. In engineering problems, the numbers of input and output parameters are generally determined by design requirements.

As inputs enter the input layer from an external source, the input layer becomes activated and emits signals to its neighbors (hidden layer) without any modification. Neurons in the input layer act as distribution nodes and transfer input signals to neurons in the hidden layer. The neighbors receive excitation from the input layer, and in turn emit an output to their neighbors (second hidden layer or output layer). Each input connection is assigned weight factor or connection strength. The strength of a connection between two neurons determines the relative effect that one neuron can have on another.

3.2 Elements of neural networks

The basic component of a neural network is the neuron, also called node, or the processing element (PE). Nodes contain the mathematical processing elements which govern the operation of a neural network. Figure 1 illustrates a single node of a neural network, in which it can be distinguished:

a- Inputs and outputs

Inputs are represented by a_1, a_2, \dots, a_n , and the output by b_j . Just as there are many inputs to a neuron, there should be many input signals to the PE. The PE manipulates these inputs to give a single output signal.

b- Weighting factors

The values $w_{1j}, w_{2j}, \dots, w_{nj}$ are weight factors associated with each input to the node. This is something like the varying synaptic strengths of biological neurons. Weights are adaptive coefficients within the network that determine the intensity of the input signal. Every input (a_1, a_2, \dots, a_n) is multiplied by its corresponding weight factor ($w_{1j}, w_{2j}, \dots, w_{nj}$), and the node uses this weighted input ($w_{1j} a_1, w_{2j} a_2, \dots, w_{nj} a_n$) to perform further calculations. For a positive weight factor, ($w_{ij} a_i$) tends to excite the node, and for a negative weight factor, ($w_{ij} a_i$) inhibits the node. In the initial setup of a neural network, weight factors may be chosen according to a specified statistical distribution. Then these weight factors are adjusted during the development of the network or learning process.

c- Internal threshold

The other input to the node is the node's internal threshold, T_j . This is a randomly chosen value that governs the activation or total input of the node through the following equation [15].

$$\text{Total activation} = X_i = \sum_{i=1}^n (w_{ij} a_i) - T_j \quad (6)$$

The total activation depends on the magnitude of the internal threshold T_j . If T_j is large or positive, the node has a high internal threshold, thus inhibiting node-firing. If T_j is zero or negative, the node has a low internal threshold, which excites node-firing [15]. If no internal threshold is specified, a zero value is assumed.

d- Transfer functions

The node's output is determined by using a mathematical operation on the total activation of the node. This operation is called a transfer function. The transfer function can transform the node's activation in a linear or nonlinear manner [15].

3.3 Training the network

Training is the process by which the neural network systematically adjusts the weights of interconnections between nodes so that the network can predict the correct outputs for a given set of inputs. There are many different types of training algorithms. One of the most common classes of training algorithms for feed-forward interlayer networks is called back-propagation. In a back-propagation algorithm, a set of inputs is fed to the network and outputs are returned. Then, the network compares its output with the output of the actual data set. The network calculates the amount of error between its predicted output and the actual output. The network works backwards through the layers, adjusting the weight factors according to how much error it has calculated in its output. Once all of the weight factors have been adjusted, the network works in a forward path, taking the same input data to predict the output, based on the new weight factors. The network again calculates the error between the predicted and actual outputs. It adjusts the weight factors and the process continues iteratively, until the error between the predicted and actual outputs has been minimized.

3.4 Generalization

After learning or training, the network should extract regularities or rules from the training data and be able to generalize (during testing), to give the right answers for input not belonging to the training sets. When the network is trained with a randomly selected set of

examples and tested with another set of inputs, the expected number of correct results is called generalization capability. Generalization capability can be used to evaluate the behavior of the ANN [16].

4. BPNN model: This study

A BPNN model developed for this study is used to predict the punching shear strength of ferrocement slabs. The Neural Network Toolbox of MATLAB [17] is used to develop a BPNN model for this problem. The results from the available study in the literature[7-10] were used to compile a set of 68 experimental data, which is divided into two groups, one for training and another for testing.

Seven variables are selected as input to BPNN model. These variables are: the effective span (l), slab thickness (h), yield tensile strength of wire mesh (f_y), volume fraction of reinforcement (v_f), mortar compressive strength (f'_c), width of square loaded area (w), boundary condition of the supported slabs (r). The output variable is the punching shear strength of ferrocement slab. Table 1 summarizes the ranges of the different variables. The data used in this study are summarized in Table A in the Appendix.

Through a set of trials, a network of two hidden layers with five neurons in each layer was found to yield an optimal configuration, with minimum mean square error (MSE). The number of hidden layers, number of hidden nodes, and transfer functions are chosen to get the best performance of the model. After the errors are minimized, the model with all the parameters including the connection weights is tested with a separate set of testing data that is not used in the training phase. At the end of the training, the neural network represents a model that should be able to predict the target value (punching shear strength) for given the input pattern.

The network was trained continually through updating of the weights until the final error of 1.37×10^{-3} was achieved after 500 epochs. Figure. 2 shows the performance for training and testing data sets. The network performance with back-propagation training algorithm have been tested for training and testing patterns, as shown in Figures. 3 and 4. The predicted values were found to be in good agreement with the actual (target) values.

5. Graphical user interface (GUI) of BPNN program

The graphical user interface (GUI) developed for the BPNN program is presented in Figure. 5. GUI provides a user friendly platform run the analysis using intuitive text boxes. The GUI represents a simplified tool to use the developed neural network to predict the punching shear strength of ferrocement slab. A window is provided through which the input

data is introduced and the results of network are displayed in the same window or in an output file. The results include the output of the network and the regression analysis for both the training and testing phases. The main advantage of the GUI is the short time that used to predict the punching shear strength. nine seconds is enough to get the result.

6. Parametric study

Once the artificial neural network has been trained, a parametric analysis is conducted to study the influence of the various parameters on the punching shear strength of slabs. The most important conclusions are given in the following.

In Figure (6) the punching shear strength of ferrocement slab is plotted versus the total thickness of slab (h). It can be clearly seen from the figure that an increases in h causes the punching shear strength to increase. This is so because larger h increases the stiffness and strength of slab. This conforms to the observations reported by [8-10].

Figure (7) shows the effect of compressive strength of mortar (f'_c) on punching shear strength of ferrocement slab. It can be seen from this figure that as (f'_c), increases, the punching shear strength slightly increased. A reasonable agreement is achieved between the results from experiments [8,10] and those of the neural network.

The influence of the volume fraction of reinforcement (v_f) on the punching shear strength as predicted by artificial neural network is presented. Figure (8) shows that the punching shear strength can be improved substantially by an increase in v_f . In general this finding is in agreement with other experimental results [7-10].

The width of square loaded area (w) also, is important parameter, because this parameter has significant effect on behavior of ferrocement in punching shear. Figure (9) shows that the punching shear strength increases with an increase in w . This is because a larger load area required a longer critical perimeter for punching shear to occur. The increase in critical perimeter means a higher load, as also concluded by Mansur et al. [8].

The effective span (l) also has an influence on the punching shear strength of ferrocement slabs. Figure(10) shows that the relationship between the effective span and punching shear strength. It can be seen that when l decrease the shear strength increase. In other words, a decrease in the l/h ratio that achieved by changing the effective span length leads to increase the punching shear strength, but the increase is not as pronounced as in the case of changing the depth. These results are in agreement with other experimental results by [8,9].

Finally, the influence of end restraint on the punching shear strength of ferrocement slabs it may be observed in Figures(6 to 10). It can be concluded that the restrained slabs exhibited

higher strength than the corresponding simply supported slabs. Mansur et al. [10] attributed that to the development of higher membrane stresses in the restrained slabs. It should be noted that the range of data of restrained slabs considered in our model is very limited because of the data available. The authors are aware of this limitation.

7. BPNN prediction: Comparison with experimental and theoretical results

The predictions of punching shear strength of ferrocement slabs as obtained from BPNN, ACI code and two empirical equation as mentioned in section 2 are compared with the experimental results and shown for both training and testing sets in Figures(11 and 12) and Table (2).

Table (2) summarizes the average and standard deviation of the ratio of the experimental punching shear strength (V_e) to predicted (V_i). The BPNN model gives an average V_e/V_i ratio for training and test data sets of 1.0 and 1.07, and standard deviation of 0.1 and 0.14, respectively. These values indicate that the proposed BPNN model can predict more reliably the punching shear strength compared to the other three models. Figures (11 and 12) confirm the same conclusion that the predictions of BPNN model are better than those of the three empirical models. Table (3) also confirms this conclusion when comparing the correlation factor coefficient for all models for both training and test data sets. Values of 0.995 and 0.96 for the BPNN training and test data sets, respectively, are close to 1.0 and higher than that of the other three models.

8. Conclusion

In this study a model based on back-propagation neural network (BPNN) is developed to predict the punching shear strength of ferrocement slabs. A database from the results of sixty eight (68) tests is data developed from the review of literature, which is used for the training and testing of this BPNN model. Seven variables are selected as input to BPNN model with one target variable, punching shear strength.

A parametric study based on BPNN demonstrates that the network is able to learn and generalize, and thus captures quite well effect of each input variables on the final output.

The predictions of punching shear strength of ferrocement from BPNN model are compared those from three other available empirical models, as well as to those from experimental results. It is found that the predictions from BPNN are indeed better. We conclude that the BPNN model may be serve as a good tool for predicting the punching shear strength.

Table (1). Range of input parameters in the database.

No.	Parameter	Range
1	l (mm)	400-1200
2	h (mm)	10-70
3	f'_c (MPa)	21.5-72.6
4	f_y (MPa)	362-485
5	v_f	1.01-7.6
6	w (mm)	40-200
7	r	Simply supported slabs (S.S) or restrained slabs (R.S)

Table (2). Comparison of punching shear prediction.

Data set	No. Spec.	Average of V_e / V_i				STDEV of V_e / V_i			
		BPNN	ACI [14]	Mansur et al. [8]	Al Kubasy and Jumaat [9]	BPNN	ACI [14]	Mansur et al. [8]	Al Kubasy and Jumaat [9]
Training	56	1.00	0.76	1.23	1.46	0.10	0.24	0.24	0.51
Testing	12	1.07	0.81	1.26	1.45	0.14	0.22	0.20	0.42

Table (3). Comparison of correlation coefficient, R.

Model	R	
	Training	Testing
BPNN	0.995	0.96
ACI [14]	0.89	0.79
Al Kubasy and Jumaat [9]	0.89	0.74
Mansur et al. [8]	0.96	0.92

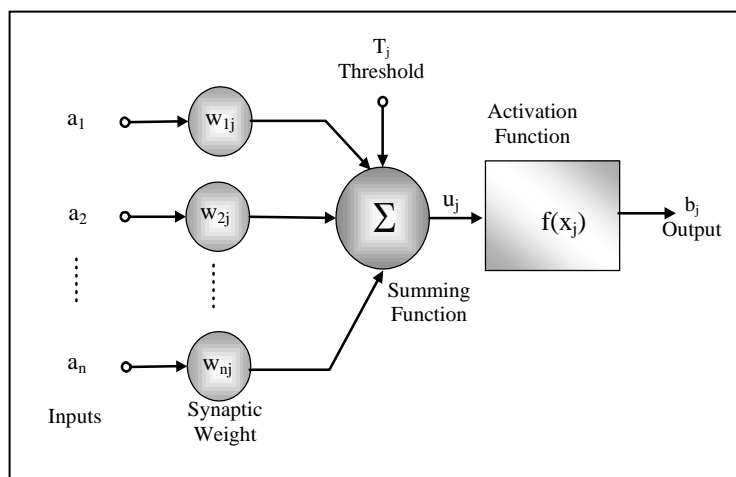


Figure (1). Single node of a neural network.

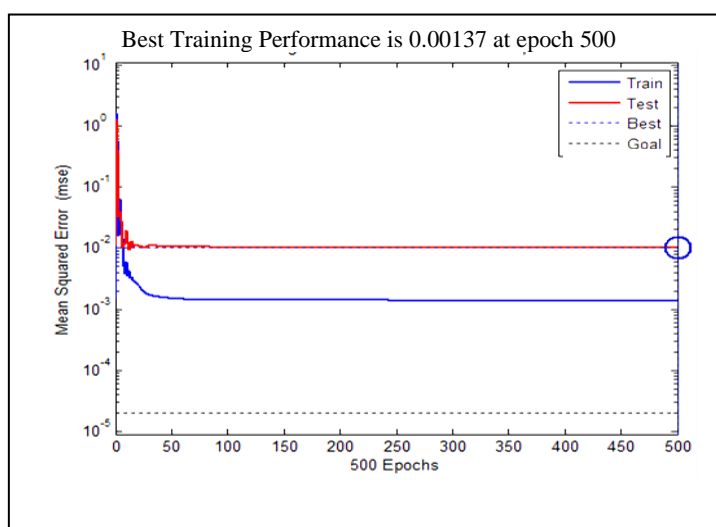
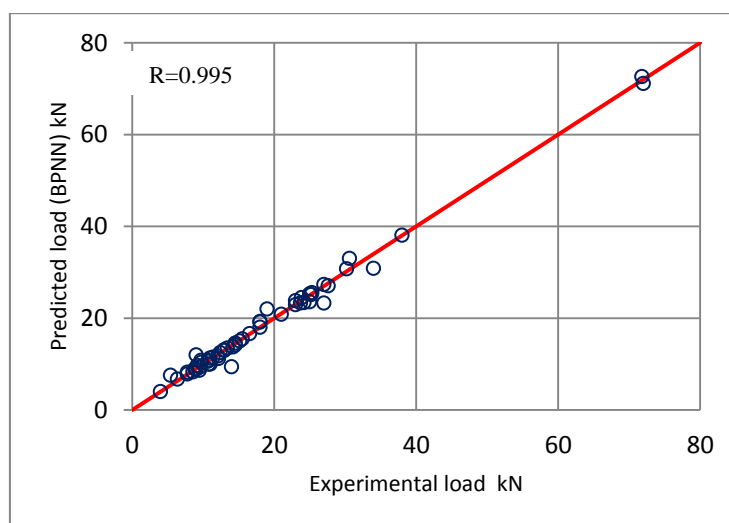


Figure (2). Convergence of the BPNN for training and testing sets.



Figure(3) .BPNN punching shear strength for training data set.

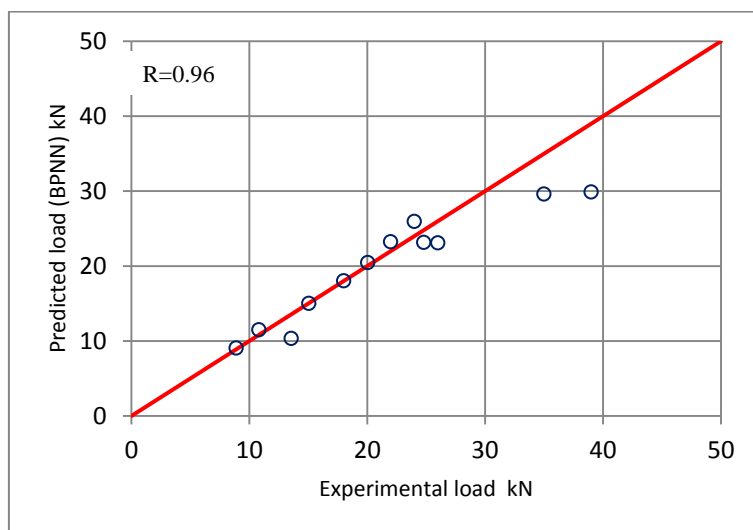


Figure (4). BPNN punching shear strength for testing data set.

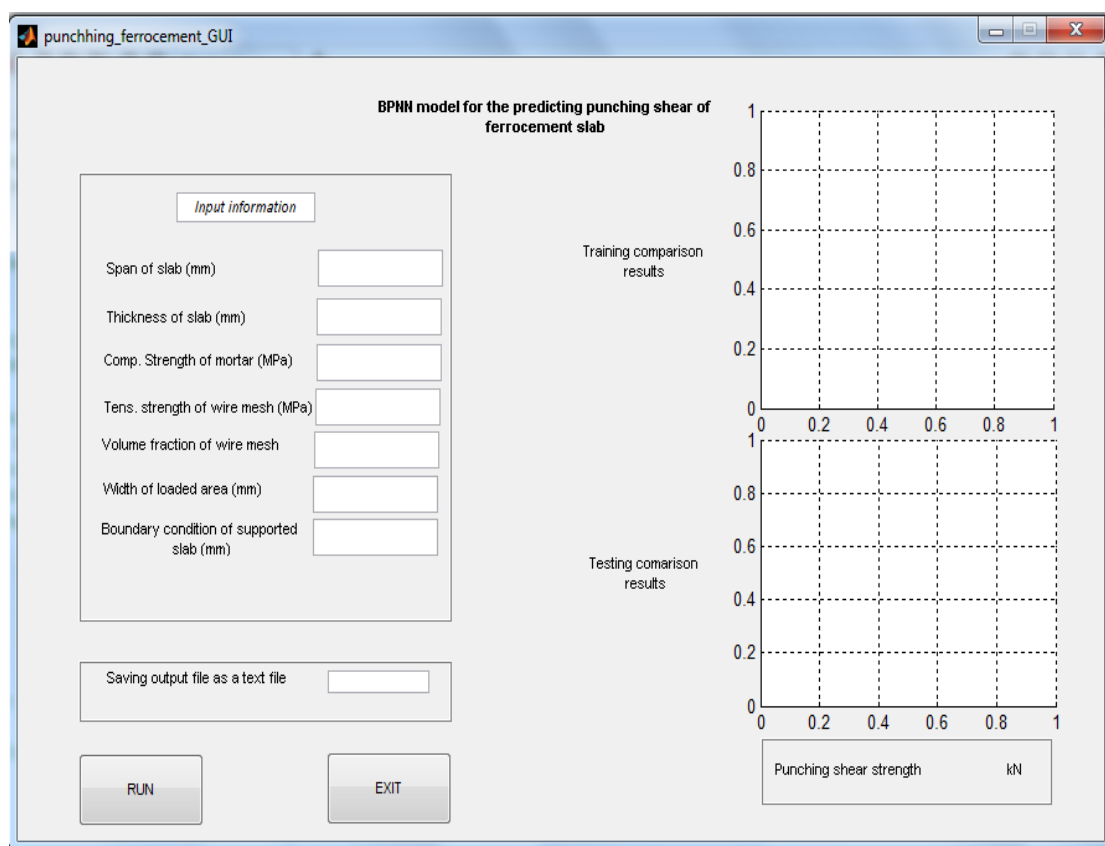


Figure (5). User friendly GUI for BPNN model.

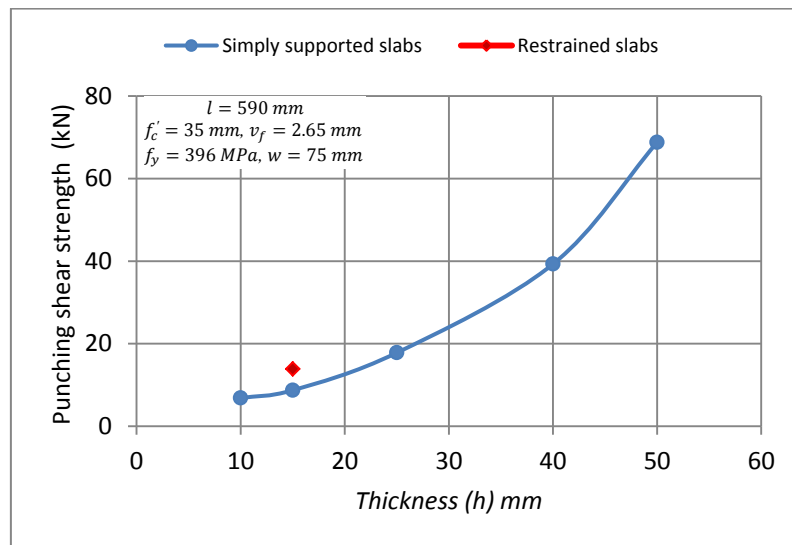


Figure (6). Effect of slab thickness on Punching shear strength.

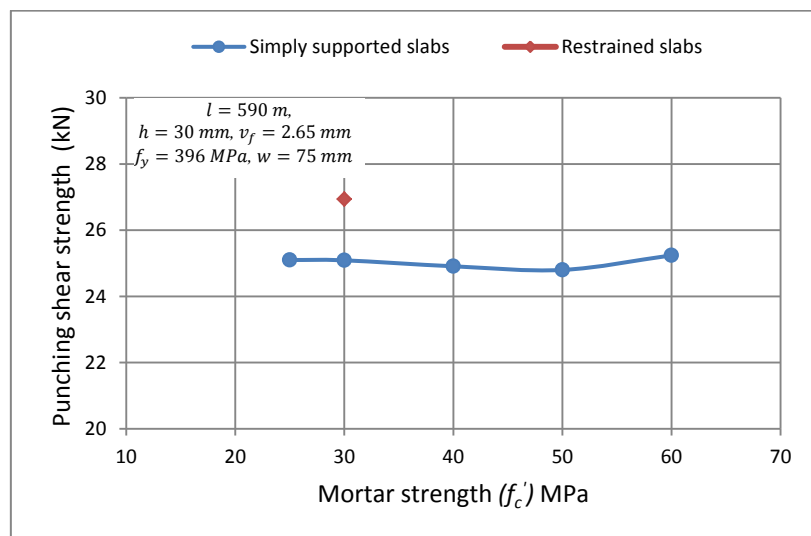


Figure (7). Effect of mortar compressive on strength punching shear strength.

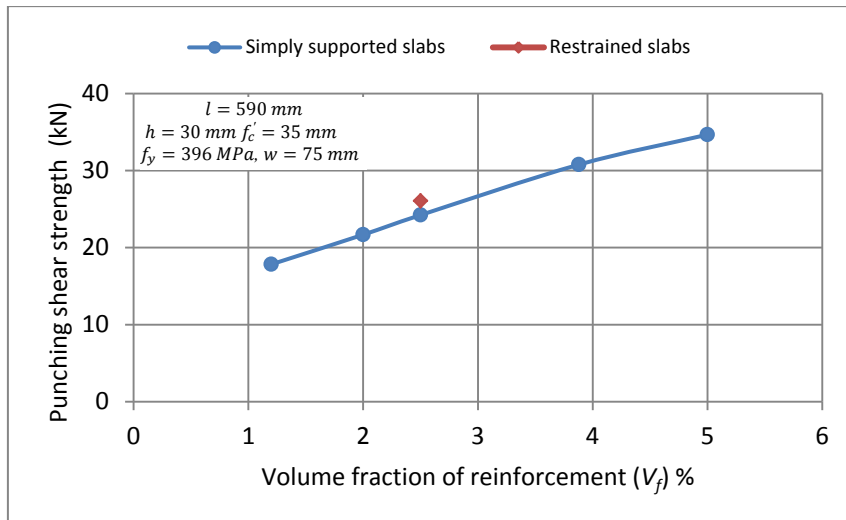


Figure (8). Effect volume fraction on punching shear strength.

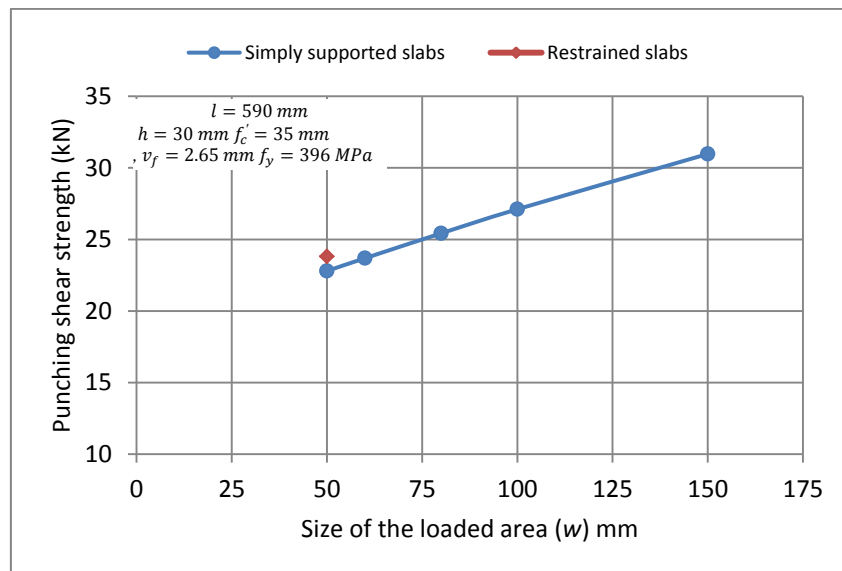


Figure (9). Effect of size of loaded area on punching shear strength.

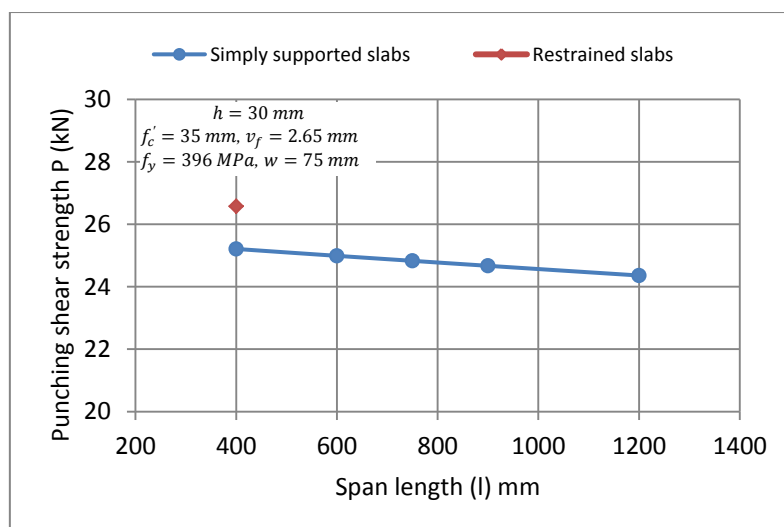


Figure (10). Effect of span length on punching shear strength.

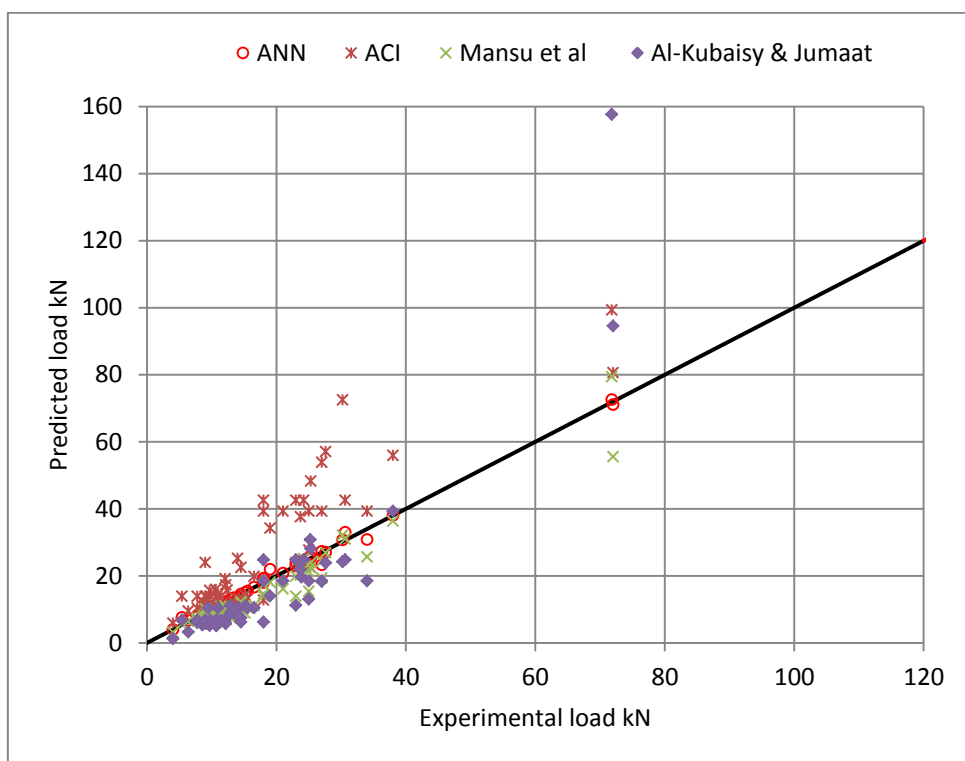


Figure (11). Experimental versus predicted punching shear for training data sets.

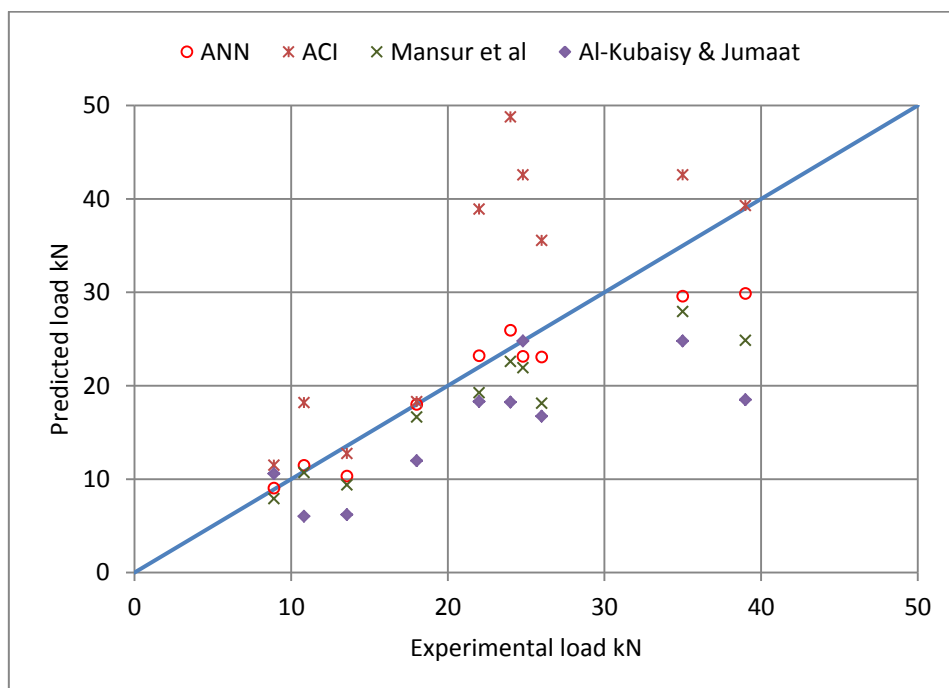


Figure (12). Experimental versus predicted punching shear for testing data sets.

9. References

- [1] Naaman A E. Ferrocement and Laminated Cementitious Composites. Ann Arbor, Michigan, USA: Techno Press 3000; 2000. p. 372.
- [2] Shah P. New Reinforcing Materials in Concrete. Journal of ACI, 1974; 71(5): 257-262.
- [3] Paul B K, Pama R P. Ferrocement. International Ferrocement Information Center, IFIC Pub., 1978.
- [4] Lee S L. Raisinghani, M, Pama R P. Mechanical Properties of Ferrocement. FAO Seminar on the Design and Construction of Ferrocement Vessels, 1972.
- [5] ACI Committee 549. State-of-the Art Report on Ferrocement. ACI, 549-R97, in Manual of Concrete Practice, ACI, Detroit, 1997.
- [6] Rao C T, Rao T D, Rao N V. An Appraisal of the Shear Resistance of Ferrocement Elements. ASIAN Journal of Civil Engineering (Building and Housung), 2006; 7(6): 591-602.
- [7] Paramasivam P, Tan K. Punching Shear Strength of Ferrocement Slabs. ACI Structural Journal, 1993; 7(3): 294-301.
- [8] Mansur M, Ahmad I, Paramasivam P. Punching Shear Strength of Simply Supported Ferrocement Slabs. Journal of Materials in Civil Engineering, 2001; 13(6): 418-426.
- [9] Al-Kubaisy M, Jumaat M. Punching Shear Strength of Ferrocement Slabs. Journal of Ferrocement, 1999; 29(2): 99-114.
- [10] Mansur M, Ahmad I, Paramasivam P. Punching Shear Behavior of Restrained Ferrocement Slabs. ACI Structural Journal, 2000; 97(5): 765-773.
- [11] Nehdi M, Djebbar Y, Khan A. Neural Network Model for Preformed-Foam Cellular Concrete. Materials Journal, 2001; 98(5): 402-409.
- [12] Rafiq M, Bugmann G, Easterbrook D. Neural network design for engineering applications, Journal of Computers and Structures, 2001; 79(17): 1541-1552.
- [13] Mashrei M, Abdulrazzaq N, Abdalla T, Rahman M. Neural networks model and adaptive neuro-fuzzy inference system for predicting the moment capacity of ferrocement members, Journal of Engineering Structures, 2010; 32(6): 1723-1734.
- [14] American Concrete Institute (ACI). Building code requirements for reinforced concrete. ACI 318-08.
- [15] Baughman, D R., Liu, Y A. Neural Network in Bioprocessing and Chemical Engineering, Academic Press, San Diego, CA, 1995.
- [16] Cheung H W. Neural Network Aided Aviation Fuel Consumption Modeling. M.Sc. Thesis, Virginia Polytechnic Institute and State University, 1997.
- [17] Neural Networks Toolbox User's Guide for Use with MATLAB, 2009.

10. Notation

A_s : cross-sectional area of reinforcement (wire mesh)

b : side dimension of square slab

d : effective depth of slab

f'_c : compressive strength of mortar

f_y : yield strength of wire mesh

h : total depth of slab

l : span length

r : boundary condition of the supported slabs

u_o : rectangular critical perimeter at distance $0.5d$ from face of column

V_u : punching shear strength

v_f : volume fraction of wire mesh

w : size of loaded area

α_s : constant used to compute shear strength in slab

β : ratio of long to short sides of the loaded area or column

ρ : reinforcement ratio

Appendix

Table (A). Experimental data used to construct the BPNN model

Test No.	l mm	h mm	f'_c MPa	f_y MPa	v_f mm	w mm	r mm	V_u kN	References
1	400	20	47.5	364	2.53	40	S.S	9.45	Mansur et al. [8]
2	400	20	52.7	364	2.53	40	S.S	8.9	
3	400	20	47.5	364	2.53	80	S.S	10.82	
4	400	20	57	364	2.53	50	S.S	10.75	
5	400	20	47.5	364	2.53	50	S.S	9.48	
6	400	20	57	364	2.53	60	S.S	10.63	
7	400	20	47.5	364	2.53	60	S.S	11	
8	400	20	52.7	364	2.53	80	S.S	12.06	
9	400	20	35.2	364	2.53	50	S.S	8.55	
10	400	20	35.2	364	2.53	80	S.S	9.68	
11	400	20	42.8	364	2.53	40	S.S	7.76	
12	400	20	42.8	364	2.53	50	S.S	8.82	
13	400	20	42.8	364	2.53	60	S.S	9.17	
14	400	20	42.8	364	2.53	80	S.S	12.16	
15	400	20	72.6	364	2.53	50	S.S	12.38	
16	400	20	72.6	364	2.53	80	S.S	14.5	
17	400	20	56.5	413	1.01	50	S.S	5.39	
18	400	20	56.5	362	1.93	50	S.S	9.75	
19	400	20	47.5	365.5	3.16	50	S.S	13.56	
20	400	25	54.7	362	3.86	50	S.S	18.02	

21	400	20	47.5	364	5.06	50	S.S	14.5	Paramasivam and Tan [7]
22	400	20	47.5	364	7.6	50	S.S	18	
23	400	10	54.7	362	3.86	50	S.S	3.99	
24	400	15	54.7	362	3.86	50	S.S	6.37	
25	400	20	54.7	362	3.86	50	S.S	11.38	
26	400	30	54.7	362	3.86	50	S.S	23.84	
27	600	20	56.5	364	2.53	50	S.S	9	
28	900	20	56.5	364	2.53	50	S.S	7.76	
29	600	35	46.6	485	1.94	100	S.S	24.2	
30	1200	35	46.6	485	1.94	100	S.S	23	
31	900	35	46.6	485	1.21	100	S.S	18	
32	900	35	46.6	485	3.88	100	S.S	30.6	
33	900	22	50.64	485	1.94	100	S.S	14	
34	900	57	46.6	485	1.94	100	S.S	72	
35	900	70	40	485	1.94	100	S.S	71.8	
36	900	35	36.4	485	1.94	100	S.S	23.7	
37	900	35	60	485	1.94	100	S.S	25.3	
38	900	35	44.6	485	1.94	200	S.S	30.2	
39	900	35	46.6	485	1.94	100	S.S	24.8	
40	900	35	46.6	485	3.15	100	S.S	35	
41	900	35	44.6	485	1.94	150	S.S	27.6	
42	750	30	58.24	406	3.55	100	S.S	34	Al-Kubaisy and Jumaat [9]
43	750	30	58.24	406	2.44	100	S.S	25	
44	750	30	58.24	403	2.03	100	S.S	27	
45	750	30	58.24	390	1.4	100	S.S	21	
46	750	30	58.24	390	1.05	100	S.S	18	
47	750	20	57.28	409	2.38	100	S.S	9	
48	750	27	57.28	399	2.61	100	S.S	19	
49	750	40	57.28	406	2.5	100	S.S	38	
50	750	30	21.5	403	2.03	100	S.S	23	
51	750	30	29	403	2.03	100	S.S	25	
52	750	30	57.12	403	2.03	150	S.S	27	
53	750	30	58.24	406	3.34	100	S.S	39	
54	750	30	47.7	403	2.03	100	S.S	26	
55	750	30	57.12	403	2.03	133	S.S	24	
56	750	30	57.12	403	2.03	100	S.S	22	
57	420	20	55.6	364	2.53	40	R.S	12.9	Mansur et al. [10]
58	420	20	50.8	364	2.53	50	R.S	14.2	
59	420	20	56.3	364	2.53	80	R.S	16.54	
60	420	20	33.4	364	2.53	50	R.S	12.97	
61	420	20	43.5	364	2.53	50	R.S	13.4	
62	420	20	60	364	2.53	50	R.S	15.13	
63	420	20	50.8	364	1.93	50	R.S	10.95	
64	420	20	50.8	364	3.86	50	R.S	15.51	
65	440	15	50.8	364	3.86	50	R.S	10.71	
66	440	30	50.8	364	3.86	50	R.S	25.21	
67	420	20	55.6	364	2.53	60	R.S	15.06	
68	440	25	50.8	364	3.86	50	R.S	20.06	

Experimental Enhancement of the Thermal Conductivity for Mortar Concrete by Adding Polystyrene

Mohammed Wahhab Aljibory

Mechanical Engineering Department

Karbalaa University

maljibory71@yahoo.com

Mobile-009647801154038

Abstract

This paper gives an experimental study for the thermal conductivity of mortar concrete material by adding polystyrene (styropr) as granules for different volume percentages (0%, 5% , 10% and 15 %). Polystyrene considered as a polymeric thermal isolative material. The specimens of 343 cm³ are made with a mixing percentages of 22.72% cement, 68.18% sand and 9.1% water which they accredited according to the Iraqi standardization No. (5 /1984).

Tests are carried out in the laboratories of the engineering college – Karbalaa university to determine the thermal conductivity, compressive strength, porosity and the density for the specimens. The results showed that the polystyrene leads to decrease the thermal conductivity of the mortar concrete. The thermal conductivity of the (5%) polystyrene specimen is decreased by (2.6%), (10%) polystyrene specimen is decreased by (10.4%), and for the specimen of (15%) polystyrene is decreased by (20.28%). The compressive strength of the specimen is decreased by increasing the polystyrene percentages and this clearly appear in the 10% and the 15% specimens but it isn't exceed the permissible range according to the Iraqi standardization No. 5/1984 (compressive strength ≥ 23 Mpa).

المستخلص

يعطي هذا البحث دراسة عملية للموصلية الحرارية لمادة الكونكريت (مونة) بإضافة مادة البوليسترين (الستايروبر) على شكل حبيبات بنسب حجمية مختلفة (5% , 10% و 15%). تعتبر مادة البوليسترين من المواد البوليمرية العازلة. تم تصنيع النماذج وبحجم 343 سم³ وبنسب خلط (22,72%) سمنت , (68,18%) رمل و (9,1%) ماء وحسب المواصفة العراقية (1984/5) مع اضافة المادة العازلة بالنسب اعلاه للخليط.

اجريت الفحوصات في مختبرات كلية الهندسة جامعة كربلاء لقياس الموصلية الحرارية, مقاومة الانضغاط, النفاذية, والكثافة للنماذج المصنعة.

بينت النتائج ان اضافة مادة البوليسترين ادت الى نقصان الموصلية الحرارية لمادة الكونكريت. ان اضافة حجمية بنسبة (5%) من مادة البوليسترين قللت الموصلية الحرارية بنسبة (2,6%) و اضافة (10%) من البوليسترين قللت الموصلية الحرارية بنسبة (10,4%) اما اضافة (15%) من البوليسترين فقد قللت الموصلية الحرارية بنسبة (20,28). لقد لوحظ ان مقاومة الانضغاط تقل بزيادة نسبة المادة المضافة وخصوصا بنسب (10 و 15) % ولكن دون ان تتجاوز الحد المسموح به لمادة الكونكريت وحسب المواصفة العراقية (1984/5) حيث (مقاومة الانضغاط ≤ 23 ميغا باسكال).

1. Introduction

Thermal conductivities for most polymers are on the order of 0.3 W/m.K° . For these materials, energy transfer is accomplished by the vibration and rotation of the chain molecules. The magnitude of the thermal conductivity depends on the degree of crystallization of polymer with a highly crystalline and ordered structure will have a greater conductivity than the equivalent amorphous material. This is due to the more effective coordinated vibration of the molecular chains for the crystalline state. Polymers are often utilized as thermal insulators because of their low thermal conductivities. Like ceramics, their isolative properties may be further enhanced by the generation of small pores, which are ordinarily generated by foaming during polymerization (chemical process of forming a polymer). Foamed polystyrene (styropr) is commonly used [1].

Al-Sanea [2] found that the inclusion of a 5-cm thick molded polystyrene layer reduced the roof heat transfer load to one-third of its value in an identical roof section without insulation. Hernandez-Olivares et al. [3] studied mechanical and thermal properties of a composite material that is made of cork and gypsum; they found that cork-gypsum composite is characterized by both low thermal conductivity and low density. On the other hand, the mechanical properties of cork-gypsum composite are poor, and such a composite material was suggested for use in building applications as partitions. Mohsen and Akash [4] showed that large energy savings about (76.8%) can be achieved when polystyrene is used for both wall and roof insulations. Jubran et al. [5] investigated the use of Jordan Valley clay with addition of straw, chicken feather, human hair, cement and polystyrene as insulating materials. The percentage of insulating materials in the brick ranged from 2 to 20 %. They also found that the combined additives consisting of 10 % rock wool, 5% human hair and 5% cement gave the best thermal and mechanical properties. Jaber and Hammad [6] showed that adding thermal insulation system proved to be effective nearly 82% of the estimated required heating energy was saved by using thermal insulation of 0.057 m and about 7.2 m^2 of Trombe wall system where added and the payback period was less than 2 year. Awni Al-Otoom et al

[7] presented a new technology based on crystallization of the salt solution of sodium acetate, which can be produced via the reaction of acetic acid and sodium carbonate.

The main objective of this work is to investigate the effect of the addition of some insulation materials with different weight percentages on the water absorption, compressive strength and the thermal conductivity of the mortar concrete. The objective of this arrangement besides lowering the thermal conductivity is to make the material has an emulsion capability when it is marketing.

2. Theoretical considerations

The inside door temperature of building is affected by the three modes of heat transfer: convection, conduction and radiation. The major portion of heat is transmitted into the building by conduction mode through the walls in addition to heat losses by air leakage. The thermal conductivity for steady state condition of a single wall can be calculated by the following Fourier's law [8]:

$$q_x = -kA \partial T / \partial x \quad (1)$$

Where q_x is the heat-transfer rate (W) and $\partial T / \partial x$ is the temperature gradient in the direction of the heat flow. The positive constant (k) is called the **thermal conductivity** (w/m.k) of the material, and the minus sign is inserted so that the second principle of thermodynamics will be satisfied. The composite walls involve several layers of different materials with different thermal conductivities. In the composite systems it is often convenient to work with Newton's law of cooling using the following equation:

$$q_x = UA \Delta T \quad (2)$$

In which U is the overall heat transfer coefficient (W/K.m²) and represents the sum of all parallel and series thermal resistances and ΔT is the overall temperature difference. In this research work the thermal conductivity of concrete containing different weight percentages of insulating materials are experimentally determined and compared with thermal conductivity of the concrete which do not contain any insulating materials.

3. Materials equipment and experimental procedures

3.1 Materials

The materials used throughout this work are the typical ones used in manufacturing the ordinary concrete. These are cement, sand and water with the insulating material which are used and added in different weight percentages to the concrete. The insulation material was chosen to be ease of handling, low water absorption values, low cost and low thermal conductivity [9,10].

3.2 Equipment

The Hilton B480 Thermal Conductivity of Buildings & Insulating Materials Unit instrument shown in Figure (1) was used to measure the thermal conductivity of the different manufactured specimens. The apparatus consists mainly of an insulated fiberglass hinged enclosure. The base section of the closure contains the heat flow meter and the cold plate assembly which mounted on four springs. The plate is cooled with water to maintain it at constant temperature. The enclosure lid houses the electrically heated hot plate, which is electronically controlled for setting the required temperature. A computerized system is used to determine and display the measured values of thermal conductivity.



Figure (1). Hilton B480 instrument for measuring thermal conductivity of buildings & insulating materials.

The faces of the enclosure are insulated to ensure adiabatic boundary condition and to ensure that all faces of the specimen are not in direct contact with the hot and the cold plates. This thermal conductivity measuring method is a heat flow meter method which complies with the International Standard for steady-state measurement, ISO8301, [11].

The compressive strength of the different specimens was measured using the international testing machine shown in Figures (2) and (3) respectively, where the specimen was compressed between the upper and lower hubs of the machine until fracture of the specimen had occurred. The uncertainty average of the used machine was ($\pm 0.1\%$).



Figure (2).ELE international testing machine.



Figure (3).The hubs of ELE international testing machine.

4. Experimental procedures

The experimental procedure begin with preparation of the dry concrete follow the same procedure used in preparation of the concrete, which is in accordance with the International Standards. The specimens were of the dimensions $7\text{cm} \times 7\text{cm} \times 7\text{cm} = 343 \text{ cm}^3$, and this is according to the Iraqi specification to measure the compressive strength. The insulating material (as shown in the Figure (4)) was added in different volume percentages during the preparation of the concrete specimens. The insulating material was added in the form of small granules of the polystyrene.



Figure (4). Granules of polystyrene.

Table (1) shows the weight of each material that the concrete specimen consist of and its percentage was.

Table (1) . Tabulation of each material and its percentage per specimen.

Material	Material's weight per specimen gm / specimen	The material weight percentage
Cement	185	22.72 %
Sand	555	68.18 %
Water (H ₂ O)	74	9.1 %

The insulation added as a volume percentage, where the polystyrene has a low density and these percentage listed in Table (2). For example it was evaluated as ($0.05 \times 343 = 17.15 \text{ cm}^3$).

Table (2). Tabulation of Insulation volume added for each Specimen type .

Specimen type	Insulation volume(cm³) Per specimen
0% Insulation	0.0
5% Insulation	17.15
10% Insulation	34.3
15% Insulation	51.45

The experimental work of the project was carried out in the laboratories of engineering college of Karbalaa university begin with the specimens making process. Mixing process was done by putting the cement and sand then they mixed manually properly , finally the mixture is made by adding the water with overturning it to have a homogenous mixture for four minutes as mentioned in the Iraqi standardization, as shown in Figure (5). In case of adding the insulation the cement , sand and the specified percentage of the granule of insulation (polystyrene) are putted and then mixed manually for the same period.

**Figure (5). The mixing process.**

Vibrating machine device is also used to ensure a good distribution of the mixture in the mold and expel the air (Figure (6)).



Figure (6). The Vibrating machine.

Finally, after pull out the specimen mold from the vibrating device, it is putted in an optimum condition box as shown in Figure (7) with specified condition (dry bulb Temperature = 21.4°C & relative humidity = 88%), to reach the maturation case (7days). Figure (8) shows the specimens after the process.



Figure (7) .The optimum conditions box.

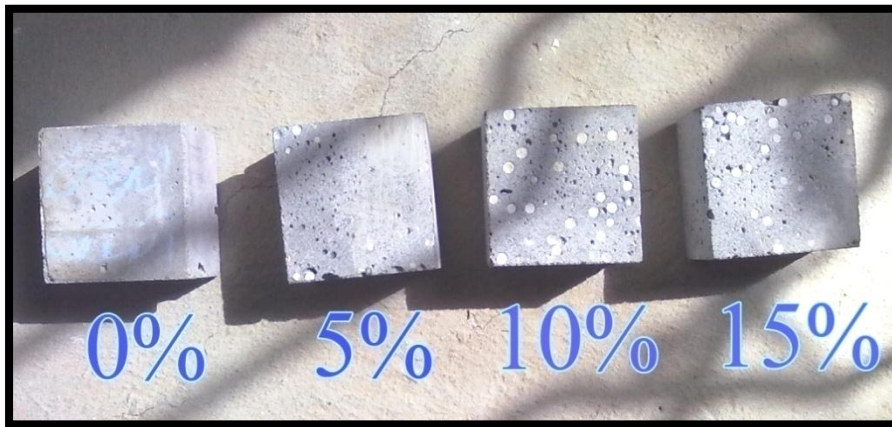


Figure (8).The specimens after the process .

5. Results and discussion

The compressive strength is measured directly by the ELE International testing machine for each specimen and the results are listed in Table (3). The readings still in the permissible range according to the Iraqi standardization number (5/1984) for the mortar concrete at maturation for 7 days which it is (compressive strength ≥ 23 Mpa).

Table (3). Tabulation of the compressive strength for each specimen.

Specimen type	Compressive strength (Mpa)
0 % Insulation	33.29
5 % Insulation	31.18
10 % Insulation	26.05
15 % Insulation	23.88

The density of each specimen is calculated by knowing the masses and the reduction in the mass for all specimens and the porosity is evaluated as:

$$\begin{aligned}\% \text{ porosity} &= \frac{\text{void volume}}{\text{total volume}} \times 100 \\ &= \frac{(m_t - m_s)}{V_s \rho_w} \times 100\end{aligned}\quad (3)$$

The masses after the specimens immersed appeared as:

$m_t(0\%) = 813 \text{ gm}$, $m_t(5\%) = 799 \text{ gm}$, $m_t(10\%) = 769 \text{ gm}$, $m_t(15\%) = 747 \text{ gm}$

therefore the results are tabulated in Table (4) for the constant specimens volume of (343 cm^3).

Table (4). Tabulation of the specimens masses and its reduction with calculated density and porosity.

Specimen type	Mass (gm)	%Reduction in mass	Density gm / cm ³	Porosity %
0 % Insulator	809	0.0	2.358	1.166
5 % Insulator	794	1.854	2.315	1.457
10 % Insulator	761	5.933	2.218	2.332
15 % Insulator	737	8.899	2.149	2.915

The effect of the volume addition of insulating material on thermal conductivity of the concrete specimens is shown in Figure (9). It can be seen from this figures that, for all the tested concrete specimens, as the volume percentages of insulator increases the thermal conductivity decreases where the overall density of the specimens decreases and the results of the thermal conductivity of each specimen are listed in the Table (5). However, the decreasing rate is more pronounced for the insulating percentage of (15%).

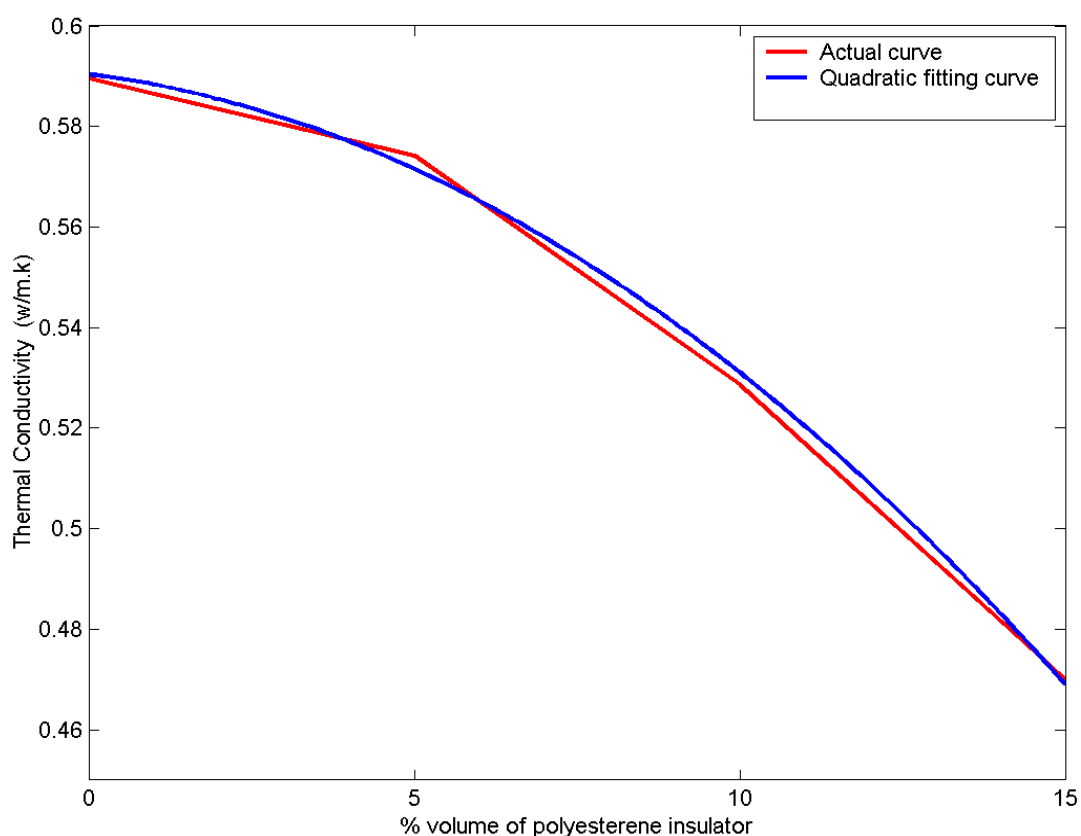


Figure (9). The relation between the thermal conductivity and the % volume of Polystyrene insulator.

Table (5). Tabulation of the Thermal Conductivity and the Percentage of Reduction .

Specimen type	Thermal conductivity (W/m.K)	Reduction of Thermal Conductivity (%)
0 % Insulator	0.5896	0.0
5 % Insulator	0.5742	2.6
10 % Insulator	0.5286	10.4
15 % Insulator	0.47	20.28

6. Conclusions

It can be concluded that the addition of a reasonable percentage of the Polystyrene (5-15)%, resulted in reduction of water absorption, decrease in the compressive strength and pronounced decrease in thermal conductivity. The most effective Polystyrene percentage in reducing thermal conductivity of concrete is found to be (15%) which leads to reduce the thermal conductivity by (20.28%) with the permissible strength limit of (compressive strength ≥ 23 Mpa). The maximum porosity percent is in the case of (15%) addition being (2.915%) and the minimum porosity percent is in the case of (5%) addition (1.457%).

7. References

- [1] Callister, W. D. Jr., Rethwisch, D. G. (2008) "Fundamentals of materials science and engineering", 3rd edition, Asia, John Wiley & sons.
- [2] S.A. Al-Sanea. "Thermal performance of building roof elements. Building and Environment". Vol.37, 2002, 665–675.
- [3] Hernandez-Olivares, F., M.R. Bollati, M. del Rio, M., B. Parga-Landa, "Development of cork–gypsum composites for building applications". Construction and Building Materials, Vol.13, 1999, 179–186.
- [4] M. Mohsen, B. A. Akash, Some prospects of energy saving in Jordan, Energy conservation and Management, Vol.42, 2001, 1307-1315
- [5] B.A. Jubran, S.M. Habali, M.A.S. Hamdan, Adnan I.O. Zeid, "Some mechanical and thermal properties of clay bricks for Jordan valley region Materials and Structure", Vol.21, September 1988, No.125, 364-369
- [6] S. Jaber, M. Hamdan, "The Thermal and economical analysis of renewable energy buildings", Towards low energy house in Jordan, Proceeding of GCREEDER conference, Amman – Jordan, 2009
- [7] Al-Otoom, A. Al-Khlaifa and A. Shawaqfeh, "Crystallization Technology for Reducing Water Permeability into Concrete", Industrial & Engineering Chemistry Research Vol.46, 2007, 5463-5467
- [8] F.P. Incropera, D.P. Dewitt, L. Bergman and A.S. Lavine, "Fundamentals of Heat and Mass Transfer", Six edition, John Wiley & Sons, 2007, USA (Ch. 1 & 3),
- [9] J.A. Wordingham, P. Reboul, "Dictionary of Plastics, third edition". Newnes Middlesex, England. 1968.
- [10] F.W. Billmeyer "Textbook of Polymer Science", Second edition. John Wiley, New York. 1984.
- [11] Thermal insulation - Determination of steady-state thermal resistance and related properties - Heat flow meter apparatus International Standard Organization; ISO 8301:1991, 2006.

The Temperature Effect on Sensitivity of Direct Detection Optical Receiver Incorporating FET- Amplifier

Abdulgaffar S. M.

Elect.and electronic Eng. Dept.
College of Engineering
Thi-Qar University

RafidM.Hannun

Elect.and electronic Eng. Dept.
College of Engineering
Thi-Qar University
eng_rafid005@yahoo.com

Muhannad Sahib Ali

Mech. Eng. Dept.
College of Engineering
Thi-Qar University

Abstract

It is known that temperature rise boosts the generations of electron-holes pairs in semiconductors and increases their conductivity that obtained to increase noise. High Electron Mobility Transistors (HEMTs) gives many advantages like low noise and high associated gain at microwave frequencies. Different shapes and places in containers are done to analyze the temperature effect on chips with other thermal and aerodynamic parameters.

In this paper, the performance of integrated optical receiver consisting of PIN (Positive Intrinsic Negative)-photodiode and HEMT-based transimpedance type amplifier is analyzed upon the effect of temperature variation. Variation of temperature occurs when change device space in one block covers. The simulation results show that the sensitivity (P_{sen}) of an optical receiver is minimal in space when temperature effect is low if it is based on well-designed HEMT.

المستخلص

تؤدي ارتفاع درجات الحرارة في أشباه الموصلات إلى توليد أزواج إلكترون-فجوة التي تؤدي إلى زيادة الموصلية والتي تزيد من الضجيج. لذا تعطي الترانزسترات ذات حركة الإلكترونات العالية عدة ميزات كإنخفاض الضجيج والربح المصاحب العالي في ترددات الموجات الدقيقة المايكروية. تم اختيار مواقع وأشكال مختلفة للحيز الذي يحتوي هذه الدقائق الإلكترونية لتحليل تأثير درجة الحرارة عليها ودراسة بعض الخصائص الحرارية والايرو ديناميكية لها.

تم في هذا البحث تحليل أداء المستلم البصري المتكامل المتكون من دايمود ضوئي نوع PIN ومضخم من نوع الممانعة الانتقالية المعتمدة على HEMT. تم هذا التحليل بالاعتماد على تأثير تغير درجة الحرارة. إن تغير درجة الحرارة يحدث عند تغيير شكل وفضاء الحيز الذي يحتوي هذه الأجهزة. نتائج المحاكاة بينت أن الحساسية للمستلم البصري تكون الأقل في الفضاء الذي يكون فيه تغير درجة الحرارة قليل عندما يكون تصميم HEMT جيد.

1. Introduction

The continuing minimization of electronic devices has significantly contributed to rapid developments in electronic technology. Miniaturization is, however, characterized by high heat dissipation per unit area of electronic components. Therefore, an effective cooling strategy is required to avoid premature failure and to ensure enhanced reliability and life expectancy of electronic components. Despite various cooling techniques and recent developments in the electronic industry, air cooling is still considered to be not only a cheap and readily available option but also a very effective technique.

The optoelectronic device that recovers the transmitted electrical signal from the incident light wave signal is optical receiver. It is formed from a photo detector (photodiode), connected to a FET-based amplifier. It is represented by PIN photodiode. Theoretical sensitivities for both PIN/FET direct-detection receivers are shown in Figure(1)[1, 2].

HEMTs based on AlGaAs/InGaAs structure given many advantages due to their low noise [3], and high associated gain at microwave frequencies [1]. Therefore, they are well suited to the preamplifier requirements of broadband light wave receivers.

It is expected that the monolithic integration of optical and electronic components on the same chip will alternatively lead to ultra-high speed, high sensitivity, reliability, and low cost [4,5]. Most of wide band optical receivers have been fabricated by integrating a PIN photodiode for light detection [3], and a transimpedance amplifier for electronic signal amplification and impedance matching [6].

In this paper the performance(sensitivity) is analyzed for a monolithically integration optical receiver consisting of a PIN photodiode and an FET-based transimpedance type preamplifier through variation of temperature to determine the optimum space with minimum effect of temperature.

The resulting boundary layer equations for a two-dimensional vertical flow, with variable fluid (air) properties except density, for which the Boussinesq approximations are used, are then written as [7, 8]:

$$\frac{\partial u}{\partial x} + \frac{\partial v}{\partial y} = 0 \quad (1)$$

$$u \frac{\partial u}{\partial x} + v \frac{\partial v}{\partial y} = g\beta(T - T_{\infty}) + \frac{1}{\rho} \frac{\partial}{\partial y} \left(\mu \frac{\partial u}{\partial y} \right) \quad (2)$$

$$\rho c_p \left[\frac{\partial u}{\partial x} + \frac{\partial v}{\partial y} \right] = \frac{\partial}{\partial y} \left(k \frac{\partial T}{\partial y} \right) + q''' + \beta T u \frac{\partial P_a}{\partial x} \mu \left(\frac{\partial u}{\partial y} \right)^2 \quad (3)$$

where the last two terms in the energy equation are the dominant terms from pressurework and viscous dissipation effects. Here u and v are the velocity components in the x and y directions, respectively. Although these equations are written for a vertical, two-dimensional flow, similar approximations can be employed for many other flow circumstances, such as axisymmetric flow over a vertical cylinder and the wake above a concentrated heat source.

2. Receiver

2.1 Description

In this paper, the optical receiver is considered to consist of an InGaAs PIN photodiode integrated with a single gain stage trans impedance amplifier as shown in Fig (1). The design of preamplifier provides (i) a wide bandwidth; and (ii) high dynamic range, which is defined as the range of input power levels over which the bit error rate is acceptable [9]. All of the loads in the circuit are active to allow for integration with the other HEMTs and to reduce device area and overall power dissipation of the circuit. A feedback convention resistor is replaced by a transistor (Q_3) with an equivalent output resistance R_F . The FET feedback can be used to reduce parasitic shunt capacitance, thereby resulting in a wide bandwidth operation.

2.2 Receiver noise sources

The receiver current noise consists of thermal noise in the feedback resistor, FET channel noise, low frequency (LF) noise and shot noise due to the leakage in the FET gate and the detector. Contributions noise in an optical receiver are determined by [5, 9]:

$$\sigma_{sh} = \sqrt{2q(I_{Dark} + I_{leak})I_2 B} \quad (4)$$

$$\sigma_{ch} = 4\pi C_T B \sqrt{\frac{kT\Gamma I_3 B}{g_m}} \quad (5)$$

$$\sigma_{LF} = 4\pi C_T B \sqrt{\frac{2kT\Gamma f_c I_f}{g_m}} \quad (6)$$

$$\sigma_{th} = 2 \sqrt{\frac{kT I_2 B}{R_F}} \quad (7)$$

Here, σ_{sh} , σ_{ch} , σ_{LF} , and σ_{th} are the shot noise, channel noise, LF noise, and thermal noise respectively, g_m is the extrinsic transconductance, T is the temperature, k is the Boltzmann constant, B is the data bit-rate, I_{Dark} is the PIN dark current, q is the electronic charge, I_{leak} is the gate leakage current, Γ is the HEMT noise figure (≈ 1.6 [5]), f_c is the LF corner frequency, and C_T is the total front-end capacitance. C_T is determined by:

$$C_T = C_{st} + C_{PD} + C_{GS} \quad (8)$$

where, C_{st} is the input stray capacitance, C_{PD} is the PIN diode capacitance, and C_{GS} is the HEMT gate-source capacitance. I_f , I_2 , and I_3 are effective receiver bandwidth integrals which depend on the transfer function of the circuit and the input and output waveforms. A NRZ data format is assumed, and a raised cosine output pulse response of the receiver for a rectangular pulse shape.

2.3 Receiver sensitivity

The sensitivity of receiver is given in terms of minimum, time-averaged incident optical power (P_{sen}), which can be detected for a given acceptable Bit Error Rate (BER). Assuming Gaussian noise statistics, the sensitivity is determined by [9]:

$$P_{sen} = \left(\frac{Qhf}{\eta q} \right) \sigma_T \quad (9)$$

where, η is the overall efficiency in converting the incident optical power into a signal current, h is Planck constant, f is the frequency of the incident light, $Q=6$ for $BER=10^{-9}$, and σ_T is the total noise standard deviation which is defined as:

$$\sigma_T = \sqrt{\sigma_{sh}^2 + \sigma_{ch}^2 + \sigma_{LF}^2 + \sigma_{th}^2} \quad (10)$$

Sensitivity of Receiver may be improved by decreasing the impedance at the interface. The low impedance at the PD-amplifier interface is highly non-optimal from a noise point of view, which, together with the intrinsic noise figure of the amplifier, limits receiver sensitivity.

It may be expected that the integration of monolithic transimpedance receiver is one of the facial ways to realize high sensitivity OptoElectronic Integrated Circuits (OEICs) [10].

3. Transimpedance amplifier

The PIN/transimpedance amplifier equivalent circuit is shown in Figure 2, where C_F is the stray capacitance of the feedback resistor R_F , R_{in} is the input resistance of the amplifier, A is the amplifier voltage gain, and I_{ph} is the PIN diode photocurrent.

The receiver response is represented by the transimpedance Z_T , which is the ratio of the output voltage to the input photocurrent. The frequency dependence of Z_T is calculated by [11]:

$$Z_T(f) = \frac{-AR_{in}R_F/[R_F + (I+A)R_{in}]}{1 + j \frac{2\pi f R_{in}R_F}{R_F + (I+A)R_{in}} [C_T + (I+A)C_F]} \quad (11)$$

Let Z_{T0} be the DC transimpedance, and f_{3dB} is the cutoff frequency (-3dB point), then:

$$Z_{T0} = \frac{-AR_{in}R_F}{R_F + (I+A)R_{in}} \quad (12)$$

and

$$f_{3dB} = \frac{I}{2\pi \left[\frac{R_{in}R_F}{R_F + (I+A)R_{in}} [C_T + (I+A)C_F] \right]} \quad (13)$$

Eqn. 13 is useful in determining the bandwidth of the system.

The bandwidth of the preamplifier should be at least equal to the effective noise bandwidth of the receiver (I_2B). To accomplish this, R_F must be adjusted such that f_{3dB} is equal to the effective bandwidth. Let $A \gg 1$ and $AR_{in} \gg R_F$, Eqn. 13 becomes:

$$f_{3dB} = [2\pi R_F (C_F + C_T/A)]^{-1} \quad (14)$$

then

$$R_F = [2\pi I_2 B (C_F + C_T/A)]^{-1} \quad (15)$$

Figures (3, 4) display the variation of thermal and shot of receivers noise sources as a function of bite rate, they give much prediction of receiver behavior.

Figure(6) displays the variation of sensitivity as function of bite rate.

Figures (7, 8, 9, 10) and (11, 12, 13, 14) display the variation of different receivers noise sources as a function of T. Otherwise, the parameter values used in the simulation are listed in Table(1). It is clear that the thermal and shot noises increase in the absence of temperature. At B=10 Gbit/s, the thermal noise rise is more important than that of the shot noise. The channel and LF noise behave in asame manner. However, at the same bit-rate, the channel noise and LF noise increase by factors of 1.4 and 2.08, respectively. The total noise current decreases to 0.107 of its value at 10 Gbit/s bit-rate. In Figure(6),the total noise is plotted as a function of bit-rate.

In Figure (5) R_F that satisfies the condition of negligible intersympole interference is plotted as a function of the bit-rate. Note that $R_F \approx 600 \Omega$ is required for B=10 Gbit/s. The dependence of receiver sensitivity on bit-rate is depicted in Figure(7). Note that P_{sen} (in dBs) decreases linearly with the temperature.

4. Theoretical analysis of aerodynamic and thermal parameters[13]

The heat sources simulate the components of electrical devices generating a natural convection flow in the enclosure. In addition, an externally sourced uniform air stream with a specific temperature enters the enclosure from a section located at the bottom of the enclosure (entry section) and exhausts from the upper rear section (exist section). This airflow generates a forced convection flow in the enclosure.

The equations (1, 2, 3) can be solved for domain which use air as fluid with natural convection at using the enclosure without velocity input or output and using mixed convection with using velocity input at bottom of enclosure to exit from outlet at the upper

vent. Energy equation demonstrated by equation (3) can be derived to get Prantle number of 0.7 for this type of flow. This analysis applied by the following boundary conditions:

$$u=v=0, \frac{\partial T}{\partial n}=0 \quad \text{at all the walls} \quad (16)$$

$$u=u_{in}, v=0, T=T_{atm} \quad \text{at } x=0 \text{ and } 0 \leq y \leq 5\text{cm} \quad (17)$$

$$u=u_{out}, v=0 \quad \text{at } x=x_{max} \text{ and } 25\text{cm} \leq y \leq y_{max} \quad (18)$$

$$x=x_{chip}, y=y_{chip}, q'''=\text{constant} \quad (19)$$

at this paper $x_{max}=60\text{cm}$ and $y_{max}=30\text{cm}$

5. Numerical analysis

To solve the equations of continuity, momentum and energy for temperature distribution domain start by the following steps:

- 1- By using GAMBIT code [12], the systems are drawn to be more than 18000 nodes depending the number of electronic devices for two dimensional space.
- 2- FLUENT 6.3 code[12] used to solve the case study by using finite volume method (one of computational fluid dynamics techniques) [8].

Steady, viscous, laminar and compressible air flow is used. The density calculated as Boussinesquequation [7]. The operating pressure is 101325 Pascal at reference location of $x=0$, $y=0$ (left bottom corner of system). The operating temperature is 300K. The heat flux rate is 10W/m^2 for any electronic device.

SIMPLE method used to solve pressure-velocity coupling with standard discretization of pressure, first order upwind discretization of momentum equation and energy equation [14].

The convergence of equations is 1×10^{-3} for continuity and velocity equations. It is 1×10^{-6} for energy.

6. Results and discussion

6-1 Sensitivity

To calculate the performance of the optical receiver, a HEMT with parameter values given in Table 1 are assumed. Other parameters used in this analysis are listed in Table 2. The HEMT performance such as g_m , C_{GS} , and C_{GD} are determined from expressions derived in Eq.(9). The HEMT capacitance and trans conductance are functions of structure parameters of the device. Therefore, it is expected that the sensitivity of HEMT-based receivers vary with transistor structure parameters.

However, the simulation results reveal that this fact loses its importance when

C_{GS} is kept much lower than $(C_{PD}+C_{st})$; or

The total front-end capacitance to trans conductance ratio (C_T/g_m) is small. In other words, the operation speed of the HEMT is much greater than the bit-rate.

Using the parameters listed in Tables (1) and(2), the PIN/HEMT optical receiver sensitivity is display in Tables(3) and(4) as a function of temperature and plotted in Figure(8) and Figure(13) as a function of T for different block form (the lower temperature induced at the design of one chip only or for three chips as shown in figure 21 to be 300.5 K). The results in this figures indicate clearly that the receiver sensitivity is less affected by the variation of T when T is small and this effect is more pronounced optimum space of receiver. For the receiver under consideration,. The simulation results indicate that P_{sen} is almost independent of the variation of T parameters. In fact, P_{sen} is minimum where T is minimum and because that the optimum space for the first block is (1) and for the second block is (2).

Figures (8, 13) present directly depend the sensitivity and temperature, also the Figures (9-12), (14- 17) offer directly dependence of the noise source with different temperature in each block.

6-2 Thermal Parameters

Eight cases of enclosure of chip design are studied at this paper. These cases are done by changing the site of chip for a typical design as shown in Figures (19, 20) and (23); case A is general for three chips, but in B the upper right chip. The lower right chip in C and the upper left chip in D. The lower mid chip is for shape (E) and the upper mid chip for F. There are two cases for half circle shape; the first is at the lower and the other isat upper. The

temperature for the first five square cases are indicated in Table (3) and for half circle in Table (4).

Figure (19) shows the velocity vectors and contours for different shapes of instrument container. For squared figure, in slide shape A it is observed that high velocity values happen at the exit (0.25 m/s) because of decreasing the density of air as a result to increasing the temperature due to the electrical and electronic devices. There is a circulation zone at the container centre. The circulation zone lies at the circumferential wall with large circle at B since one source of heat found here with low effect. Accelerated velocity at C (0.38m/s) is as a result to seven sources of heat which create strong free convection. This velocity magnitude is forced at slide contour D for low effect of obstacle to hot air passes from input vent (at low part) to output vent (at the high part). The same effect for E, but for F high velocity magnitudes takes place in comparison with all shapes to above cause. For half circle container shape, low velocity range at shape G but at H is the higher. These values are the middle values among all figures.

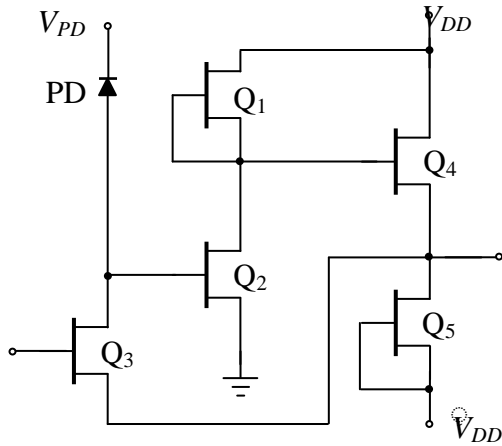
Figure (18) shows good prediction to velocity magnitude. The lower average value is near the outlet vent of system (0.52m of the horizontal dimension 0.6m) because of circulation and vortex due to the electronic devices places. But the higher is at the inlet vent. As a result to different values of velocity mentioned above and due to heat added to system because of the electronic devices, high temperature values accumulated at low velocity values. The temperature is considered as sensible heat values.

Figure (20) presented the temperature contour of domain. The range is between 300.5K to 307K for squared shape but it is between 301K to 304K for half circle shape. These differences as a result to heat added inside the system, heat rejected from the system due to free convection and the air velocity obstacle through the domain. The difference is very small as mentioned in figure. Higher temperature (307K) is at shape C and E but the lower (304K) is at shape G.

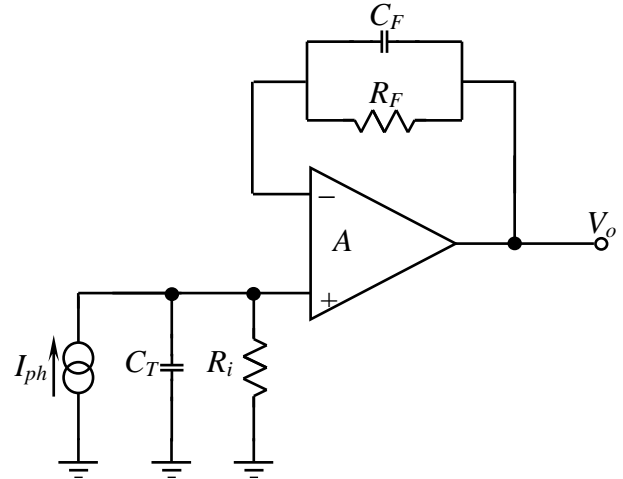
Figure (21) presented the temperature average values with horizontal axis at one domain. The highest values demonstrated here for the electronic devices places which continuously lost heat to device interior.

The pressure values in the system demonstrated by Figure (23) that give low values converged to atmospheric pressure because it is near the ground level and low temperature gradients throughout the different shapes. So, it is observed naturally low pressure values at the upper part and the higher at the low part for all shapes domain.

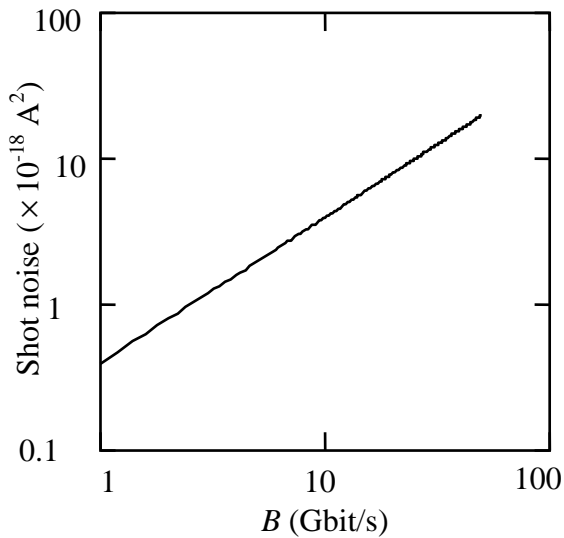
Figure (22) shows that the higher pressure value at the bottom. The average lower value is at two-third height of system.



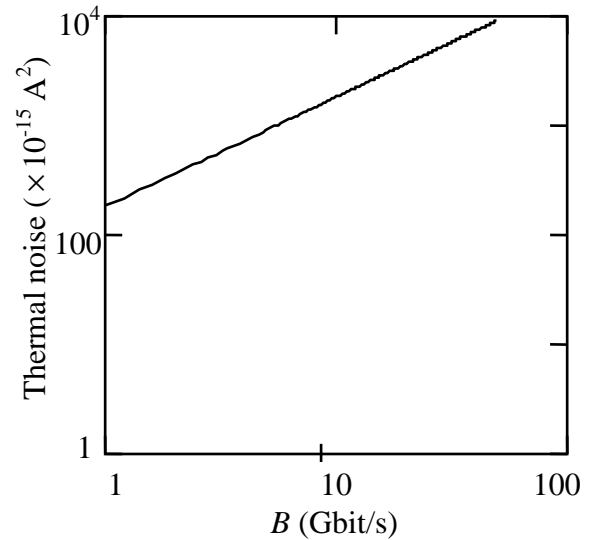
Figure(1). Circuit diagram of a transimpedance optoelectronic integrated circuit (OEIC) optical receiver.



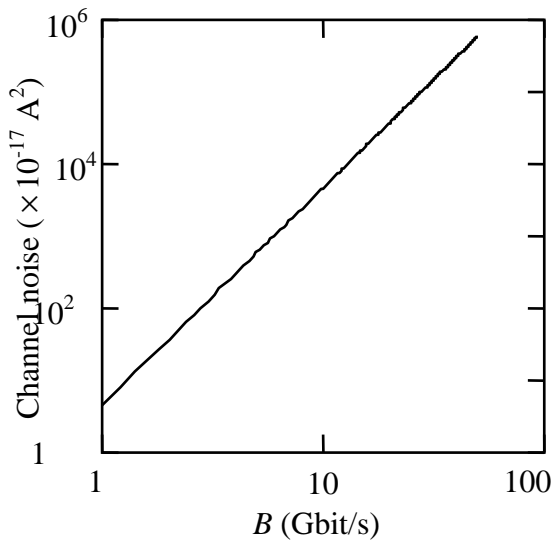
Figure(2). Equivalent circuit of the Amplifier of Figure(1).



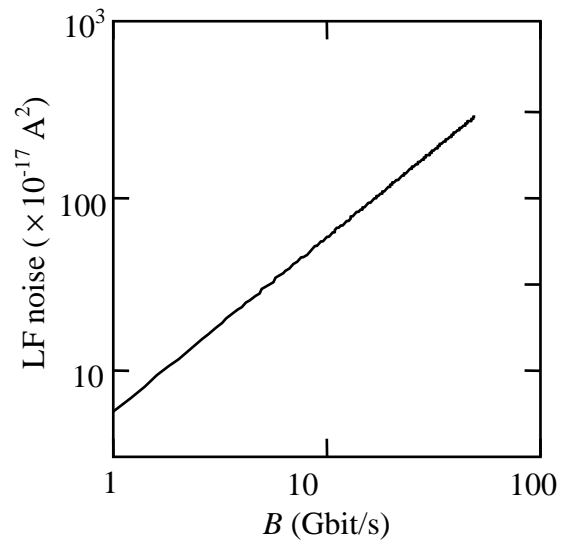
Figure(3). Variation of Shot noise as a function of B for BER of 10^{-9} .



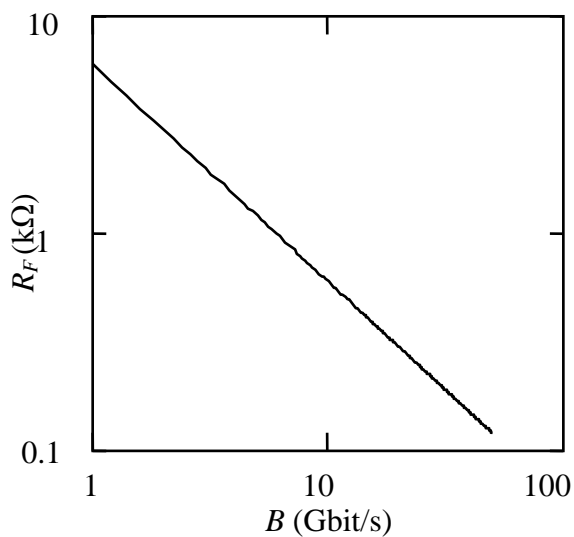
Figure(4). Variation of thermal noise as a function of B for BER of 10^{-9} .



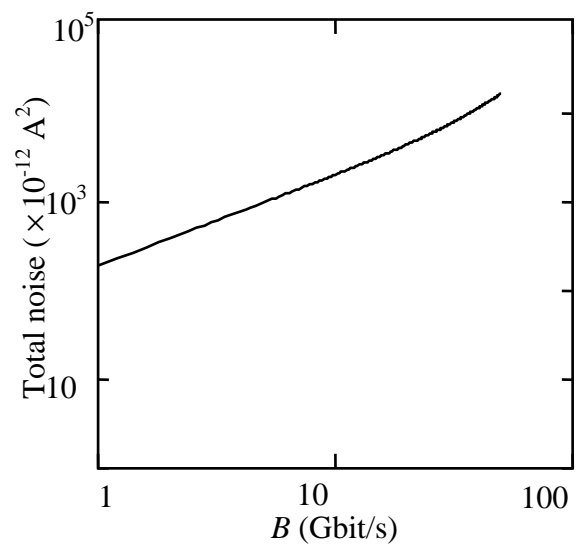
Figure(3d). Variation of Channel noise as a function of B for BER of 10^{-9} .



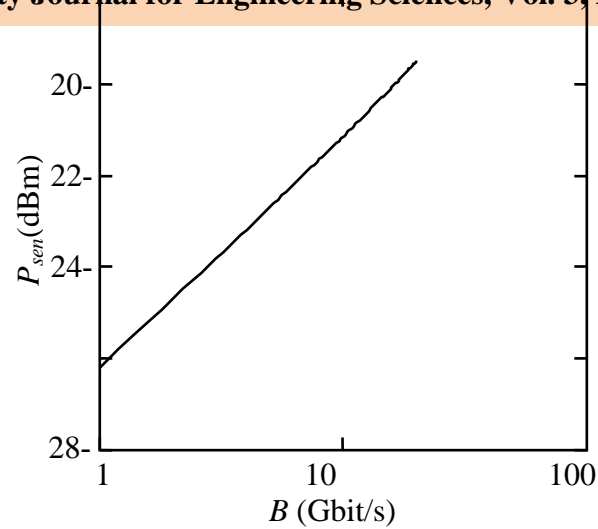
Figure(3c). Variation of LF noise as a function of B for BER of 10^{-9} .



Figure(5). Feedback resistance satisfying the condition of negligible ISI noise as a function of the bit rate.



Figure(6). Total noise as a function of bit-rate for BER of 10^{-9} .



Figure(7). Receiver sensitivity as a function of data bit-rate.

Table (1). Receiver parameters values used in the simulation.

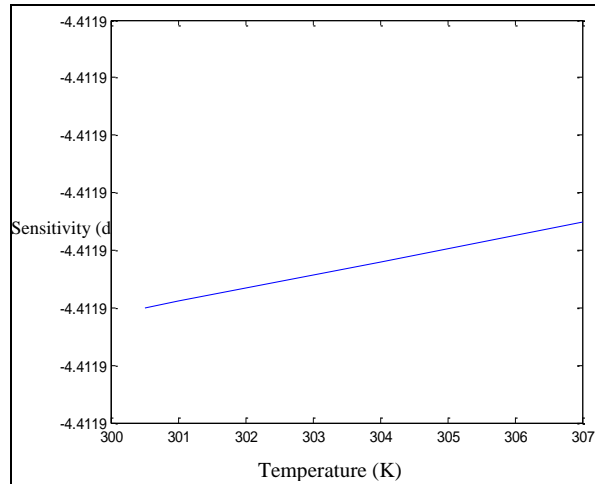
Parameter	Value	Unit
Q	6	-
I_2	0.55	-
I_3	0.085	-
I_f	0.12	-
I_{dark}	2	nA
J_{leak}	10	mA/cm^2
f_c	25	MHz
λ	1.55	μm
Γ	1.6	-
η	0.85	-
C_{PD}	125	fF
C_{st}	125	fF
B	10	Gbit/s

Table (2). FET parameters used in the simulation.

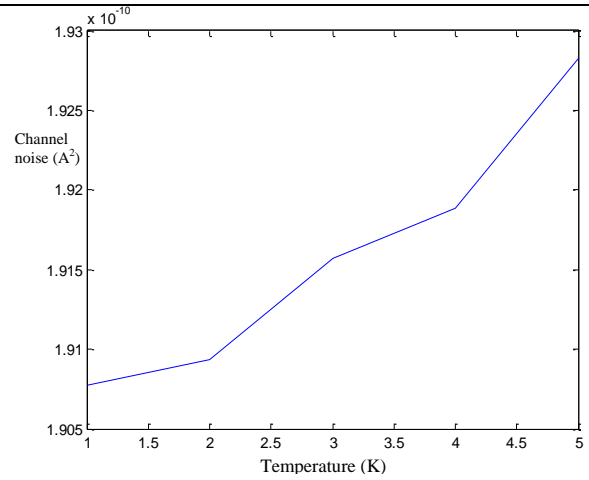
Parameter	Value	Unit
L_g	50	nm
W	50	μm
d_i	20	\AA
d_d	80	\AA
μ	12800	cm^2/Vs
v_{sat}	280×10^7	Cm/s
ϵ_r	12.1	–
N_d	6×10^{18}	cm^{-3}
V_{off}	-0.017	V
R_s	1.0	Ω
R_d	1.0	Ω

Table (3).Sensitivity(dB) as a function of temperature(K).

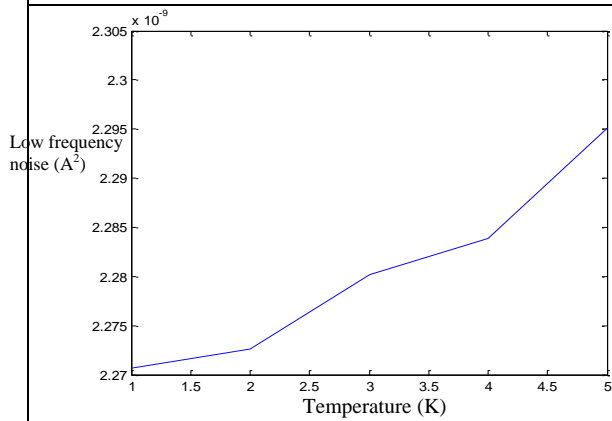
T(k)	$P_{sen}(\text{db})$
300.5	-4.41190884739970
301	-4.41190884737677
303	-4.41190884728509
304	-4.41190884723925
307	-4.41190884710172



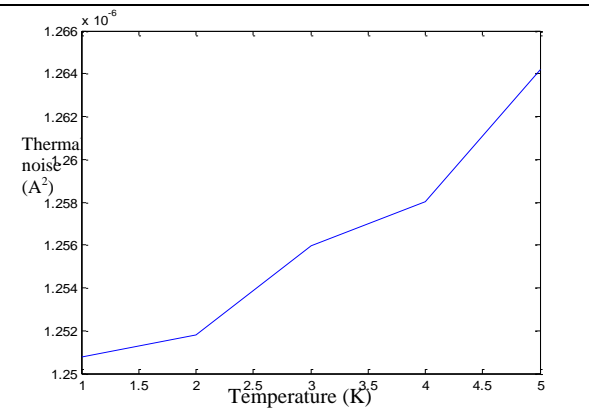
Figure(8). Sensitivity(dB) as a function of temperature(K).



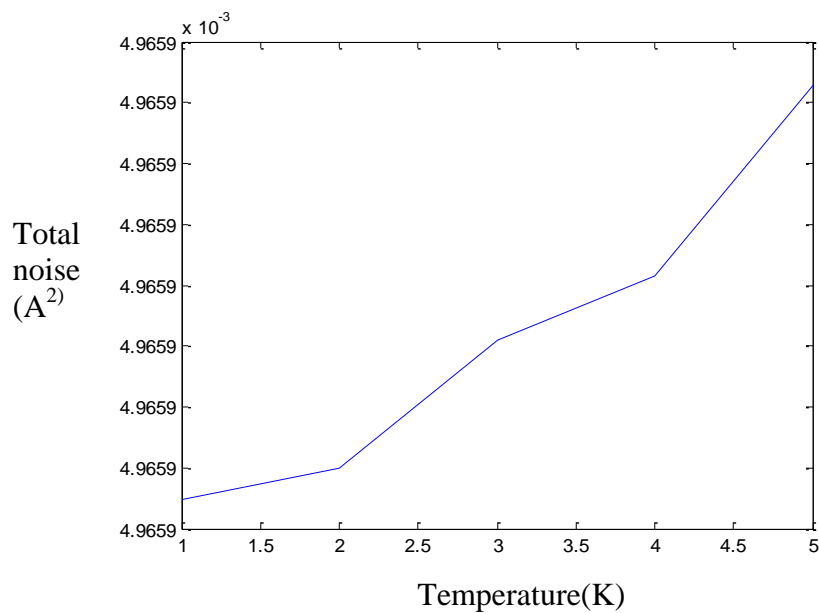
Figure(9).Low frequency noise(A^2) with respect to temperature (K).



Figure(10). Channel noise(A^2) as a function of temperature(K).



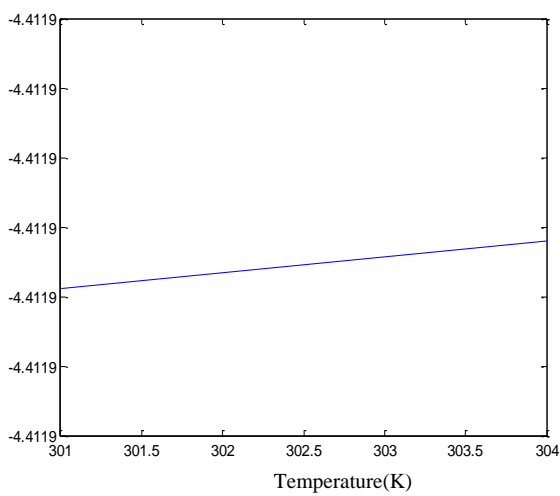
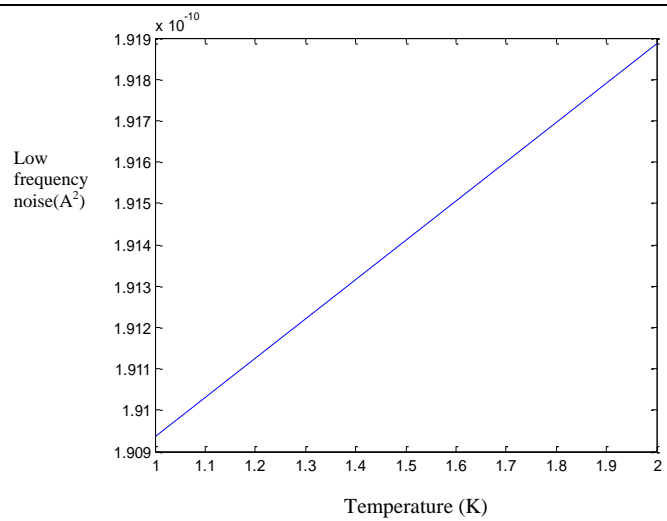
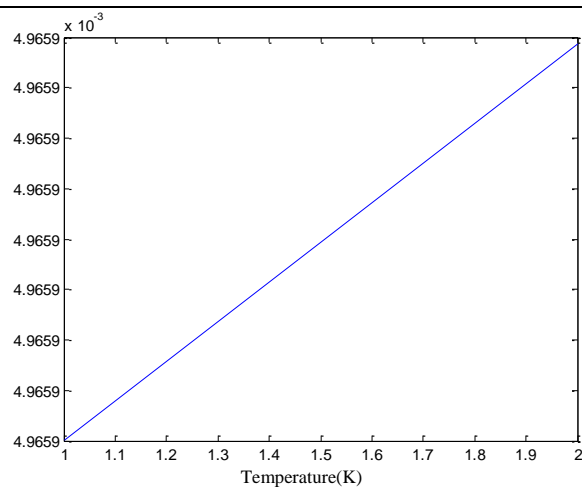
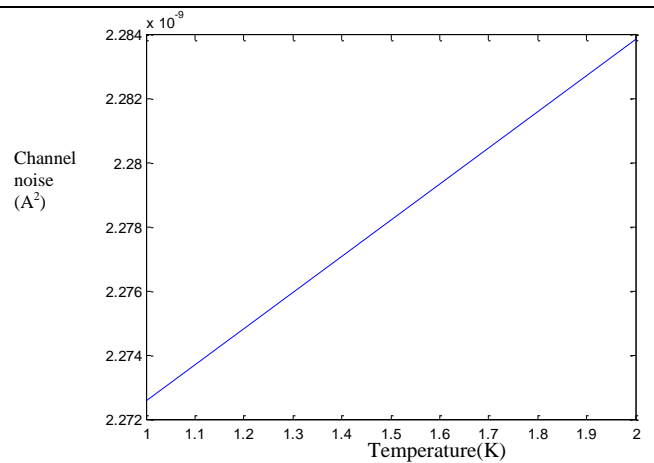
Figure(11).Thermal noise(A^2) with respect to temperature(K).



Figure(12). Total noise(A^2) as a function of temperature(K) .

Table(4).Sensitivity(dB) as a function of temperature(K).

T(K)	$P_{sen}(db)$
301	-4.411908847376774
304	-4.411908847239248

**Figure(13). Sensitivity(dB) as a function of temperature(K).****Figure(14).Law frequency noise(A²) with respect to temperature(K).****Figure(15). Total noise(A²) as a function of temperature(K).****Figure(16). Channel noise(A²) with respect to temperature(K).**

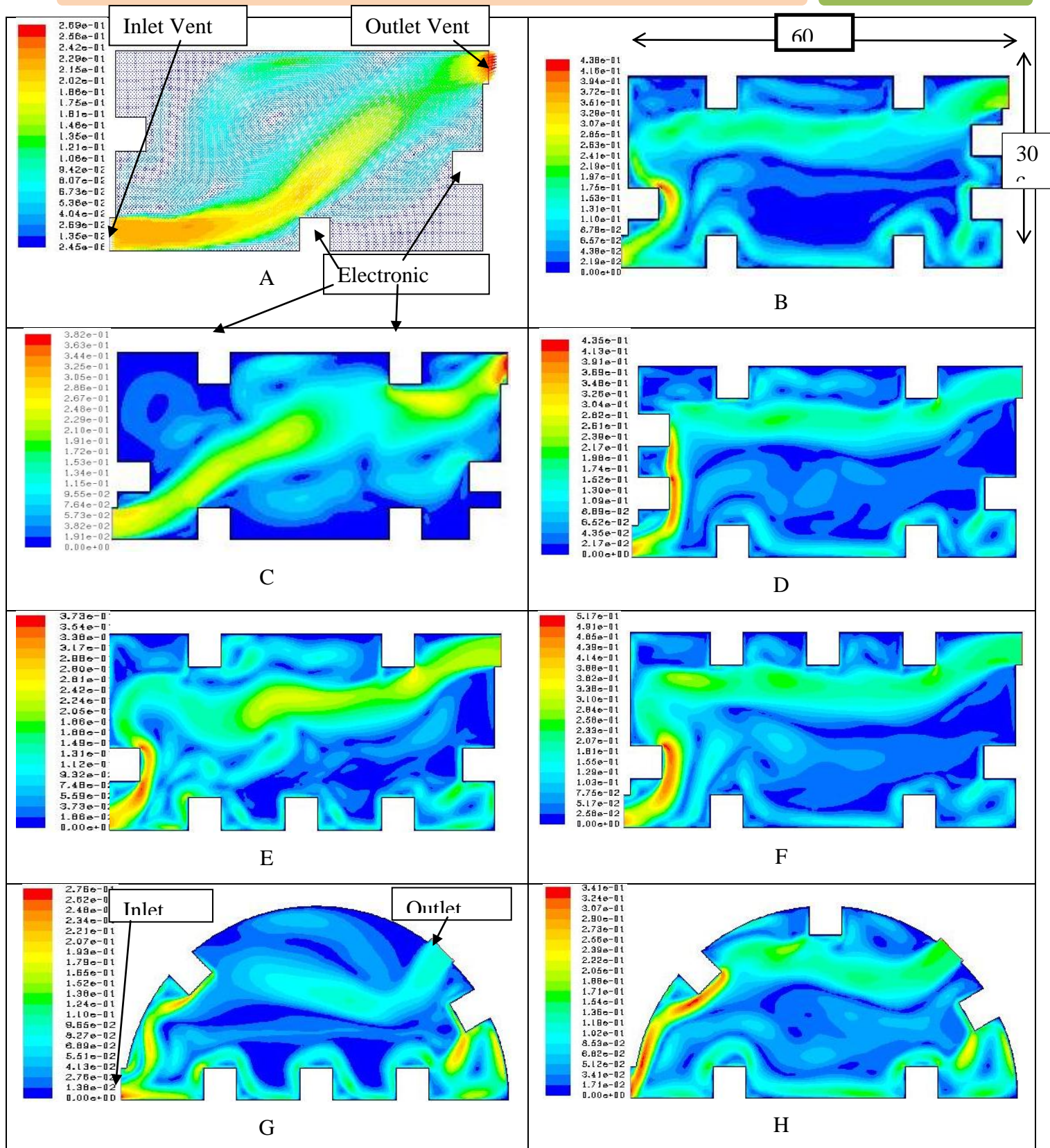


Figure (19). Velocity vectors and contours .

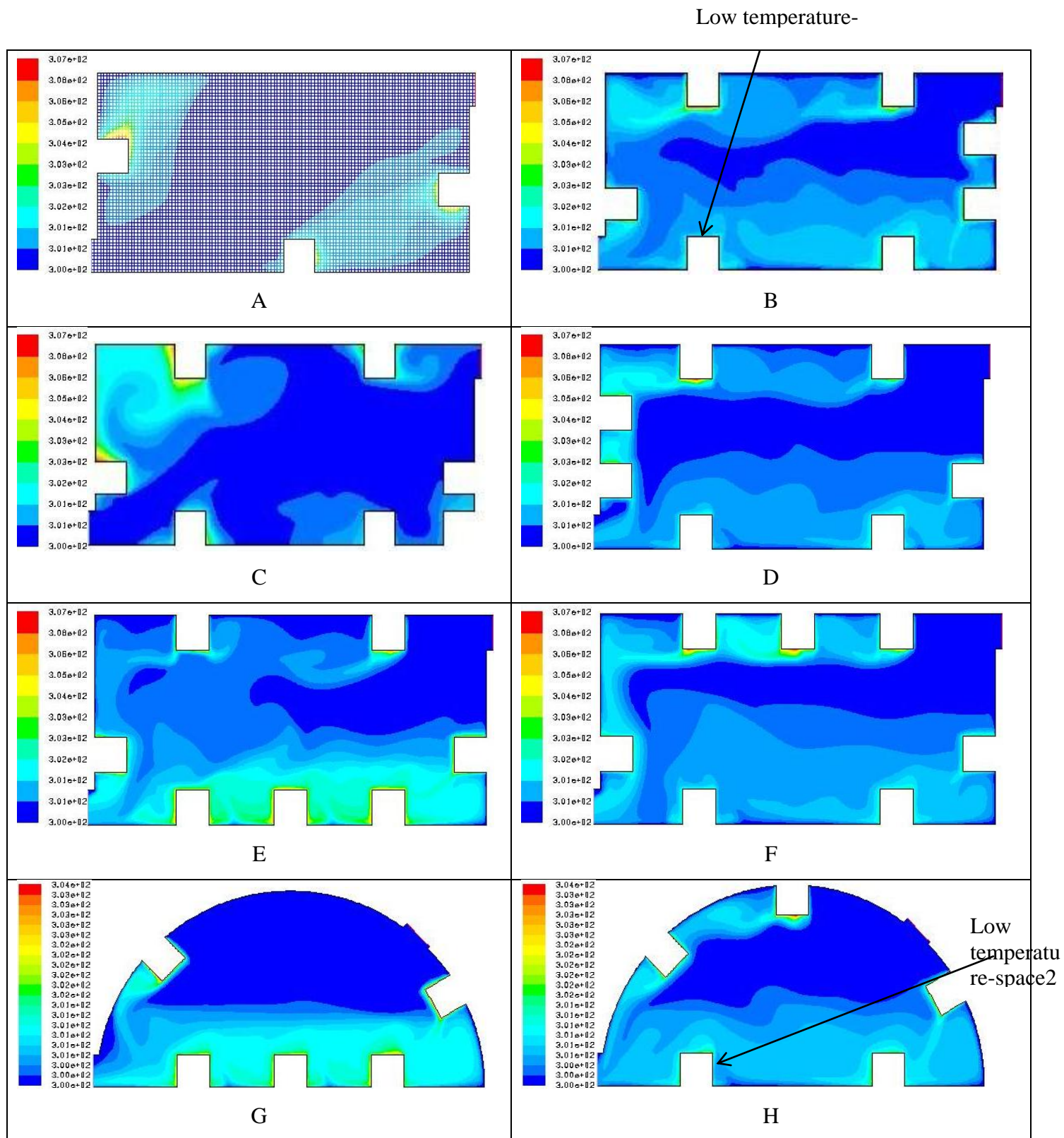


Figure (20). Contours of temperature gradient.

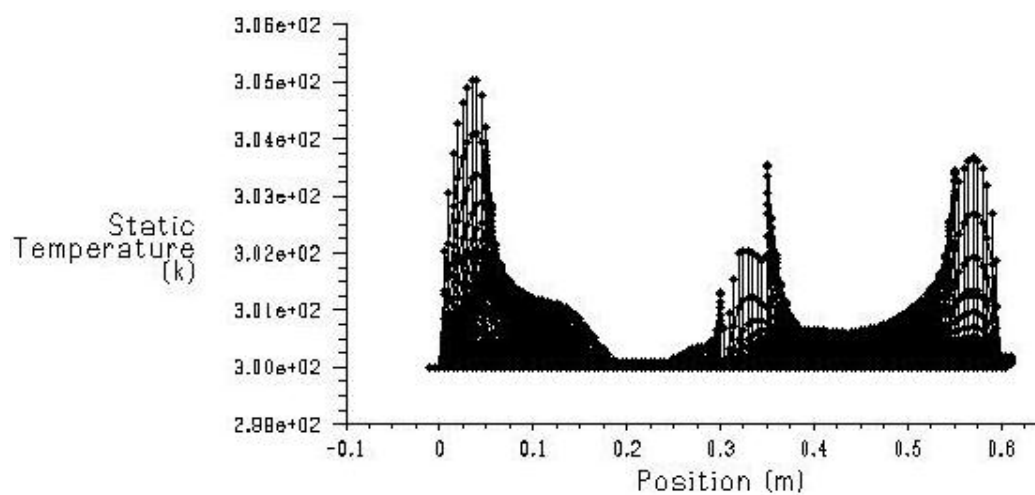


Figure (21). Static temperature with horizontal axis of domain.

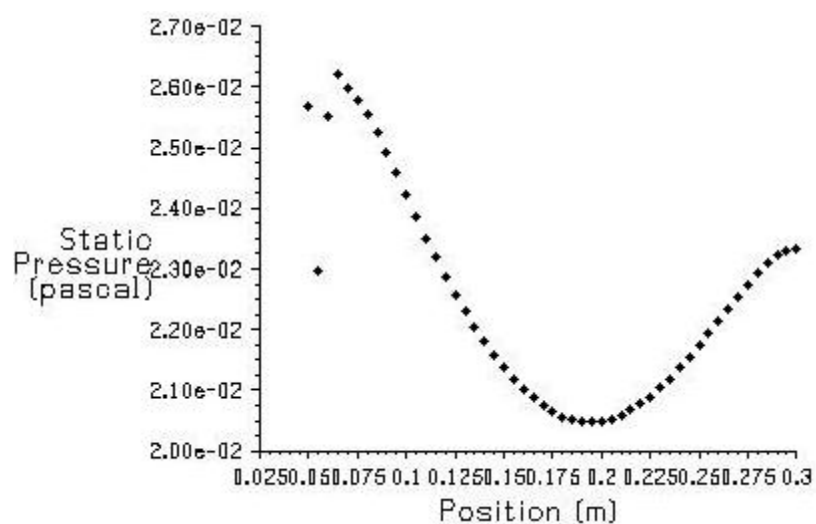


Figure (22). Static pressure curve with position at vertical axis.

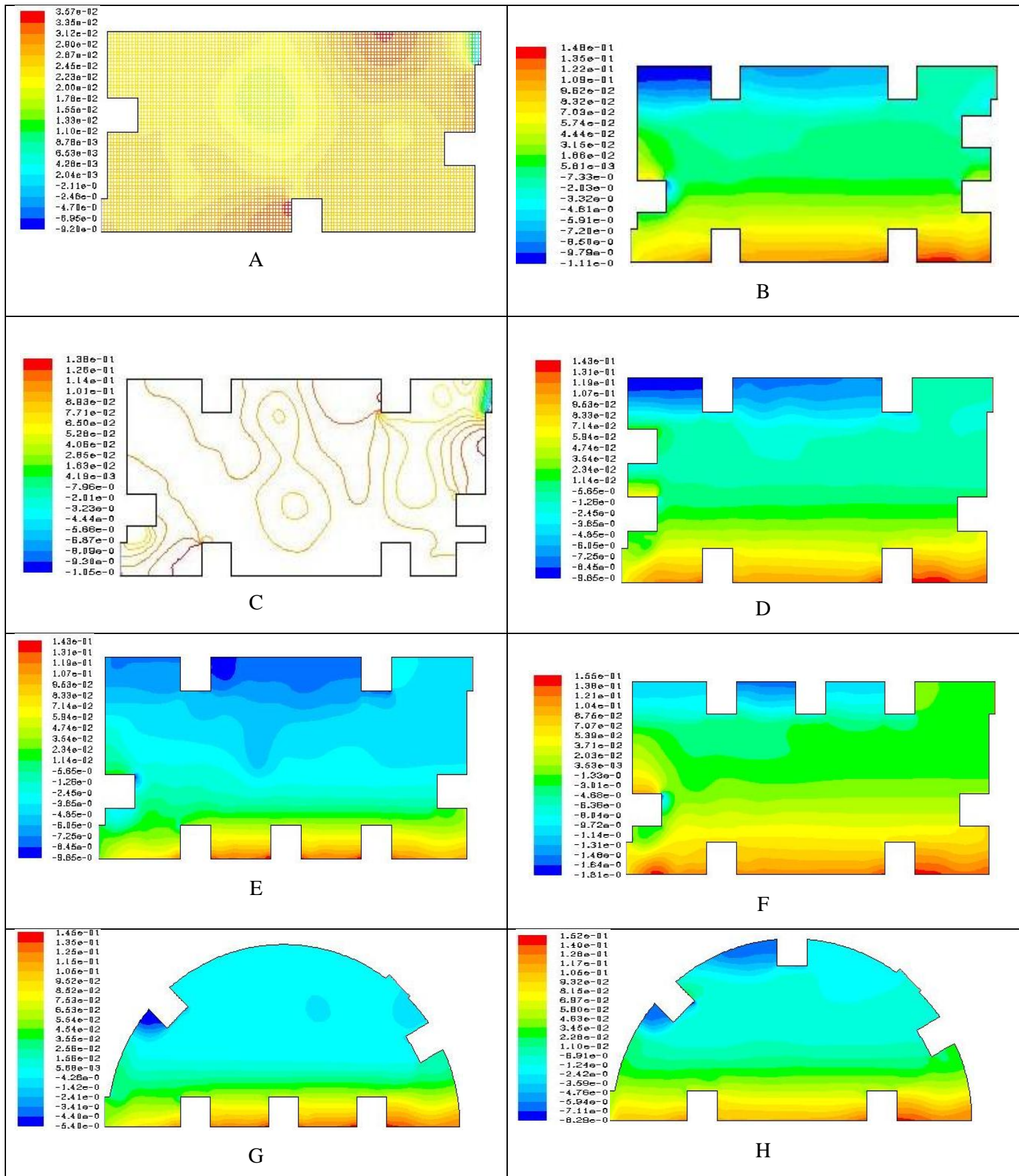


Figure (23) Static pressure contour.

7. Conclusion

The temperature performance of optical receiver consisting of PIN-photodiode and FET-based transimpedance type amplifier is by investigating the effect of various device parameters on receiver performance. The simulation results show that the sensitivity (P_{sen}) of an optical receiver is approximately independent of temperature, of one block, however, as shown in Fig.20, the optimum space for the first block is in space (1), while in the second block the optimum space is (2).

The velocity of air inside the container plays an important role in changing the temperature of chips. So, the chip position has importance in evaluation of heat supply or transferred from one space to another.

The heat generation as a result of electrical power in electronic devices field must be studied to fasten them in proper situation inside the selected block.

8. References

- [1] C. H. Chen and M. J. Deen, "Channel noise modeling of deep submicron MOSFETs," IEEE Trans. Electron Devices, vol. 49, pp. 1484–1487, Aug. 2002.
- [2] H. Shin, J. Jeon and S. Kim, "Analytical Thermal Noise Model of Deep Submicron MOSFETs," Journal of Semiconductors Technology and Science, vol. 6, No. 3, September, 2006.
- [3] B. Claflin, E. R. Heller, and B. Wenningham, "Accurate Channel Temperature Measurement in GaN-based HEMT Devices and its Impact on Accelerated Lifetime Predictive Models," CS MANTECH Conference, May 18th-21st, 2009, Tampa, Florida, USA.
- [4] Claudiu Amza, Ovidiu-George PROFIRESCU, Ioan CIMPIAN, Marcel D. PROFIRESCU, "Monte Carlo Simulation of a HEMT Structures," Proceedings of The Romanian Academy of The Romanian Academy, Volume 9, Number 2, 2008.
- [5] Mustafa Erol, "Effect of Carrier Concentration Dependent Mobility on the Performance of High Electron Mobility Transistors," Turk J Phy, 25 (2001), 137 - 142.
- [6] Wen-Chau Liu, Wen-Lung Chan, Wen-Shiung Lour, Kuo-Hui Yu, Chin-Chuan Cheng, and Shiou-Yinh Cheng, "Temperature-dependence investigation of a high performance

- inverted data-doped V-shaped GaInP/In_xGa_{1-x}As/GaAs pseudomorphic high electron mobility transistor,” IEEE Trans. Electron Devices, vol. 38, no. 7, pp. 1290-1296, 2001.
- [7] Jaluria, Y., “Natural Convection Heat and Mass Transfer”, Pergamon Press, Oxford, 1980.
- [8] Versteeg H.K. and Malalasekera W., “An Introduction to Computational Fluid Dynamics, The Finite Volume Method”, Longman Group Ltd Copyright, England, 1995, (P.41).
- [9] D. C. W. Lo, and S. R. Forrest “Performance of In_{0.53}Ga_{0.47}As and InP junction field effect transistors for optoelectronic integrated circuits. II. Optical receiver Analysis,” Journal of Lightwave Technology, Vol. 7, No. 6, pp. 966-971, June 1989.
- [10] Alok Kushwaha, Manoj Kumar Pandey, Sujata Pandey, and A. K. Gupta, “Analysis of 1/f Noise in Fully Depleted n-channel Double Gate SOI MOSFET,” Journal of Semiconductor Technology and Science, Vol.5, No.3, September, 2005.
- [11] R. S. Fyath, and H. N. Wazeer "Performance Analysis of High Electron-Mobility Transistor for Optical Receiver," M. Sc. Thesis, University of Basrah, College of Engineering, Basrah, Iraq, 2002.
- [12] FLUENT 6.3.26, “User Guide and Manuals”, 2008.
- [13] Ismael M., “Numerical Simulations of Counter Flow Microchannel Heat Exchanger with Different Channels Geometry and Working Fluids”, Ph.D. Thesis, Basrah University, College of Engineering, (2009).
- [14] Gebhart, B., Jaluria, Y., Mahajan, R. L., and Sammakia, B., “Buoyancy Induced Flows and Transport”, Hemisphere Publishing, New York, 1988.

9. Nomenclature

Symbol Definition

x, y	Cartesian coordinates
x_{chip}	horizontal distance of chip
y_{chip}	vertical distance of chip
u, v	velocity component in x, y directions respectively
u_{in}	the velocity input to enclosure
u_{out}	the velocity output from the enclosure

g gravitational acceleration

β coefficient of thermal expansion $\beta = -\frac{1}{\rho} \left(\frac{\partial \rho}{\partial T} \right)$

μ Air viscosity

C_p specific heat at constant pressure

k conductivity

ρ density

\dot{q} heat generation rate

p pressure

T temperature

T_{atm} atmospheric temperature

t time

